

*Mineralogical and ion-exchange leaching  
study of a Rare Earth Element (REE)  
bearing ion-adsorption clay deposit*

by

Cody Owen Burcher-Jones

BRCCOD001



SUBMITTED TO THE UNIVERSITY OF CAPE TOWN

In fulfilment of the requirements for the degree

MASTER OF SCIENCE

in Chemical Engineering

Faculty of Engineering and the Built Environment

UNIVERSITY OF CAPE TOWN

Date of Submission: 19 February 2018

Supervisor: Professor Jochen Petersen

Co-supervisors: Ms Tokoloho Rampai, A. Professor Megan Becker, Professor Dee Bradshaw

The copyright of this thesis vests in the author. No quotation from it or information derived from it is to be published without full acknowledgement of the source. The thesis is to be used for private study or non-commercial research purposes only.

Published by the University of Cape Town (UCT) in terms of the non-exclusive license granted to UCT by the author.

## DECLARATION

I, Cody Owen Burcher-Jones, hereby declare that the work on which this dissertation/thesis is based is my original work (except where acknowledgements indicate otherwise) and that neither the whole work nor any part of it has been, is being, or is to be submitted for another degree at this or any other university.

I empower the university to reproduce for the purpose of research either the whole or any portion of the contents in any manner whatsoever.

Signature:

Signed by candidate

Date: 9 February 2018

## ACKNOWLEDGEMENTS

I would like to thank my supervisor, Professor Jochen Petersen, for the opportunity to work on this project and for guiding me along the way. I would also like to thank my co-supervisors Ms Tokoloho Rampai, A. Professor Megan Becker and Prof Dee Bradshaw for all their help and assistance through my degree. Thank you to Dr Michael Haschke of GUB Ingenieur AG for his collaboration as part of the German  $r^4$ -SEM<sup>2</sup> project and for supplying the samples. A special thank you to Dr Rahul Ram for his assistance throughout the project.

I would like to thank Kenneth Maseko and Monde Bekaphi for their assistance in the CMR lab and with the PSD data acquisition and to Ms Christel Tinguely and Dr Philip Janney from the Department of Geological Sciences (UCT) for their assistance in ICP-MS and XRF data acquisition and interpretation. A huge thank you to Maria Atanasova of the Council for Geoscience for her assistance in XRD data acquisition and interpretation. To Gaynor Yorath and Lorraine Nkemba, you were invaluable for your assistance in preparing the QEMSCAN blocks and QEMSCAN data acquisition and interpretation. This work is based on the research supported in part by the National Research Foundation of South Africa, grant number 86054.

I would like to thank Stephanie La Grange and Zulfa Le Riche for their assistance with Malvern PSD data acquisition and interpretation and thank Miranda Waldron and Dr Innocent Shuro for their assistance in SEM data acquisition and interpretation.

I wish to gratefully acknowledge Professor Dr. P.J. Kooyman for assistance in TEM data acquisition and interpretation. In addition, I wish to gratefully acknowledge the Centre for High Resolution Transmission Electron Microscopy, especially Dr. J.E. Olivier and Dr. J.H. O'Connell, at Nelson Mandela Metropolitan University in Port Elizabeth for their assistance and use of their facilities. This work is based on the research supported in part by the National Research Foundation of South Africa, grant number 94878.

I would like to thank my parents, Terence and Fiona Burcher-Jones, for all their love and support. I would like to thank all the input and assistance from friends and colleges from Minerals to Metals, Centre for Minerals research, Hydrometallurgy and the Department of Chemical Engineering (UCT). Special mention to Kathija Shaik for assistance in the Hydromet lab and Sfiso Mkhize for his collaboration on the project.

I would like to thank the UCT Football Club for giving me the opportunity to coach football and to my team (UCT fourth team) for joining me on my MSc journey.



I would also like to thank Arsenal Football Club for allowing me to live up to their motto:

“Victoria Concordia Crescit” – Victory through Harmony.



I would also like to thank Sri Sri Ravi Shankar for his assistance on my path:

“Innovation and creativity spring from within us and spirituality — study of our Self —, is the technology to tap that source.”



## ABSTRACT

Rare earth elements (REEs), La to Lu including Y, are vital elements in manufacture of catalysts and metallurgical industries, and play a critical role in meeting future energy demands, such as through their use in permanent magnets in wind turbines. China has dominated more than 90 % of the REE market, with heavy REE (HREE) clay deposits in South China accounting for 35 % of their total REE output. This has prompted the evaluation of ion-adsorption clay (IAC) deposits in tropical regions outside China, namely Madagascar.

Clay minerals such as kaolinite are part of the phyllosilicate class, containing structures of shared octahedral aluminium and tetrahedral silicon sheets. Isomorphous substitutions within the lattice leads to a charge imbalance, which accounts for negative charge on kaolinite, thus giving the ability to attract REE cations from aqueous solution to the surface of the clay particle. IAC deposits are formed from the tropical weathering of granite with REE enrichment from accessory minerals.

IAC clay samples of two regolith profiles, the pedolith (A1) and saprock (A2, B and F) from northern Madagascar were collected and subjected to a suite of characterisation techniques to investigate the properties of the clay mineral. This included particle size distribution (PSD), X-ray fluorescence (XRF), X-ray diffraction (XRD), quantitative evaluation of minerals by scanning electron microscopy (QEMSCAN), inductively coupled plasma mass spectrometry (ICP-MS), scanning electron microscopy (SEM), and transmission electron microscopy (TEM).

The geochemical leaching characteristics of the clay mineral were investigated using a sequential leaching program, targeting ion-exchangeable REE on kaolinite, halloysite, REE-organic matter and mineral phase. Ammonium sulphate leach experiments were conducted, varying the ionic strength to determine optimum leaching concentrations. Seawater is easily available at the coastal mine, therefore simulated seawater (NaCl) experiments were conducted with the addition of ammonium sulphate to improve the REE recovery. Compound leaching agents were investigated including varying magnesium / ammonium ratios in a sulphate system as well as ammonium in a varying nitrate / sulphate ratio system. The magnesium ion was investigated to correct the Mg deficiency in soils after leaching and the nitrate ion was investigated due to its high ionic permeability in kaolinite. Ion-adsorption clay leaching includes the leaching of impurities such as Al, Fe, Mg, K, Na, Ca and Mn. Ammonium

sulphate experiments with increasing amounts of ammonium acetate were conducted. Ammonium acetate acts as a buffering agent to inhibit the leaching of the main impurity Al.

The texture of sample A1 (5 to 6.5 m) was homogenous, with the QEMSCAN results showing Fe minerals distributed through the kaolinite, giving it a red appearance. The saprock samples A2, B and F have a heterogeneous texture due to the preservation of the primary texture. The QEMSCAN results show that this texture is composed of pure white kaolin, kaolin with red staining due to Fe minerals, tawny staining due to Al minerals and black phases containing Mn minerals. These Mn minerals show Ce deposited as the mineral cerianite, unavailable for ion-exchange. The pedolith sample was light REE (LREE) enriched but depleted in total REE (TREE = 1 503 ppm) compared with the saprock samples (TREE = 7 006 ppm on average). The saprock samples show LREE and HREE enrichment with samples A2 and F having La / Gd ratio of 17.4 and Gd / Lu ratios of 1.2. The more crystalline samples A2 and F (Hinckley index 0.40 and 0.44 respectively) are more REE enriched than the more weathered sample B (Hinckley index 0.32).

The geochemical characterisation of sample A1 showed decreasing REE recovery from LREE to HREE from kaolinite whereas sample A2 showed consistent recovery across the REEs from kaolinite with both showing little Ce recovery. The best TREE recovery for samples A1 and A2 in the chloride system achieved with was  $\text{NH}_4^+$  (44.3 % and 83.1 % respectively) followed by  $\text{Na}^+$  (39.5 % and 72.2 %) and  $\text{Mg}^{2+}$  (28.9 % and 72.1 % respectively). For sample A1 the recovery from the kaolinite fraction was 37.7 %, halloysite 5.1 %, organic 1.6 % and mineral 55.7 %. The proportion of ion-exchangeable REE is increased in sample A2 showing a recovery from the kaolinite fraction of 66.9 %, halloysite 12.7 %, organic 3.5 % and mineral 16.9 %.

The results from increasing the ionic strength of ammonium sulphate shows that TREE leachant concentration increases as the concentration increases but decreases above 0.25 M. This indicates that the ammonium sulphate concentration saturates at 0.25 M and any further lixiviant increase eliminates access to the kaolinite surface. The simulated seawater experiments indicate that some addition of ammonium sulphate is beneficial as the addition of 0.05 M ammonium sulphate almost doubled the TREE leachant concentration. However excess addition of ammonium sulphate above 0.05 M had adverse effects on the leachant concentration of the LREEs.

It was concluded from the compound leaching experiments that the  $Mg^{2+}$  ion can be used to supplement ammonium leaching with the greatest leachant concentration using a  $Mg^{2+}:NH_4^+$  ratio of 1:2 (equal charge). This ratio would produce a high REE leachant concentration while keeping Mg available for plants (flora). Compound leaching with the nitrate ion shows that the greatest REE leachant concentration was with a  $NO_3^-:SO_4^{2-}$  ratio of 2:1 (equal charge) due to increased nitrate ion permeability. The results from the addition of ammonium acetate as a buffer showed that the buffer inhibited the leaching of Al in both samples A1 and F, with the greatest inhibition at 0.05 M.

The characterisation experiments illustrate the complexity of the *in-situ* clay deposit and further work should use this information to construct leaching models that take into account the heterogeneity of saprock samples. The leaching experiments show that compound leaching can improve REE recovery and further work should incorporate multiple lixiviants in *in-situ* leaching models.



## NOMENCLATURE

$\alpha$	Alpha	Eu*	Unfractionated europium
A, B and A <sub>t</sub>	Hinckley index parameters	Eu <sub>n</sub>	Chondrite normalised europium
Å	Angstrom (10 <sup>-10</sup> m)	Fe	Iron
AD	anno Domini	FEG	Field emission electron gun
Al	Aluminium	Gd	Gadolinium
atm	Atmosphere	g, kg	gram, kilogram
$\beta$	Beta	HAADF	High-Angle Annular Dark Field
B	Boron	Ho	Holmium
(BH) <sub>max</sub>	energy density (kJ/m <sup>3</sup> )	IAC	Ion-adsorption Clay
BSE	Backscattered electron	kV	Kilovolt
Ce	Cerium	La	Lanthanum
CEC	Cation-exchange Capacity	Lu	Lutetium
Co	Cobalt	M	Molar concentration (mol/L)
Cs	Caesium	m, km	Metre, kilometre
Cu K $\alpha$	Copper K-alpha (X-ray energy wavelength)	nm, mm	Nanometre, millimetre
°N, °S	Degree North, degree South	$\mu$ m	Micron (micrometre)
Dy	Dysprosium	mL, L	Millilitre, litre
EDS	Energy Dispersive Spectrometer	M <sub>r</sub>	Molar mass
EDX	Energy-dispersive X-ray spectroscopy	MW	Megawatt
Er	Erbium	nA	Nanoampere
Eu	Europium	Nd	Neodymium

NW-SE	Northwest-Southeast	STEM-BF	Scanning Transmission Electron Microscopy – Bright Field
Pm	Promethium		
ppm	Parts per million (mg/L)		
Pr	Praseodymium	Tb	Terbium
REE	Rare Earth Element	TEM	Transmission electron microscope
REO	Rare Earth Oxide	Th	Thorium
LREE, HREE	Light REE, Heavy REE	Tm	Thulium
TREE	Total REE	Θ	Theta (degree)
rpm	Revolutions per minute	U	Uranium
s	second	W	Watt
Sc	Scandium	WCEDREO	Weathered Crust Elution- Deposited REO
sccm	Standard cubic centimetre per minute	wt %	Weight percent
SE	Solvent exchange	XRD	X-ray Diffraction
SEM	Scanning electron microscope	XRF	X-ray Fluorescence
Sm	Samarium	Y	Yttrium
Std Dev	Standard deviation	Yb	Ytterbium
		γ	Gamma
		Z	Atomic number

## GLOSSARY

The geology definitions were taken from the Oxford Dictionary of Earth Sciences 3<sup>rd</sup> Ed (Allaby, 2008).

- Alkali Basalt** A fine-grained, dark-coloured, volcanic rock characterized by phenocrysts of olivine, titanium-rich augite, plagioclase, and iron oxides.
- Biotite** A common rock-forming silicate mineral; a member of the mica group  $K_2(Mg,Fe)_6[Si_3AlO_{10}]_2(OH,F)_4$ , in which the Mg/Fe ratio is less than 2 : 1.
- Breccia** Coarse sedimentary rock, may also be applied to angular volcanic rocks from a volcanic vent.
- Caldera** A roughly circular topographic and structural depression, varying in diameter from about 1 to 100 km, and formed by the foundering and collapse of a magma chamber roof into its underlying magma body.
- Carbonatites** Igneous rocks consisting largely of carbonate minerals calcite ( $CaCO_3$ ) and dolomite ( $CaMg(CO_3)_2$ ) and sometimes containing REE minerals bastnaesite ( $(Ce,La,Nd)(CO_3)F$ ) and parisite ( $Ca(Ce,La)_2(CO_3)_3F_2$ ).
- Cenozoic** Era of geological time extending from about 65.5 million years ago to present.
- Clay minerals** Members of the phyllosilicates (sheet silicates) with related chemistry, all are hydrous aluminium silicates with layered structure; layers of silicon tetrahedra ( $SiO_4$ ) of composition  $(Si_4O_{10})^{4-}$  are joined to Al-O layers (gibbsite-type layers) or (Mg,Fe)-O layers (brucite-type layers). 1 : 1 sheet silicates have one Si-O layer coupled to one brucite or gibbsite layer and include the serpentine group and the kaolinite group of clays; 2 : 1 sheet silicates have two Si-O layers joined to one brucite or gibbsite layer and include the smectite and illite groups of clays, bentonite and montmorillonite, as well as talc and the mica group; 2 : 2 sheet silicates have two Si-O layers joined to two brucite or gibbsite layers and include the chlorite group. It is difficult to distinguish clay minerals by hand or under the microscope, so sophisticated techniques of X-ray diffraction and scanning electron microscopy (SEM) are used to determine the precise clay mineral under investigation.

Dyke	Cross-cutting tubular intrusion, most being vertical or near vertical. A Dyke set is a suite of dykes whose alignment is parallel, reflecting their placement from a common source or under a common stress regime.
Eluviation	One of the main processes involved in laterisation where clays and solutes are removed from suspension in a particular horizon.
Fractionation	The separation process in which a certain quantity of a mixture (gas, solid or liquid) is divided during phase transition into a number of smaller fractions in which the composition varies according to a gradient.
Granite	A light-coloured coarse grained igneous rock consisting of quartz (at least 20 %), alkali feldspar and mica (biotite and/or muscovite).
Igneous	Broad classification for rocks that have crystallized from a magma.
Illuviation	One of the main processes involved in laterisation where material is accumulated, usually at a lower level.
Intercalate	Insertion of molecule between the layers in a crystal lattice.
Kaolin	General term used to describe all the clay minerals listed: kaolinite, dickite, nacrite and halloysite.
Kaolinite	A very important group of clay minerals belonging to the 1 : 1 group of phyllosilicates (sheet silicates), and with the general formula $Al_4(Si_4O_{10})(OH)_8$ , kaolinite represents the final product from the chemical weathering of feldspars to give clays.
Laterite	Weathering product of rock, composed mainly of hydrated iron and aluminium oxides and hydroxides, and clay minerals, but also containing some silica. It is related to bauxites and is formed in humid, tropical settings by the weathering of such rocks as basalts.
Lithophile	Part of the Goldschmidt classification, grouping chemical elements to preferred hosts within the Earth. Lithophile (rock-loving), siderophile (iron-loving), chalcophile (sulphur-loving) and atmophile/volatile (gas-loving).

Ligand	Ion or molecule that binds to a central metal atom to form a coordination complex.
Massif	A very large topographic or structural feature, usually of greater rigidity than the surrounding rock.
Metamorphic	Broad classification for rocks formed by the recrystallisation of pre-existing rocks in response to a change of pressure and/or temperature.
Miller index	Notation system in crystallography for planes in crystal (Bravais) lattices, determined by three integers $h$ , $k$ , and $l$ (the Miller indices) written as $(hkl)$ . By convention, negative integers are written with a bar (as in $\bar{1}$ for $-1$ ) usually written in lowest terms so that their greatest common divisor should be 1.
Mischmetal	An alloy of REEs with a typical composition of 50% cerium and 25% lanthanum, with small amounts of neodymium and praseodymium.
Pedogenesis	The natural process of soil formation, including a variety of subsidiary processes such as humification, weathering, leaching, and calcification.
Pedolith	Upper part of the regolith profile, characterized by complete destruction of rock fabric and leaching of all but the most stable elements. This zone is dominated compositionally by Si, Al, and ferric Fe occurring mainly in kaolinite, quartz, and hematite/goethite.
Pegmatite	An extreme igneous rock produced in the final stages of a magma's crystallisation. They are characterised as 'extreme' due to the exceptionally large crystals, which sometimes contain rare elements, attributed to low-viscosity fluids that allow ions to be very mobile.
Peralkaline	A chemical classification applied to felsic igneous rocks in which there are more molecules of $(Na_2O + K_2O)$ than of $Al_2O_3$ .
Pyroxene	An important group of inosilicates (chain silicates) comprising the orthorhombic pyroxenes (orthopyroxenes) and the monoclinic pyroxenes (clinopyroxenes) with the general formula $XYZ_2O_6$ , where $X = Mg, Fe, Ca, \text{ or } Na$ ; $Y = Mg, Fe, Fe^{3+}, \text{ or } Al$ ; and $Z = Si$ (and some Al substitution).

Regolith	General term for the layer of unconsolidated (non-cemented), weathered material, including rock fragments, mineral grains, and all other superficial deposits, that rests on unaltered, solid bedrock. It reaches its maximum development in the humid tropics. Soil is regolith that often contains organic material and is able to support rooted plants.
Rhyolite	A fine-grained, extrusive, igneous rock, consisting of essential quartz, alkali feldspar, and one or more ferromagnesian minerals.
Saprolith	The base of a lateritic regolith profile, characterized by highly weathered rock where the primary texture and fabric is still preserved.
Sedimentary	Rock formed by the deposition and compression of mineral and rock particles, often including material of organic origin and exposed by various agencies of denudation.
Syenite	A saturated, coarse-grained, igneous rock consisting of essential alkali feldspar and ferromagnesian minerals (biotite, hornblende, arfvedsonite, aegirine-augite, and/or aegirine) and accessory apatite, zircon, and iron oxides. The feldspar constitutes more than 65% of the rock.

## TABLE OF CONTENTS

Acknowledgements.....	iii
Abstract.....	v
Nomenclature .....	viii
Glossary.....	ii
Table of Contents.....	vi
List of Figures .....	x
List of Tables .....	xv
1. Introduction.....	1
1.1. Rare Earth Elements (REEs).....	1
1.2. Application of REEs.....	3
1.3. Feasibility Criteria.....	4
1.4. Sourcing REEs .....	6
1.5. Problem Statement .....	9
1.6. Objectives.....	10
2. Literature Review .....	11
2.1. Rare Earth Elements.....	11
2.1.1. Chemical and physical properties.....	11
2.1.2. Production of Rare Earth Elements .....	14
2.2. Clay Minerals.....	17
2.2.1. Classification and structure of clay minerals .....	17
2.2.2. Kaolin structure and properties.....	18
2.2.3. Cation-exchange capacity .....	20
2.2.4. Halloysite-7Å and Halloysite-10Å .....	22

2.2.5.	Crystallinity .....	22
2.2.6.	Morphology.....	23
2.2.7.	Interactions with organic compounds and salts.....	26
2.2.8.	Formation of clay minerals .....	26
2.2.9.	Laterite regolith formation .....	30
2.2.10.	REE enrichment .....	33
2.2.11.	Vegetation .....	35
2.3.	<i>In-situ</i> Ion-adsorption Clays .....	36
2.3.1.	<i>In-situ</i> leaching.....	36
2.3.2.	Properties of ion-adsorption clays.....	38
2.3.3.	Current work.....	39
2.4.	Research Approach .....	42
3.	Experimental Methodology.....	44
3.1.	Materials .....	44
3.1.1.	Regional geology.....	44
3.1.2.	Sample preparation .....	46
3.1.3.	Reagents.....	46
3.2.	Characterisation Techniques.....	47
3.2.1.	PSD (Particle Size Distribution) .....	47
3.2.2.	XRF (X-ray Fluorescence) .....	47
3.2.3.	XRD (X-ray Diffraction).....	48
3.2.4.	Halloysite differentiation .....	49
3.2.5.	QEMSCAN (Quantitative Evaluation of Minerals by Scanning Electron Microscopy) .....	50
3.2.6.	SIP (Species Identification Protocol) list development.....	50
3.2.7.	ICP-MS (Inductively Coupled Plasma-Mass Spectrometry).....	51



3.2.8.	Clay digestion .....	51
3.2.9.	SEM (Scanning Electron Microscopy) .....	51
3.2.10.	TEM (Transmission Electron Microscopy) .....	52
3.3.	Batch leach tests .....	52
3.3.1.	Batch-stirred tank reactors .....	52
3.3.2.	Experimental program .....	53
4.	Results and Discussion.....	56
4.1.	Ore Characterisation .....	56
4.1.1.	Samples A1, A2, B and F.....	56
4.1.2.	Particle Size Distribution (PSD) results .....	57
4.1.3.	X-Ray Fluorescence (XRF) results.....	58
4.1.4.	X-Ray Diffraction (XRD) results .....	59
4.1.5.	QEMSCAN results.....	61
4.1.6.	Scanning electron microscopy (SEM) results.....	65
4.1.7.	Transmission electron microscopy (TEM) results.....	66
4.1.8.	ICP-MS results .....	68
4.2.	Lixiviant Tests .....	71
4.2.1.	Geochemical characterisation .....	71
4.2.2.	Simulated Seawater .....	73
4.2.3.	Compound lixiviants.....	74
4.2.4.	Ionic strength .....	75
4.2.5.	Inhibitor addition .....	76
5.	Conclusion and Recommendations .....	78
5.1.	Sample Characterisation .....	78
5.2.	Batch leach tests .....	79
	References .....	81

6.	Appendices .....	xix
6.1.	Introduction.....	xix
6.1.1.	Rare Earth Elements and their uses.....	xix
6.1.2.	Locations of major REE reserves.....	xix
6.2.	Methodology.....	xx
6.2.1.	Reagents.....	xx
6.2.2.	Sip list development .....	xxi
6.3.	Results and Discussion .....	xxvi
6.3.1.	XRF trace elements .....	xxvi
6.3.2.	Hinckley Index calculations.....	xxvi
6.3.3.	QEMSCAN blocks .....	xxvii
6.3.4.	Fe QEMSCAN images .....	xxxiii
6.3.5.	Mn QEMSCAN images.....	xxxv
6.3.6.	Ce QEMSCAN images .....	xxxviii
6.3.7.	Zircon QEMSCAN images .....	xlii
6.3.8.	SEM secondary electron images.....	xlii
6.3.9.	ICP-MS.....	xliii
6.4.	Ethics Clearance .....	xliv

## LIST OF FIGURES

Figure 1.1 Standard periodic table of the elements, highlighting location of REEs (Helmenstine, 2017) .....	1
Figure 1.2 Relative abundance of the chemical elements in the Earth's upper continental crust (major industrial metals in bold, precious metals in italic) (USGS, 2002) .....	2
Figure 1.3 Diagram of REE usage with associated REE elements in brackets (Penchoff, 2013) .....	3
Figure 1.4 Advancements in energy density $(BH)_{\max}$ (kJ/m <sup>3</sup> ) of hard magnetic materials in the 20 <sup>th</sup> century and with corresponding decrease in magnet size (Gutfleisch, 2000) .....	4
Figure 1.5 Identification of critical REEs to the future of clean energy (DoE, 2011) .....	5
Figure 1.6 Locations of major REE reserves (see legend in Appendix 6.1.2) with shaded area on 23.4 °N and 23.4 °S latitudes showing favourable conditions for ion-adsorption clay formation (adapted from Papangelakis and Moldoveanu, 2014; McGill, 2000) .....	7
Figure 1.7 Global REE production between 1905 and 2015 (Zhou <i>et al.</i> , 2016) .....	8
Figure 1.8 Political cartoon illustrating the tensions between 'The West' and China over Chinese export quotas being increased (Luo, 2012) .....	8
Figure 2.1 Lanthanide Contraction effect shown by the decrease in ionic radius with increasing atomic number (Krishnamurthy and Gupta, 2004) .....	11
Figure 2.2 Plot of LREE slope La / Gd against Eu anomaly Eu / Eu* for select REE bearing ore types (adapted from Castor and Hedrick (2006)) .....	13
Figure 2.3 Beneficiation flowsheet of the Bayan Obo deposit ore (Zhi Li and Yang (2014)) .....	14
Figure 2.4 Rare Earth Solvent Exchange (SX) flow diagram for Mountain Pass ore (adapted from Caster and Hendricks, 2006) .....	15
Figure 2.5 REE extraction flow diagram for WCED REO used in southern China (adapted from Vahidi <i>et al.</i> , 2016) .....	16
Figure 2.6 Octahedral aluminium (left) and tetrahedral silicon (right) coordination diagram .....	17
Figure 2.7 A Chemical structure for Kaolinite (Grim, 1962), B tetrahedral lattice (top view), and C octahedral lattice (top view) (highlighted sections indicates unit-cell boundary) .....	19
Figure 2.8 Triclinic lattice structure and values for kaolinite .....	19
Figure 2.9 Halloysite-10Å schematic drawing showing active sites (adapted from Joussein, 2005 and Zhou and Keeling, 2013) .....	21

Figure 2.10 Crystallinity index diffractogram for kaolinite (adapted from Plançon <i>et al.</i> (1988)) .....	23
Figure 2.11 A SEM image of kaolinite (Webmineral.com, 2017), B TEM image of tubular halloysite, C TEM image of spheroidal halloysite (Joussein, 2005) .....	24
Figure 2.12 Main halloysite morphologies as a function of Fe content (Joussein, 2005) .....	25
Figure 2.13 Composition of the feldspar minerals (Earle, 2015).....	27
Figure 2.14 Principles of chemical weathering (Robb, 2005) .....	28
Figure 2.15 Relative mobility of selected ions in aqueous solutions in the surficial environment, on the basis of ionic potential (ionic charge / ionic radius) (adapted from Robb, 2005) .....	29
Figure 2.16 Generalised lateritic regolith profile showing different horizons and a generalised pattern of element mobility within the regolith (adapted from Robb, 2005) .....	31
Figure 2.17 Probable weathering paths in lateritic weathering of granite and dolerite involving kaolinite and halloysite (Western Australia) (adapted from Churchman and Gilkes, 1989) ..	32
Figure 2.18 Sequence of steps illustrating the steps involved in adsorbing metal ions onto a mineral surface (Robb, 2005) .....	33
Figure 2.19 Potential pathways for REE migration and sequestration (adapted from Aide and Aide (2012)).....	34
Figure 2.20 Cross section view of a typical in-situ leach of an ion-adsorption clay (Vahidi, 2016) .....	37
Figure 2.21 Proposed leaching mechanisms on platy hydrated halloysite-10Å: 1. Ion exchange phase. 2. Colloid phase. 3. Mineral phase (adapted from Joussein (2005) and Voßenhaul <i>et al.</i> (2015)).....	38
Figure 3.1 Geological map of Madagascar, with locality shown to the left, showing the location of the complexes in the Ampasindava peninsula (Estrade <i>et al.</i> , 2014) .....	44
Figure 3.2 Geological map showing Tsarabariabe and Ampasibitika intrusions (Estrade <i>et al.</i> , 2014) .....	45
Figure 3.3 Pit excavation showing pit sampling procedure, manual techniques and samples received (A1 (5 – 6.5 m), A2, B and F (all 6.5 – 10 m)) (Desharnais <i>et al.</i> , 2014) .....	46
Figure 3.4 Batch-stirred reactor experimental setup .....	53
Figure 4.1 Sample B clay and gangue mineral heterogeneity .....	56

Figure 4.2 Particle size versus relative volume of clay samples using the Malvern Masterizer (<38 $\mu\text{m}$ size fraction) .....	57
Figure 4.3 Major oxides determined by XRF for samples A1, A2, B and F .....	58
Figure 4.4 X-ray diffractogram and mineral analysis .....	59
Figure 4.5 Intercalation of formamide showing expansion of halloysite .....	60
Figure 4.6 Sample A1 block mount (left) (block 2) and false colour field scan image (right)..	61
Figure 4.7 Sample F and A2 block mounts (left) (blocks 9 and 4) and false colour field scan image (right).....	62
Figure 4.8 Sample B BSE image (left) showing Mn mineral with Ce scavenged on its surface as shown by the false colour field image (right) .....	63
Figure 4.9 Sample B false colour field image highlighting K-feldspar, Muscovite, Pyrolusite-Kaolinite Interface and kaolinite Fe rich .....	64
Figure 4.10 Sample A2 white kaolin SEM images showing some tubular morphology (left) and highly disordered platy morphology (right).....	65
Figure 4.11 Sample A2 black phase showing Mn minerals (left) and K-feldspar (right) .....	66
Figure 4.12 White phase kaolinite TEM image with element map .....	67
Figure 4.13 Red phase TEM image showing Fe mineral alongside kaolinite with element map .....	67
Figure 4.14 ICP-MS results for the bulk chondrite normalised REE grade .....	69
Figure 4.15 Sample A2 REE concentration distribution among the white, red and black phase compared to homogenised concentration .....	70
Figure 4.16 Sample A1 (top) and A2 (bottom) sequential leach extraction comparing the recoveries between $\text{Na}^+$ , $\text{NH}_4^+$ and $\text{Mg}^{2+}$ respectively (experiments 1, 2 and 3 top; 4, 5 and 6 bottom) .....	71
Figure 4.17 Sample A2 REE concentration in simulated seawater (SS - 0.5 M NaCl) lixiviant with increasing $(\text{NH}_4)_2\text{SO}_4$ (AS) addition .....	73
Figure 4.18 Sample B REE concentration in leachant after addition of compound lixiviants $\text{MgSO}_4$ (MS) and $(\text{NH}_4)_2\text{SO}_4$ (AS) .....	74
Figure 4.19 Sample B REE concentration in leachant after addition of compound lixiviants $\text{NH}_4\text{NO}_3$ (AN) and $(\text{NH}_4)_2\text{SO}_4$ (AS).....	75

Figure 4.20 Sample F REE and impurity concentration with increasing ionic strength of $(\text{NH}_4)_2\text{SO}_4$ (AS) .....	76
Figure 4.21 Sample A1 REE and Al concentration (primary axis, other impurities on secondary axis) in 0.5 M $(\text{NH}_4)_2\text{SO}_4$ (AS) with increasing $\text{NH}_4\text{CH}_3\text{COO}$ (AA) inhibitor.....	76
Figure 4.22 Sample F REE concentration (primary axis, impurities on secondary axis) in 0.5 M $(\text{NH}_4)_2\text{SO}_4$ (AS) with increasing $\text{NH}_4\text{CH}_3\text{COO}$ (AA) inhibitor .....	77
Figure 6.1 Surface selection for SIP list editing (yellow - kaolinite).....	xxi
Figure 6.2 Number of pixels assigned as kaolinite on SIP list as a function of the element range .....	xxii
Figure 6.3 QEMSCAN image of kaolinite with Mn, Ce phases as lighter phases .....	xxiv
Figure 6.4 BSE pixel field (A) and Ce trap pixel allocation (B) shown as green .....	xxiv
Figure 6.5 Progressive mineral assignment using trap (pink) development, C Kaolinite and full trap assigned, D Pyrolusite-kaolinite Interface assigned, E Cerianite-kaolinite interface assigned, F Cerianite assigned .....	xxv
Figure 6.6 Diffractogram for the Hinckley Index calculations shown in Table 6.6 for samples A1, A2, B and F .....	xxvi
Figure 6.7 Sample A1 block mount (left) (block 1) and false colour field scan image (right) .....	xxvii
Figure 6.8 Sample A1 block mount (left) (block 3) and false colour field scan image (right) .....	xxviii
Figure 6.9 Sample A2 block mount (left) (block 5) and false colour field scan images (right) .....	xxviii
Figure 6.10 Sample A2 block mount (left) (block 6) and false colour field scan images (right) .....	xxix
Figure 6.11 Sample B block mount (left) (block 7) and false colour field scan image (right) .....	xxix
Figure 6.12 Sample F block mounts (left) (block 8 and 10) and false colour field scan images (right) .....	xxx
Figure 6.13 BSE QEMSCAN image (left) showing Fe minerals and false colour field scan images (right) .....	xxxiii
Figure 6.14 BSE QEMSCAN image (left) showing Fe minerals with Mn and Ce minerals and false colour field scan images (right) .....	xxxiv

Figure 6.15 BSE QEMSCAN image (left) showing Mn minerals and false colour field scan images (right) .....	xxxv
Figure 6.16 BSE QEMSCAN image (left) showing Mn minerals with Ce minerals and false colour field scan images (right) .....	xxxvi
Figure 6.17 BSE QEMSCAN image (left) showing Mn minerals with Ce minerals and false colour field scan images (right) .....	xxxvii
Figure 6.18 BSE image showing Mn and Ce minerals .....	xxxviii
Figure 6.19 False colour field scan image .....	xxxix
Figure 6.20 BSE QEMSCAN image (left) showing Ce minerals and false colour field scan images (right) .....	xl
Figure 6.21 BSE QEMSCAN image (left) showing Ce minerals and false colour field scan images (right) .....	xli
Figure 6.22 Sample A1 (left) and sample B (right) zircon (bright BSE) mineral images .....	xlii
Figure 6.23 Kaolinite (red phase) SEM secondary electron images .....	xlii
Figure 6.24 Kaolinite (tawny phase - left) and gibbsite (right) SEM secondary electron images .....	xliii
Figure 6.25 Sample A1 red phase REE concentration compared to homogenised concentration .....	xliii
Figure 6.26 Sample B REE concentration distribution among the white, red and black phase compared to homogenised concentration .....	xliv
Figure 6.27 Sample F red phase REE concentration compared to homogenised concentration .....	xliv

## LIST OF TABLES

Table 1.1 Energy Technologies and their Critical Elements (REEs in bold).....	5
Table 1.2 Main REE sources .....	6
Table 2.1 Ground state electronic configurations for Rare Earth Elements (Henderson, 1984) .....	13
Table 2.2 Main REE source content (Papangelakis and Moldoveanu, 2014) .....	15
Table 3.1 Experiment number and lixiviant make up .....	54
Table 4.1 Quantitative analysis of whole rock mineralogy using the Rietveld Method (wt %) .....	60
Table 4.2 ICP-MS results for samples A1, A2, B and F prior to chondrite normalisation .....	68
Table 4.3 LREE and HREE slopes and negative REE anomalies values .....	69
Table 4.4 Geochemical characterisation sequential leach extraction recoveries .....	72
Table 6.1 Rare Earth Elements and their uses .....	xix
Table 6.2 Section 3.1.3 Reagents .....	xx
Table 6.3 Average elemental concentrations for grid selections .....	xxi
Table 6.4 Upper and lower conditions for SIP list mineral kaolinite .....	xxii
Table 6.5 X-Ray Florescence (XRF) trace element results.....	xxvi
Table 6.6 Hinckley Index Calculations (counts) .....	xxvii
Table 6.7 QEMSCAN Blocks 1 to 5 quantitative mineral content .....	xxx
Table 6.8 QEMSCAN Blocks 6 to 10 quantitative mineral content .....	xxxii



# 1. INTRODUCTION

## 1.1. Rare Earth Elements (REEs)

Rare earth elements (REEs) play a critical role in industry for their unique physical and chemical properties. REEs comprise 14 of the 15 elements from the lanthanide series (atomic numbers 57 to 71), excluding the man-made promethium (Pm - 61). Figure 1.1 shows the standard periodic table of elements, highlighting the elements under investigation.

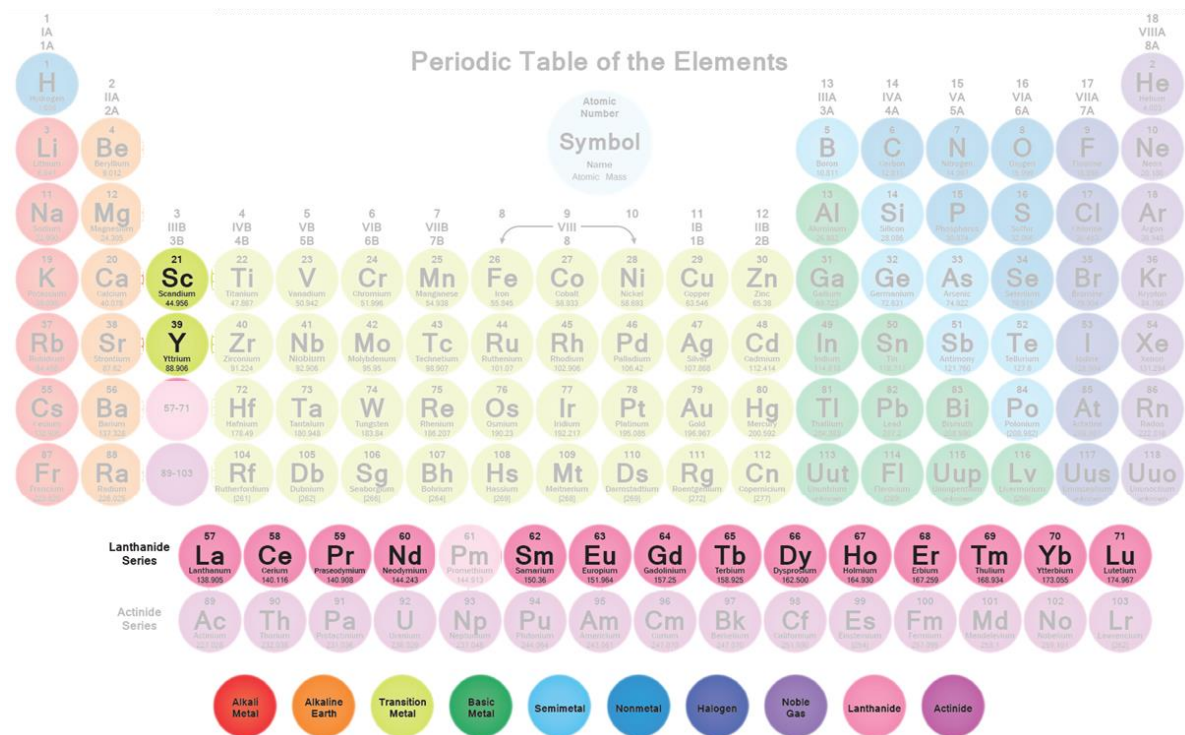


**Figure 1.1 Standard periodic table of the elements, highlighting location of REEs (Helmenstine, 2017)**

Scandium (Sc) and yttrium (Y) are often included with the REEs because they occur in the same ore bodies (Moldoveanu and Papangelakis, 2016), both being electropositive metals with similar reduction potentials to the lanthanides. The ionic radii of  $\text{Sc}^{3+}$  and  $\text{Y}^{3+}$  are 0.745 Å and 0.900 Å respectively, therefore  $\text{Y}^{3+}$  is very similar in size to ionic holmium  $\text{Ho}^{3+}$  (0.901 Å) and would resemble later (heavier) lanthanides but  $\text{Sc}^{3+}$  is smaller and would exhibit considerable differences (Cotton, 2006).

These elements are divided into light rare earth elements (LREEs) and heavy REEs (HREEs), with some authors in China referring also to a middle group (MREEs). The LREEs are lanthanum (La), cerium (Ce), praseodymium (Pr), neodymium (Nd), promethium (Pm),

samarium (Sm) and europium (Eu). The HREEs are gadolinium (Gd), terbium (Tb), dysprosium (Dy), holmium (Ho), erbium (Er), thulium (Tm), ytterbium (Yb), lutetium (Lu) and yttrium (Y).

The REEs are chemically similar to each other, invariably occurring in the same minerals, and tend to act as a single chemical entity (Krishnamurthy and Gupta, 2004). This special chemical behaviour delayed the discovery and isolation of these elements for over 160 years, from 1788 to 1941. To this day the problem of separating the elements has been one of the most challenging tasks for this industry.

The etymology for ‘rare’ suggests that the actual description for ‘rare earth elements’ should be ‘difficult to separate’ elements. REEs are actually quite abundant in the Earth’s crust, with LREE cerium being nearly as abundant as copper (Cu) and even HREEs such as dysprosium and terbium being more abundant than gold (Au) or silver (Ag) (Wübbeke, 2013). This is illustrated in Figure 1.2.

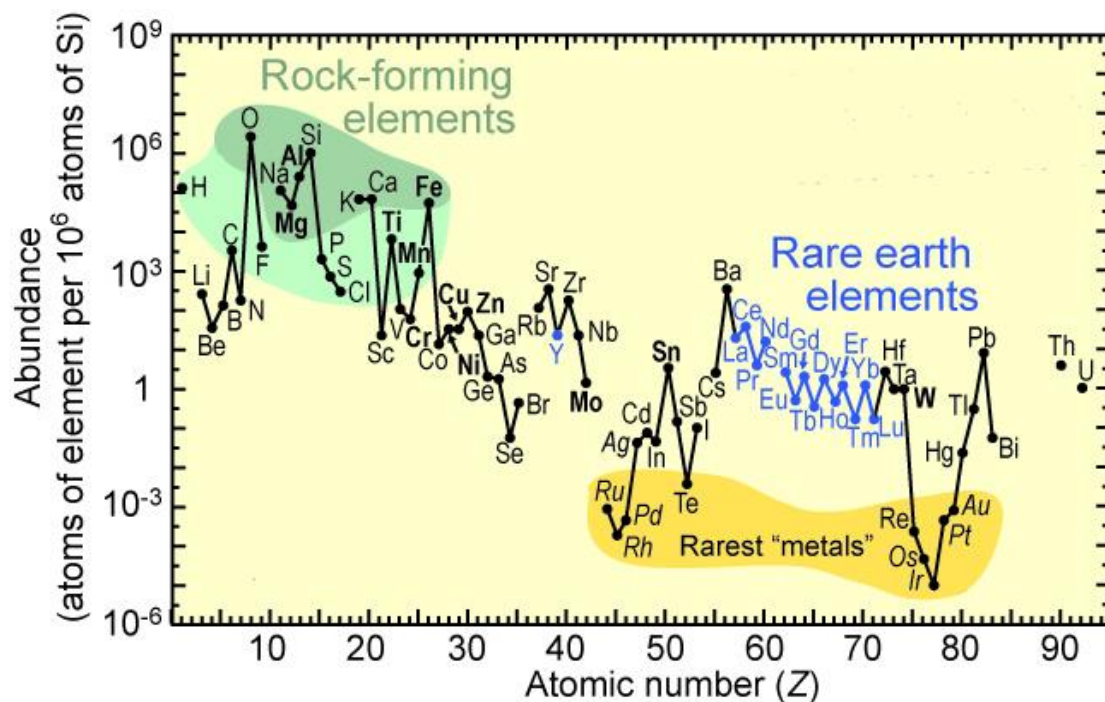


**Figure 1.2 Relative abundance of the chemical elements in the Earth’s upper continental crust (major industrial metals in bold, precious metals in italic) (USGS, 2002)**

The REEs in Figure 1.2 demonstrate a crystal abundance which demonstrates the Oddo-Harkin’s Rule. This rule states that elements with even atomic numbers are significantly more prevalent in the Earth’s crust than their neighbours in the periodic table (Jordens, 2015). This gives the REEs a characteristic ‘zig-zag’ shape shown in Figure 1.2 (blue).

## 1.2. Application of REEs

Rare earth elements are important for our current economy and some REEs are critical for the future of green technologies such as industrial pollution scrubbers and magnets in wind turbines. Figure 1.3 illustrates the uses for REEs and the sectors of the economy in which these elements are found.

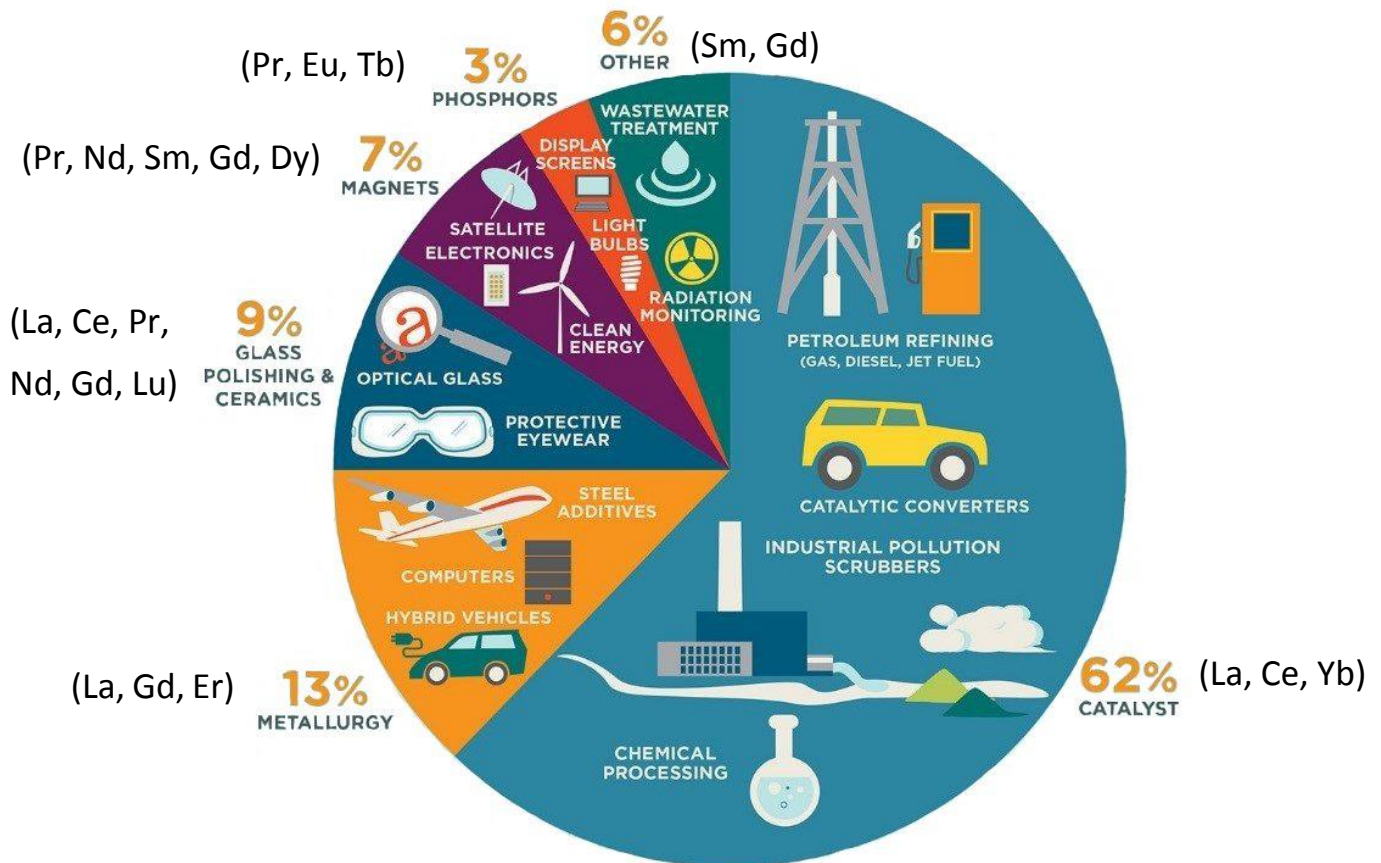


**Figure 1.3 Diagram of REE usage with associated REE elements in brackets (Penchoff, 2013)**

REEs are mainly used as raw materials for high-purity individual REE chemicals, petroleum refining, environment protection catalysts, mischmetal (a type of metallurgical alloy) and polishing powders (Krishnamurthy and Gupta, 2004) (summarized in the Appendix 6.1.1 Table 6.1).

Sometimes REEs are referred to as ‘vitamins’ because of their exclusive properties as well as only small amounts being needed to improve the performance of many final products (Golev *et al.*, 2014). For example, a variety of REEs (Ln, Tb, Pr, Eu, Dy and Gd) are used in small quantities to produce the colours on smartphones screens; Pr, Ga and Nd are used in magnets

in the speakers and microphone, with Nd, Tb and Dy compounds used in the vibrational unit of smartphones.

The properties of REEs allow for them to be used to reduce the size of components and applications (Chakhmouradian and Wall, 2012). This property of high magnetic density is shown in Figure 1.4.

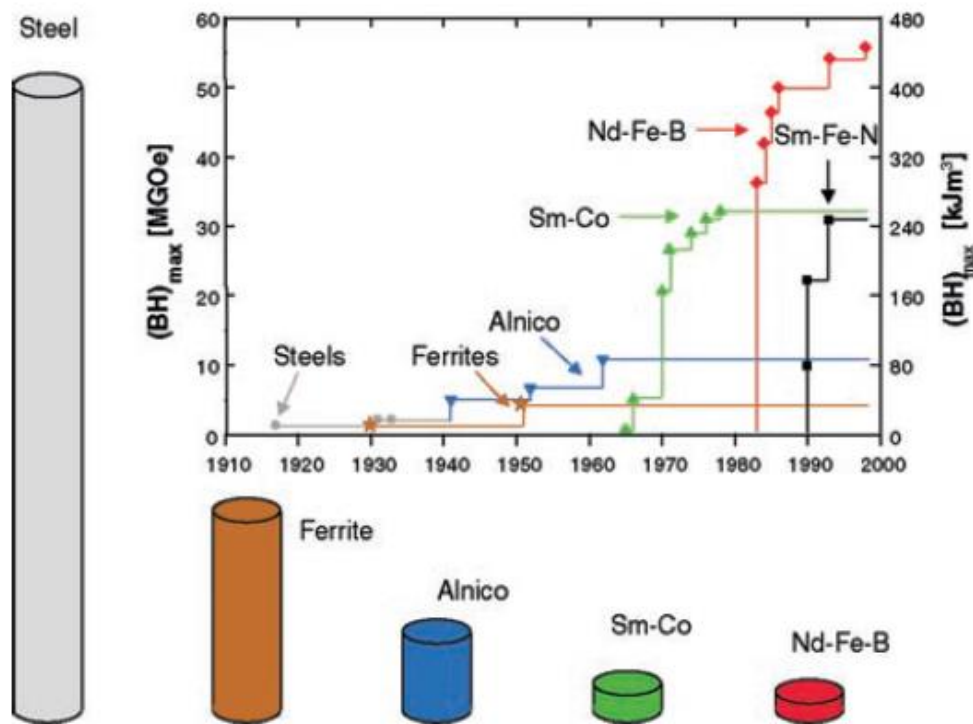


**Figure 1.4 Advancements in energy density  $(BH)_{max}$  ( $\text{kJ/m}^3$ ) of hard magnetic materials in the 20<sup>th</sup> century and with corresponding decrease in magnet size (Gutfleisch, 2000)**

This high magnetic density has resulted in worldwide attention in REEs for their use in hybrid vehicles, wind turbines and military systems (Alonso *et al.*, 2012). To quantify the importance of REEs, it's estimated that wind turbines incorporating NdFeB magnets contain 171 kg of REEs per MW of capacity (Navarro and Zhao, 2014).

### 1.3. Feasibility Criteria

REEs are an important part of the modern day economy and it is their role in clean energy that makes this commodity so valuable for the future. The U.S. Department of Energy have identified the elements most important to the future of clean energy, and together with the relative supply risk for these elements, have constructed a matrix to illustrate which REEs are critical, near-critical and not critical. This information is shown in Figure 1.5.

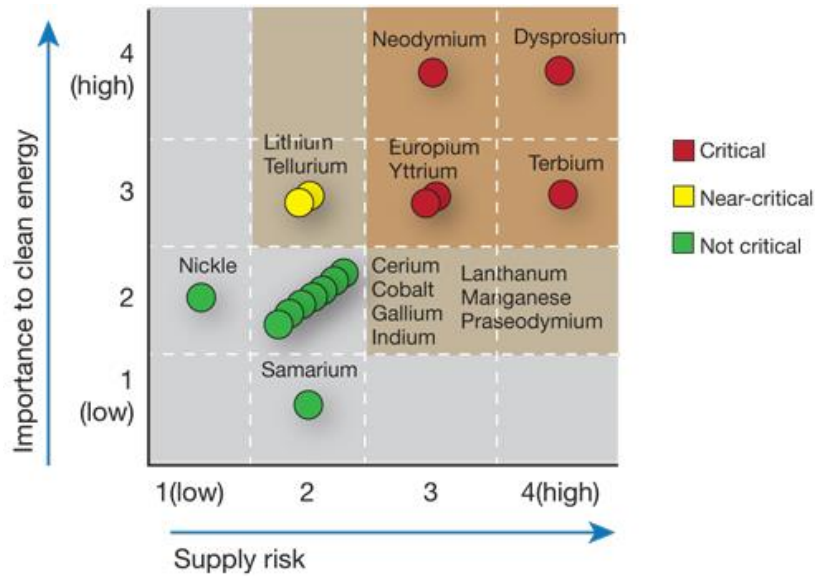


**Figure 1.5 Identification of critical REEs to the future of clean energy (DoE, 2011)**

Despite the similarity in chemical properties, each REE displays unique properties that make them suitable for specific applications, and they usually cannot be interchanged for each other. This critical matrix therefore takes into account this lack of comparable and reliable substitutes, as well as the monopolisation of sources (Golev *et al.*, 2014). This matrix forms part of the criteria when identifying the feasibility of most REE projects. The REE sources with a higher percentage of these critical elements are considered less susceptible to market fluctuations. The energy technologies which are important for energy generation, storage and transport rely on a number of critical elements, summarised in Table 1.1.

**Table 1.1 Energy Technologies and their Critical Elements (REEs in bold)**

Technology	Application	Critical Elements
Batteries	Transportation, electronics, generation systems	Lithium (Li)
Photovoltaic devices	Solar power	Indium (In), Gallium (Ga), Germanium (Ge), Tellurium (Te), Ruthenium (Ru)
Magnets	Generators (wind turbines), motors	<b>Neodymium (Nd), Dysprosium (Dy), Terbium (Tb)</b>
Superconductors	Chemical and medical imaging, transportation	Helium (He), <b>Lanthanides (La to Lu)</b>
Thermoelectric	Power generation	Tellurium (Te), <b>Ytterbium (Yb), Cerium (Ce)</b>
Fuel cells	Power generation, transportation, mobile power sources	<b>Scandium (Sc), Yttrium (Y)</b> , Platinum (Pt), <b>lanthanides (La to Lu)</b>

The availability and cost of critical elements will hinder their application and use, and increasingly REEs and non-REEs are substituted in certain applications. It is relatively easier to substitute one REE for another. For example, SmCo magnets can be replaced by NdFeB magnets which have a greater energy density and are made from cheaper metals, Fe and Nd. Nd is also more abundant than Sm and doesn't require expensive cobalt (Zhou *et al.*, 2016).

#### 1.4.Sourcing REEs

The world holds considerable reserves of REO, estimated at 110 million tons (Wübbeke, 2013). Half of these reserves are located in China with 17.3 % of reserves found in Russia and 11.8 % in the USA. There are also sizeable reserves in Brazil, India, Australia, Canada, and Greenland.

There are about 200 known minerals containing REEs, however because of their geological properties, most are not found concentrated in economically exploitable ore deposits (Golev *et al.*, 2014). The current production of REEs comes from six sources, shown in Table 1.2.

**Table 1.2 Main REE sources**

Source:	Composition:	Production:
Bastnaesite	(Ce,La,Nd)(CO <sub>3</sub> )F	95 % of world's reserves
Monazite	(Ce,La,Nd)PO <sub>4</sub>	
Xenotime	YPO <sub>4</sub>	
Loparite	(Ce,Na,Ca)(Ti,Nb)O <sub>3</sub>	Extracted in Russia only
Apatite	(Ca,REE,Sr,Na,K) <sub>3</sub> Ca <sub>2</sub> (PO <sub>4</sub> ) <sub>3</sub> (F,OH)	Produced as a by-product
Ion-adsorption clays	REE <sup>3+</sup> - Kaolin	REE enriched tropical regions

The first three sources, bastnaesite, monazite and xenotime are the most important, accounting for 95 % of the world's known reserves. Loparite is located in only one country (Russia) and REEs are produced as a by-product from apatite. These REE sources use conventional hard rock beneficiation routes, generally beneficiated by flotation, gravity or magnetic separation processes to produce REE concentrates which are further processed using pyro/hydrometallurgical routes (Jha *et al.*, 2016).

Ion-adsorption clay (IAC) deposits are formed from the tropical weathering of granites. This type of low grade (Table 2.2) secondary mineral deposit has the REEs liberated as cations on the clay surface, which can be recovered by ion-exchange using monovalent salt solutions.

The relative ease of extraction makes ion-adsorption clays attractive for the production of REEs. Ion-adsorption clays form under specific climatic conditions, along latitudes 23.4 °N and 23.4 °S. These conditions, as well as locations for major RE deposits, is shown in Figure 1.6 (McGill, 2000).

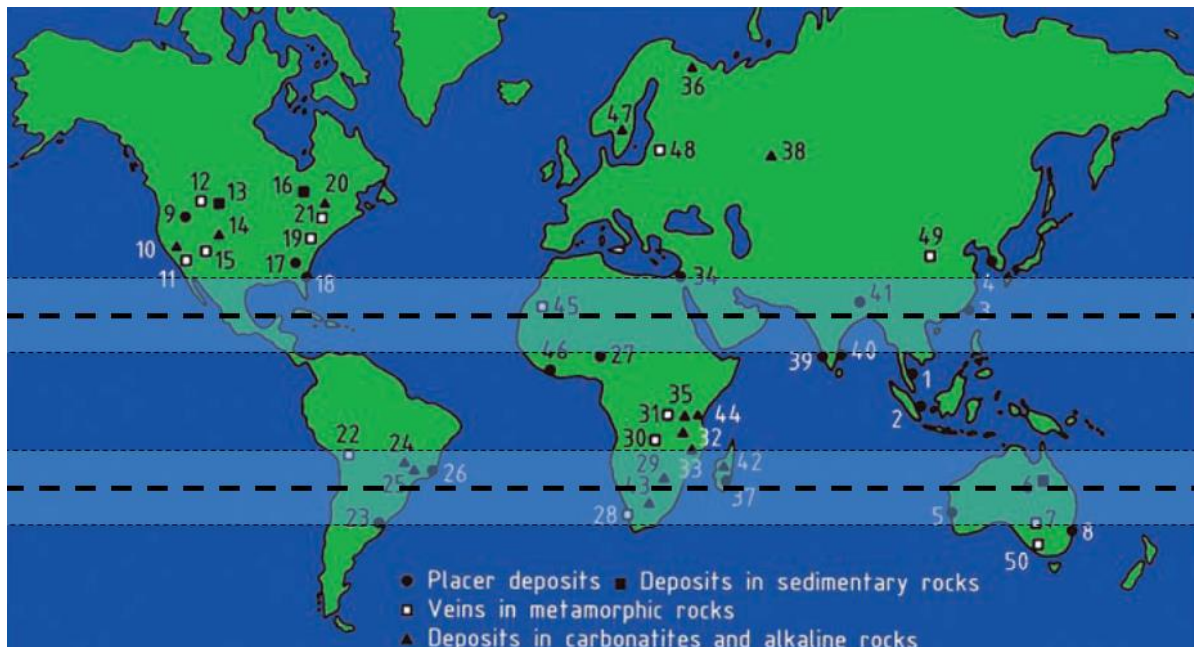


**Figure 1.6 Locations of major REE reserves (see legend in Appendix 6.1.2) with shaded area on 23.4 °N and 23.4 °S latitudes showing favourable conditions for ion-adsorption clay formation (adapted from Papangelakis and Moldoveanu, 2014; McGill, 2000)**

The conditions for IAC formation have led researchers to consider looking for these types of deposits outside China, focussing in the tropical areas of Brazil, Madagascar and parts of Asia (Weng *et al.*, 2015). A granite complex from northwest of Madagascar has shown REE enrichment with a tropical climate favourable for ion-adsorption clay formation (Estrade *et al.*, 2014).

In the late 1970s, early 80s, the U.S. was one of the few countries producing REEs, shown in Figure 1.7. By the mid 90s, China surpassed the U.S. as the world’s largest producer of REEs. Due to environmental issues and cheaper Chinese competition, the large Californian Mountain Pass REE mine was closed down from 2002 to 2010, but attempts to expand and reopen it are currently underway. Today, China dominates the industry at 90 % of the world’s production, with HREE enriched clay deposits in Jiangxi and Guangdong in South China accounting for 35 % of their total RE output.

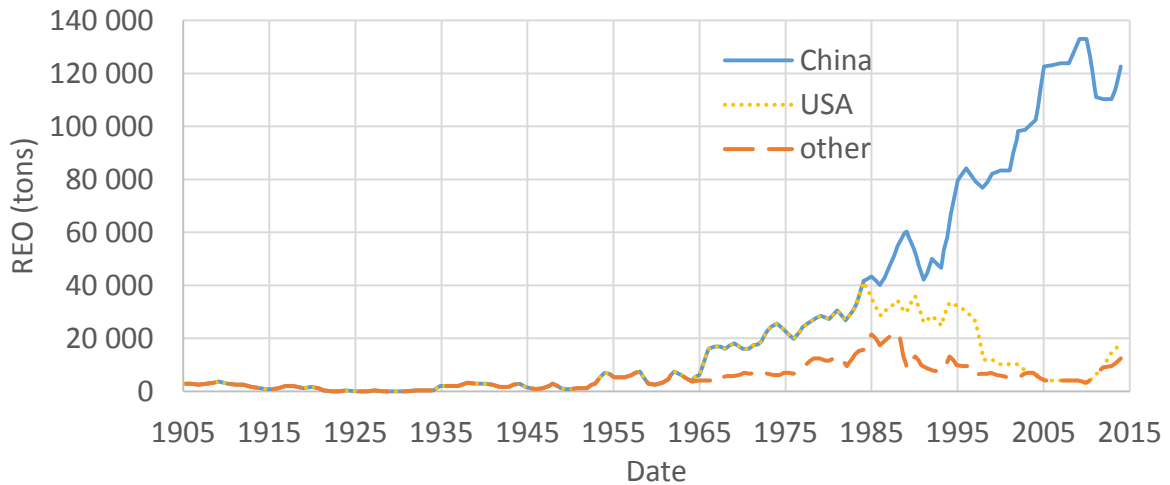


**Figure 1.7 Global REE production between 1905 and 2015 (Zhou *et al.*, 2016)**

China introduced a quota system on their REE exports in 1999. This quota was introduced to restructure the industry in order to try and eliminate the inefficient production, low prices and pollution in their country (He, 2014). In 2010, tensions grew after China increased their quota by another 40 %, resulting in the European Union, Japan and the USA requesting consultations with the World Trade Organisation in March of 2012 for fear of being cut off from these valuable metals. Figure 1.8 shows a political cartoon published in China Daily, illustrating these tensions.



**Figure 1.8 Political cartoon illustrating the tensions between ‘The West’ and China over Chinese export quotas being increased (Luo, 2012)**

This cartoon also illustrates the main issue with REE production, which is the trade-off between REE supply and environmental impact. Due to the relative ease of processing, much



of the Chinese landscape rich in REEs was dug up and leached in barrels or heap leached. This intense and largely unregulated processing, including illegal/ clandestine mining practices, led to a severe loss of vegetation and biodiversity from deforestation and discharge of tailings (Yang *et al.*, 2013). The Chinese government enforced a ban in 2011 on surface mining and batch/heap leaching while implementing in-situ technology (Papangelakis and Moldoveanu, 2014). In *in-situ* leaching the solution is injected at high pressure into the ore body and collected through recovery wells, which avoids surface vegetation clearing and soil disturbance.

The Chinese quota system can only be partly attributed to geopolitical strategies, with the main motive being concerns for resource conservation and environmental protection (Wübbeke, 2013). Since then, the West has stepped up their research into REEs, to reduce their dependence on Chinese supplies.

Due to the relative abundance of La and Ce over other REEs, the production of these REEs has seen an increase in production of all the other REEs that are associated in the same ores. This is referred to as the “balance problem” (Binnemans *et al.*, 2013). The most valuable REEs are Eu and Dy, but increasing their supply would increase the supply of the other REEs which have less demand. Investigations into recycling REEs from spent consumer goods has attempted to reduce this balance problem. Other possible solutions would be to stockpile excess REEs, removing supply from the world market, or to develop new applications for these excess REEs.

### 1.5. Problem Statement

China dominates the REE market with its deposits in REE minerals and HREE enriched ion-adsorption clay deposits. This has led to the investigation of other ion-adsorption clay deposits outside of China. Conventional heap leaching has been banned in China and replaced with *in-situ* leaching. A sample from northwest Madagascar requires mineralogical characterisation of the clay deposit to inform *in-situ* leaching conditions including REE enrichment and impurities present. This characterisation can combine with ion-exchange experiments to determine the samples specific REE leaching behaviour.

## 1.6.Objectives

The investigation herein focuses on mineralogical characterisation and ion-exchange experiments to address the following objectives:

- Determine the bulk clay mineralogy including the bulk and trace chemical composition, particle size distribution and morphology, clay mineral crystallinity, gangue mineral assemblage and LREE and HREE enrichment.
- Determine the geochemical characteristics and REE leaching behaviour of the clay samples including REE association with different mineral assemblages and lixiviant performance.
- Determine optimum leaching conditions including the variation of lixiviant cation and anion choice, ionic strength, compound lixiviants and impurities inhibition.

The suite of characterisation techniques to fulfil the study's objectives include Malvern Particle Size Distribution (PSD), X-ray Fluorescence (XRF), X-ray Diffraction (XRD), Quantitative Evaluation of Minerals by Scanning Electron Microscopy (QEMSCAN), Inductively Coupled Plasma-Mass Spectrometry (ICP-MS), Scanning Electron Microscopy (SEM) and Transmission Electron Microscopy (TEM). All these techniques are outlined in the Experimental Methodology (chapter 3).

Chapter 2 contains all the relevant literature on Rare Earth Elements, their physical and chemical properties, and the properties of clay minerals, their formation and enrichment processes. This section also reviews leaching conditions considered in the literature which leads to the formulation of the batch leaching conditions in chapter 3. Chapter 4 provides the results and discussion from the characterisation and leaching study with conclusions and recommendations given in chapter 5.

## 2. LITERATURE REVIEW

### 2.1. Rare Earth Elements

#### 2.1.1. Chemical and physical properties

Rare earth elements (REEs) have very similar chemical and physical properties. The nature of their electronic configurations gives the REEs this uniformity, comprising mainly of a particularly stable 3+ oxidation state and a small steady decrease in ionic radius as the atomic number increases along the series. This is known as the Lanthanide Contraction effect, shown in Figure 2.1.

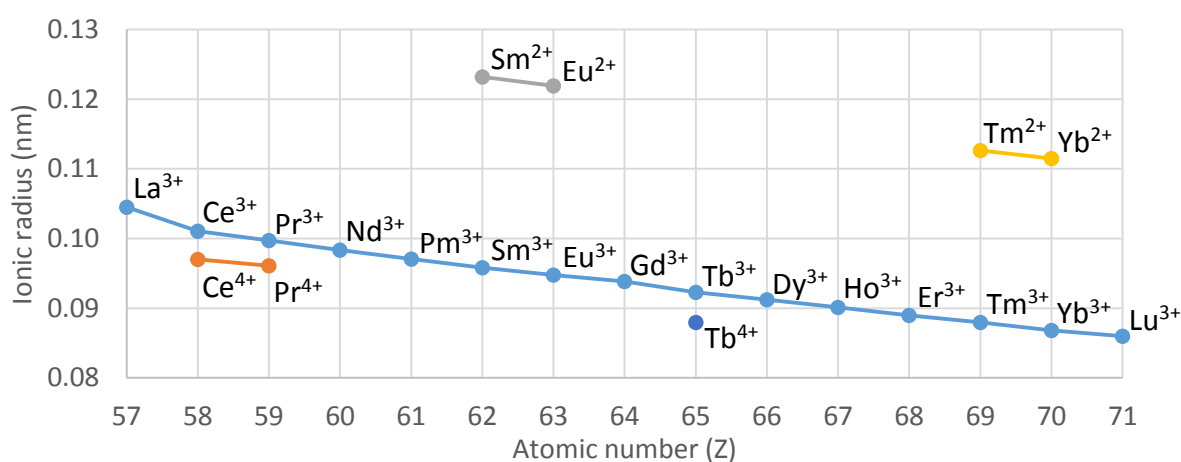


**Figure 2.1 Lanthanide Contraction effect shown by the decrease in ionic radius with increasing atomic number (Krishnamurthy and Gupta, 2004)**

The Lanthanide Contraction effect gives a natural La / Lu slope of 1.22, with LREE (La / Sm) and HREE (Gd / Lu) ratios staying the same at 1.09. This LREE to HREE enrichment can be partially fractionated from one another by several petrological and mineralogical processes. Chemical fractionation occurs from a wide variety of types and sizes of the cation coordination polyhedra in rock-forming minerals and from interactions with secondary minerals.

To determine if geological processes cause any fractionation between the REEs in a particular sample, it is necessary to normalise the concentrations to an external reference material. The common reference material is that of REEs in chondritic meteorites, as it is assumed that there is no fractionation between light and heavy REE in chondrites. The other advantage is that this normalisation eliminates the variation in odd and even atomic number due to the Oddo-Harkin's Rule (Henderson, 1984).

Europium (Eu) is the only REE that occurs in the 2+ valence state under oxygen fugacity conditions found in the Earth's crust (Rudnick and Fountain, 1995). As shown in Figure 2.1, the  $\text{Eu}^{2+}$  ion is larger than its  $\text{REE}^{3+}$  neighbours and has a charge and radius similar to Strontium (Sr). It can therefore substitute for Sr in feldspars, and fractionation of these feldspars will lead to reduced Eu concentrations known as a negative Eu anomaly. A measure for the Eu anomaly is the ratio of the fractionated Eu concentration to the predicted un-fractionated Eu concentration ( $\text{Eu}^*$ ) as shown in equation 2.1.

$$\frac{\text{Eu}}{\text{Eu}^*} = \frac{\text{Eu}_n}{(\text{Sm}_n \text{Gd}_n)^{0.5}} \quad (\text{eq 2.1})$$

The subscript n indicates chondrite normalised values. The REEs  $\text{Sm}_n$  and  $\text{Gd}_n$  neighbour  $\text{Eu}_n$  therefore the geometric mean is used to predict un-fractionated Eu ( $\text{Eu}^*$ ).

The electronic configurations of the REE are given in Table 2.1, for the ground state and the three oxidation states. Lanthanum has electrons in the 5d and 6s orbital, and from cerium onwards the REEs have electrons in the 4f orbital. This orbit is well shielded by the  $5s^2$  and  $5p^6$  sub-shells, and therefore the difference in the progressive number of 4f orbital electrons does not lead to much difference in chemical behaviour, nor to significant ligand field effects.

Promethium (Pm) is indicated in brackets because it does not occur in nature. Europium (Eu) favours the 2+ valence state as the f orbital is stabilised with 7 electrons out of 14. Cerium can be oxidised to 4+ by atmospheric oxygen as the f orbital is stabilised when the f orbital is empty. It is the only tetrapositive rare earth species that is stable in aqueous solutions and solid compounds. The Ce precipitates as mineral cerianite  $\text{CeO}_2$ , leading to a negative Ce anomaly in the vast majority of ion-adsorption clay deposits (Bao and Zhou, 2008). The Ce anomaly calculation follows the same form as equation 2.1 with Ce replacing Eu and the geometric mean between La and Pr used to predict un-fractionated  $\text{Ce}^*$ .

The REEs therefore tend to occur in any natural occurrence as a group rather than single or in combination of a few of their number, and they have a natural positive LREE to HREE slope. They are lithophile (rock-loving), and tend to concentrate in silicate rather than the metal or sulphide phases. Figure 2.2 shows the affinity for LREE accumulation or depletion with a plot of slope La / Gd versus the Eu anomaly for selected REE bearing mineral phases.

**Table 2.1 Ground state electronic configurations for Rare Earth Elements (Henderson, 1984)**

Atomic Number	Symbol	Configuration			
		0	1+	2+	3+
57	La	[Xe]5d <sup>1</sup> 6s <sup>2</sup>	[Xe]5d <sup>2</sup>	[Xe]5d <sup>1</sup>	[Xe]4f <sup>0</sup>
58	Ce	[Xe]4f <sup>1</sup> 5d <sup>1</sup> 6s <sup>2</sup>	[Xe]4f <sup>1</sup> 5d <sup>1</sup> 6s <sup>1</sup>	[Xe]4f <sup>2</sup>	[Xe]4f <sup>1</sup>
59	Pr	[Xe]4f <sup>3</sup> 6s <sup>2</sup>	[Xe]4f <sup>3</sup> 6s <sup>1</sup>	[Xe]4f <sup>3</sup>	[Xe]4f <sup>2</sup>
60	Nd	[Xe]4f <sup>4</sup> 6s <sup>2</sup>	[Xe]4f <sup>4</sup> 6s <sup>1</sup>	[Xe]4f <sup>4</sup>	[Xe]4f <sup>3</sup>
61	(Pm)	[Xe]4f <sup>5</sup> 6s <sup>2</sup>	[Xe]4f <sup>5</sup> 6s <sup>1</sup>	[Xe]4f <sup>5</sup>	[Xe]4f <sup>4</sup>
62	Sm	[Xe]4f <sup>6</sup> 6s <sup>2</sup>	[Xe]4f <sup>6</sup> 6s <sup>1</sup>	[Xe]4f <sup>6</sup>	[Xe]4f <sup>5</sup>
63	Eu	[Xe]4f <sup>7</sup> 6s <sup>2</sup>	[Xe]4f <sup>7</sup> 6s <sup>1</sup>	[Xe]4f <sup>7</sup>	[Xe]4f <sup>6</sup>
64	Gd	[Xe]4f <sup>7</sup> 5d <sup>1</sup> 6s <sup>2</sup>	[Xe]4f <sup>7</sup> 5d <sup>1</sup> 6s <sup>1</sup>	[Xe]4f <sup>7</sup> 5d <sup>1</sup>	[Xe]4f <sup>7</sup>
65	Tb	[Xe]4f <sup>9</sup> 6s <sup>2</sup>	[Xe]4f <sup>9</sup> 6s <sup>1</sup>	[Xe]4f <sup>9</sup>	[Xe]4f <sup>8</sup>
66	Dy	[Xe]4f <sup>10</sup> 6s <sup>2</sup>	[Xe]4f <sup>10</sup> 6s <sup>1</sup>	[Xe]4f <sup>10</sup>	[Xe]4f <sup>9</sup>
67	Ho	[Xe]4f <sup>11</sup> 6s <sup>2</sup>	[Xe]4f <sup>11</sup> 6s <sup>1</sup>	[Xe]4f <sup>11</sup>	[Xe]4f <sup>10</sup>
68	Er	[Xe]4f <sup>12</sup> 6s <sup>2</sup>	[Xe]4f <sup>12</sup> 6s <sup>1</sup>	[Xe]4f <sup>12</sup>	[Xe]4f <sup>11</sup>
69	Tm	[Xe]4f <sup>13</sup> 6s <sup>2</sup>	[Xe]4f <sup>13</sup> 6s <sup>1</sup>	[Xe]4f <sup>13</sup>	[Xe]4f <sup>12</sup>
70	Yb	[Xe]4f <sup>14</sup> 6s <sup>2</sup>	[Xe]4f <sup>14</sup> 6s <sup>1</sup>	[Xe]4f <sup>14</sup>	[Xe]4f <sup>13</sup>
71	Lu	[Xe]4f <sup>14</sup> 5d <sup>1</sup> 6s <sup>2</sup>	[Xe]4f <sup>14</sup> 6s <sup>2</sup>	[Xe]4f <sup>14</sup> 6s <sup>1</sup>	[Xe]4f <sup>14</sup>

[Xe] = 1s<sup>2</sup> 2s<sup>2</sup>2p<sup>6</sup> 3s<sup>2</sup>3p<sup>6</sup>3d<sup>10</sup> 4s<sup>2</sup>4p<sup>6</sup>4d<sup>10</sup> 5s<sup>2</sup>5p<sup>6</sup>

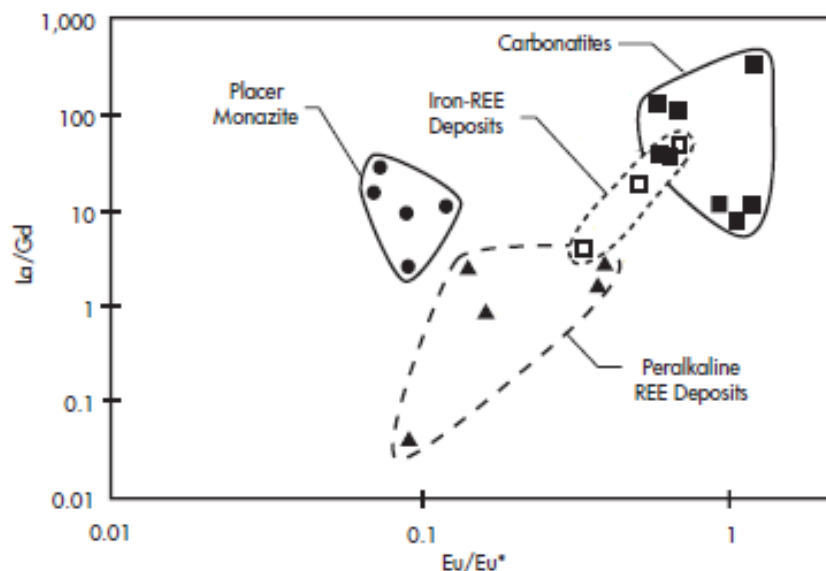


**Figure 2.2 Plot of LREE slope La / Gd against Eu anomaly Eu / Eu\* for select REE bearing ore types (adapted from Castor and Hedrick (2006))**

Carbonatites, such as in Mountain Pass bastnaesite, have an affinity for LREE whereas the low La / Gd values for peralkaline REE deposits indicate relative HREE enrichment. IAC deposits formed from these peralkaline deposits would have a similar HREE enrichment.

### 2.1.2. Production of Rare Earth Elements

China is the primary source of REEs, and 95 % of these reserves are from four types of deposits, namely the Bayan Obo REE-Fe-Nb Ore deposit in Inner Mongolia, Mianning REE Ore Deposit in Sichuan Province, Weishan REE Ore Deposit in Shandong Province and IAC deposits mainly in Jianxi Province but also in Guandong, Fujian and Guanxi Provinces (Caster and Hendrick, 2006). The ion-adsorption clay deposits are also called ‘Weathered Crust Elution-Deposited Rare Earth Ore’ (WCEDREO). This source has been much studied in the southern provinces of China, where the term WCEDREO is primarily used.

The Bayan Obo REE-Nb-Fe deposit is the world largest known REE deposit, and its principal ore is a mixture of bastnaesite and monazite, with magnetite and hematite being the dominant Fe minerals. A beneficiation flowsheet for the Bayan-Obo ore is given in Figure 2.3, and a RE solvent exchange (SX) flow diagram is shown in Figure 2.4 for Mountain Pass ore. The Mountain Pass ore is a carbonatite RE deposit containing 10 – 15 % bastnaesite (Caster and Hendricks, 2006).

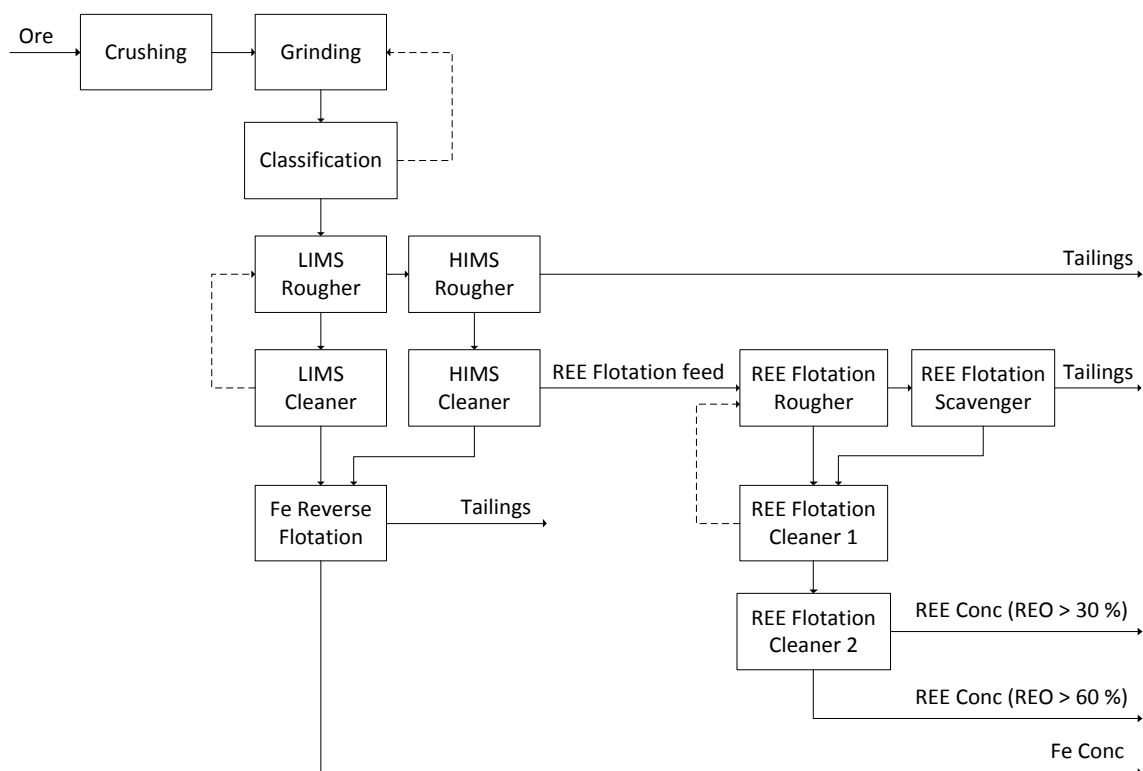


**Figure 2.3 Beneficiation flowsheet of the Bayan Obo deposit ore (Zhi Li and Yang (2014))**

These flowsheets are typical for the beneficiation and separation of high grade ore such as bastnaesite and monazite, illustrated in Table 2.2.

**Table 2.2 Main REE source content (Papangelakis and Moldoveanu, 2014)**

Source:	Composition:	Content:
Bastnaesite	(Ce,La,Nd)(CO <sub>3</sub> )F	65 – 75 wt% LREO
Monazite	(Ce,La,Nd)PO <sub>4</sub>	55 – 65 wt% LREO
Xenotime	YPO <sub>4</sub>	25 – 60 wt% HREE (Y-rich)
Ion-adsorption clays	REE <sup>3+</sup> - Kaolin	0.05 – 0.30 wt% REO

Bastnaesite, monazite, loparite and apatite are the main sources of LREEs, while xenotime and ion-adsorption clays are associated with a higher proportion of HREEs (Golev *et al.*, 2014).

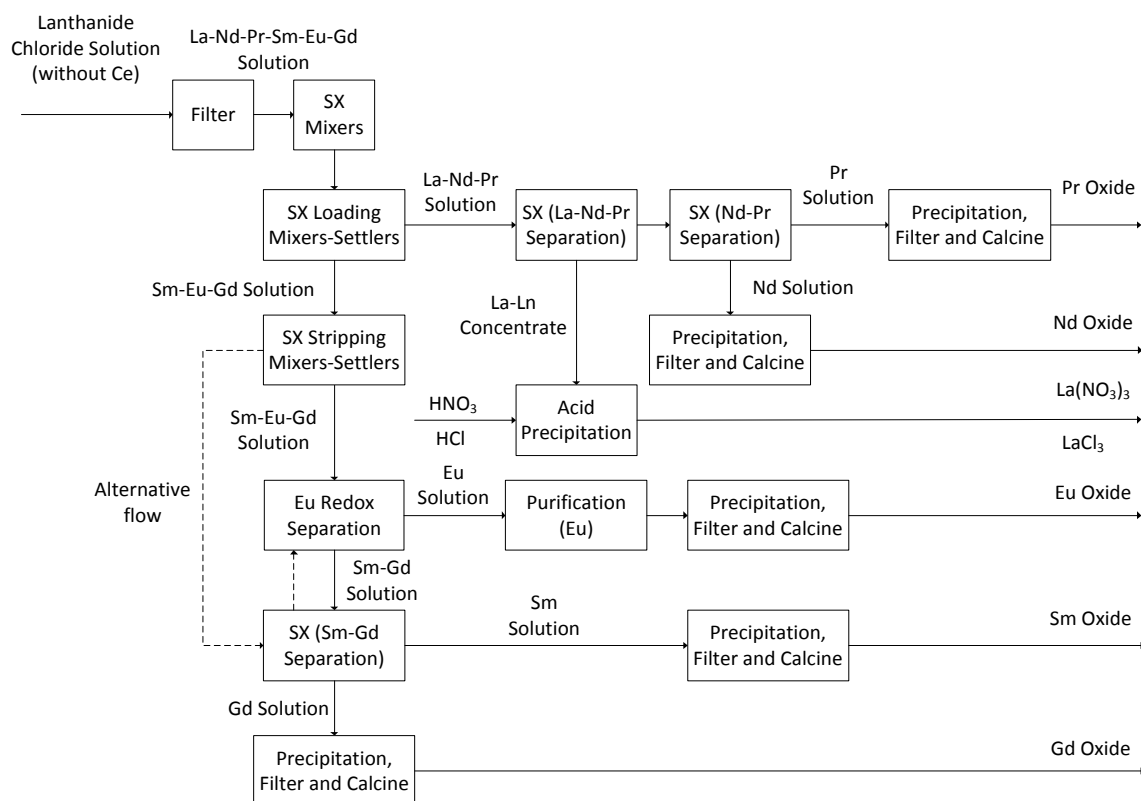


**Figure 2.4 Rare Earth Solvent Exchange (SX) flow diagram for Mountain Pass ore (adapted from Caster and Hendricks, 2006)**

Despite the very low RE content in ion-adsorption clays, it forms one of the most economically viable REE sources. This is due to the simple processing required to recover the REEs, requiring only hydrometallurgical processing with monovalent salt solutions (Moldoveanu and Papangelakis, 2012) to leach the already liberated cations. This reduces the operating costs considerably. In contrast, the richer REE ores require mining and energy intensive ore beneficiation, resulting in significant capital costs as well as highly complex processes to

further treat the ore. Phosphate minerals, monazite and apatite, have the added cost of radioactive treatment associated with U and Th, requiring separation during processing (Papangelakis and Moldoveanu, 2014).

A process flow diagram for the extraction of REEs from IAC used in southern China is given in Figure 2.5. The most important initial consideration is the selection of the mining site during mining exploration, taking into account hydrogeological features and bedrock permeability. Suitable sites are drilled with injection wells (typically 0.6 – 0.8 m diameter) at between 2 and 6 m in depth (Vahidi *et al.*, 2016). A high level pool provides the liquid for the leaching. Seawater can also be used as NaCl acts as a lixiviant for ion exchange, however ammonium sulphate ((NH<sub>4</sub>)<sub>2</sub>SO<sub>4</sub>) is the preferred lixiviant in China in recent decades. The pH of the lixiviant can be altered with addition of H<sub>2</sub>SO<sub>4</sub>.

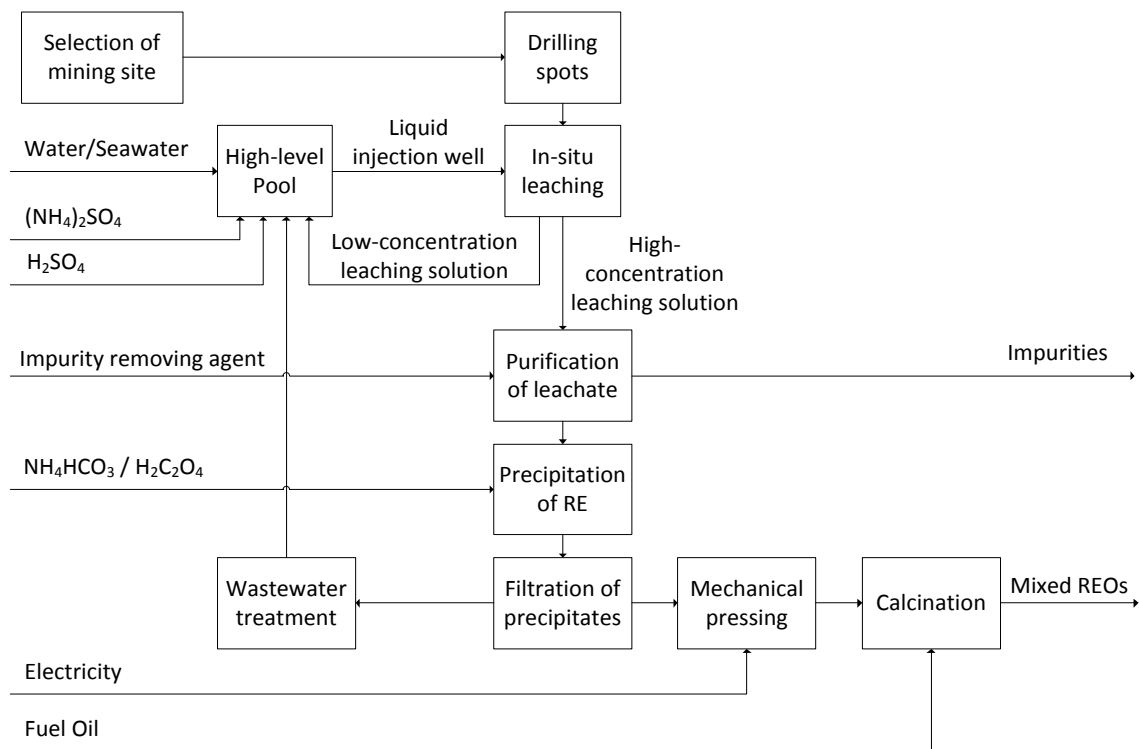


**Figure 2.5 REE extraction flow diagram for WCED REO used in southern China (adapted from Vahidi *et al.*, 2016)**

The high concentration leaching solution is rich in REE but includes impurities such as Al and Fe which need to be removed. The REEs are then precipitated with ammonium bicarbonate (NH<sub>4</sub>HCO<sub>3</sub>) or oxalic acid (HO<sub>2</sub>CCO<sub>2</sub>H). Ammonium bicarbonate is used in industry for its low cost and lower environmental impact than oxalic acid. The drawback of using ammonium



bicarbonate is the difficulty caused in downstream dehydration whereas oxalic acid has the advantage of giving a higher product purity. There are some energy costs associated with pressing the precipitate to remove water and calcining at 750 – 850 °C to produce REOs.

Research has been carried out on recovering REEs from coal (Seredin and Dai, 2012) and coal by-products (Zhang *et al.* (2015); Rozelle *et al.* (2016)), but this work falls outside of the scope for this project.

## 2.2. Clay Minerals

### 2.2.1. Classification and structure of clay minerals

In the 19<sup>th</sup> century, mineralogists used a petrographic microscope to observe minerals. They had an optical limit of 2 µm which led to the definition of clays as being sub-microscopic crystallised particles with a diameter less than this limit. However, quartz, carbonates, metal oxides and other minerals fall under this limit, so now the term clays refers to specific fine-grained layer-lattice aluminosilicates (Parker and Rae, 1998).

Clay minerals are part of the phyllosilicate class, containing structures of shared octahedral aluminium and tetrahedral silicon sheets. The octahedral unit consists of closely-packed oxygens or hydroxyls in which Al, Fe or Mg atoms are embedded in the centre of the octahedral coordination. The octahedral shape and tetrahedral shape are shown in Figure 2.6.

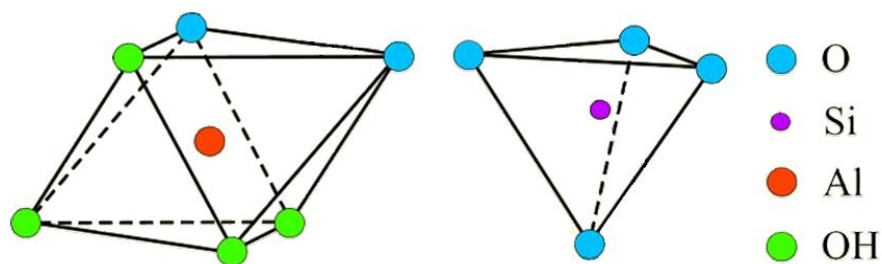


**Figure 2.6 Octahedral aluminium (left) and tetrahedral silicon (right) coordination diagram**

When Al is present, two-thirds of the positions are taken to give gibbsite's formulae of  $\text{Al}_2(\text{OH})_6$ . If Mg is present, then all positions are filled to give brucite's structure of  $\text{Mg}_3(\text{OH})_6$ . The space available for the ion in the octahedral coordination is 0.61 Å. In the silica tetrahedron unit, the Si atom is equidistant to the four oxygens and units are arranged in a hexagonal unit which repeats indefinitely to form a sheet of overall composition  $\text{Si}_4\text{O}_6(\text{OH})_4$ .

The tips of the tetrahedrons are arranged in the same direction with the base of the unit being in the same plane. The space available for the ion in the tetrahedral coordination is 0.55 Å.

Isomorphous substitutions of one cation for another (of similar size but with lesser charge, e.g.  $\text{Al}^{3+}$  for  $\text{Si}^{4+}$  or  $\text{Fe}^{2+}$  for  $\text{Al}^{3+}$ ) leads to a charge imbalance, which accounts for negative charge on clay particles, thus giving the ability to attract REE cations to the surface of the clay particle (Moldoveanu and Papangelakis, 2016).

Observational values for clay minerals show that deformations in the tetrahedral and octahedral structure play an important role and that departures from “ideal” geometry are necessary to fit silica and alumina layers together in the various clay minerals.

Crystalline clay minerals are divided into chain and layer structures, and the layer structures are either 2:1 (two layers of silica tetrahedrons and one di- or tri-octahedron layer) or 1:1 (single silica and alumina layer) layer types. A further division can be made of di-octahedral (3+ charge) or tri-octahedral (2+ charge). Kaolinite is a 1:1 layer type and swelling clays like smectite are a 2:1 layer type.

### 2.2.2. Kaolin structure and properties

Kaolin or ‘kauling earth’ is the general term used for china clay, which was originally mined from a granitic hilly region in China near a village called Kauling in the Jianxi province (Chen *et al.*, 1997). This region is well known for porcelain manufacture in China dating back to AD 800. This clay was found to contain coarse vermicular kaolinite and fine elongated halloysite, as well as minor fine-silt to clay sized mica and quartz. Thus the term “kaolin” is used to describe all the clay minerals: kaolinite, dickite, nacrite and halloysite.

Kaolinite ( $\text{Al}_4(\text{Si}_4\text{O}_{10})(\text{OH})_8$ ) is a very important industrial mineral which is used in large amounts and in a variety of applications. It is a white or near-white in colour and presents good flow properties in large amounts of water, which is vital for its major use in the coating of paper. Relatively pure kaolinites are refractory and fire to a white finish, coupled with its low shrinkage, making them important as ceramic raw materials (Murray, 1999). Usually common impurities such as quartz, goethite, hematite and pyrite need to be removed by wet processing. Primary kaolinite deposits are formed *in-situ* from weathering or by hydrothermal alteration of mainly feldspars such as the well-known primary deposit in Cornwall, southwest England (Robb, 2005).

The structure of kaolinite is shown in Figure 2.7 (Grim, 1962). The structure is composed of a single tetrahedral sheet and a single octahedral sheet combined in a unit with the tips of the silica layer and the aluminium layer forming a common layer.

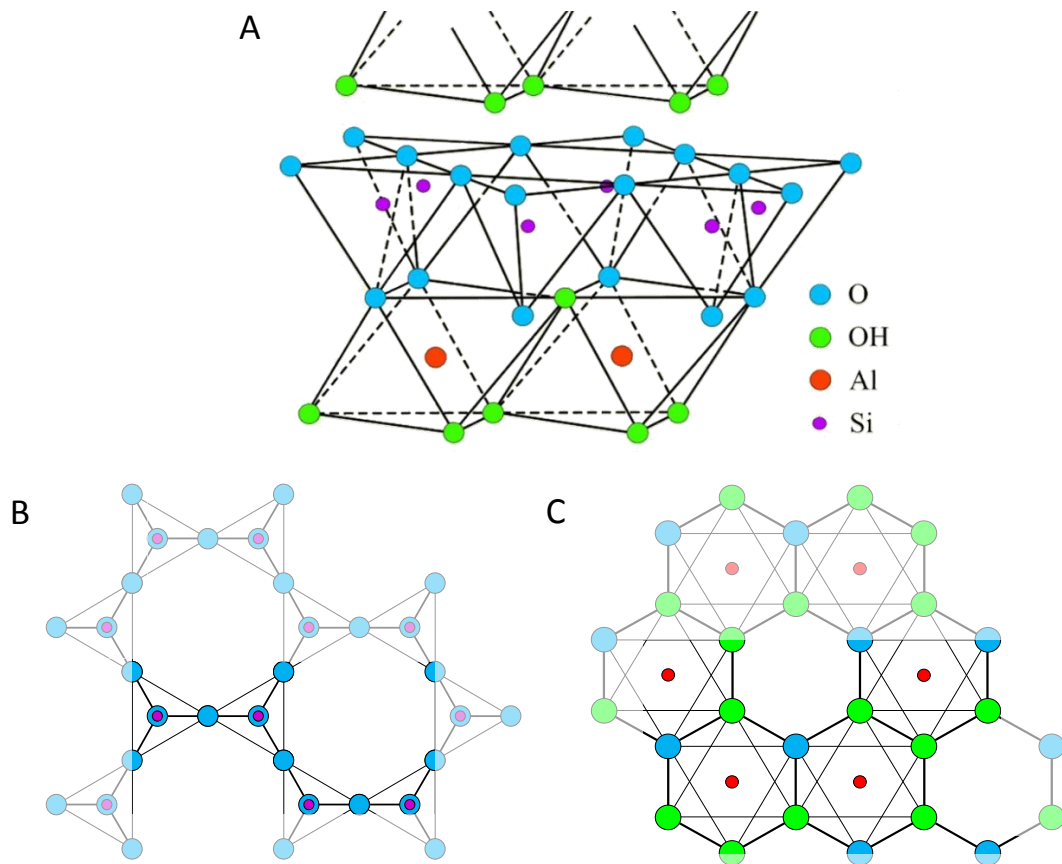


**Figure 2.7 A Chemical structure for Kaolinite (Grim, 1962), B tetrahedral lattice (top view), and C octahedral lattice (top view) (highlighted sections indicates unit-cell boundary)**

Kaolinite has a triclinic crystal lattice, meaning that the three base vectors **a**, **b** and **c** do not equal each other, and all the angles  $\alpha$ ,  $\beta$  and  $\gamma$  can be different. This is shown in Figure 2.8 and the parameters for kaolinite are given.

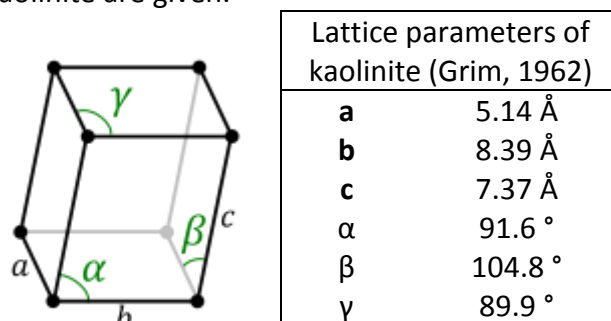


**Figure 2.8 Triclinic lattice structure and values for kaolinite**

The minerals in the kaolinite group are described as continuous in the a- and b-directions and stack one top of each other in the c-direction. This allows them to stack the crystal lattices on top of each other like the pages in a book.

The structural formula for kaolinite is  $(\text{OH})_8\text{Si}_4\text{Al}_4\text{O}_{10}$  and the theoretical oxide composition is  $\text{SiO}_2$  46.5 %,  $\text{Al}_2\text{O}_3$  39.5 % and  $\text{H}_2\text{O}$  13.96 %. Figure 2.7 shows the unit cell as the highlighted section. It is believed that there is very little substitution within the lattice, but evidence suggests that Fe can substitute for Al in relatively poorly crystalline varieties.

Dickite and nacrite are polymorphs of kaolinite, stable under different pressure and temperature conditions. They have similar structures to kaolinite and are listed as clay minerals but they are rarely found in them (Grim, 1962). The term kaolin is used in this study to describe kaolinite and halloysite present in the same sample, and excludes dickite and nacrite.

### *2.2.3. Cation-exchange capacity*

Clays have inherent features that make them attractive for use in a wide variety of applications and understanding these features informs the chemistry involved when dealing with clays. These features include (Zhou and Keeling, 2013):

- 1) Very large surface area/volume ratio that arises from the layered structure
- 2) Small size of the particles in the range of micro- to nano-scale (Johnston, 2010)
- 3) Naturally charged particles leading to relatively strong electrostatic interactions

These properties allow clay minerals to be chemically active and adsorptive, holding REEs onto the clay minerals. These active sites may arise from (Zhou and Keeling, 2013):

- 1) "Broken edge" sites and exposed surface aluminol and silanol groups
- 2) Isomorphous substitutions
- 3) Exchangeable cations
- 4) Hydrophobic silanol surfaces
- 5) Hydration shell of exchangeable cations
- 6) Hydrophobic sites on adsorbed organic molecules

These characteristics are shown in Figure 2.9. Common exchangeable cations include (in order of abundance)  $\text{Ca}^{2+}$ ,  $\text{Mg}^{2+}$ ,  $\text{H}^+$ ,  $\text{K}^+$ ,  $\text{NH}_4^+$ ,  $\text{Na}^+$  and common anions include  $\text{SO}_4^{2-}$ ,  $\text{Cl}^-$ ,  $\text{PO}_4^{3-}$  and  $\text{NO}_3^-$ . Organic ions also play a role and have shown the definite fixation of humic acid and proteins by clay (Grim, 1962).

Cation-exchange capacity (CEC) is the term used to describe the quantity of ions held by a clay mineral, measured in terms of milliequivalents (meq) per 100 g or centimol positive charge per kg clay (cmol<sub>c</sub>/kg). Kaolinite has the lowest CEC at between 3 and 15 meq/100g, next is halloysite at between 5 and 10 meq/100g. Smectite and illite carry greater CECs at 80 – 150 and 10 – 40 meq/100g respectively, due to their swelling nature and 2 : 1 layered structure.

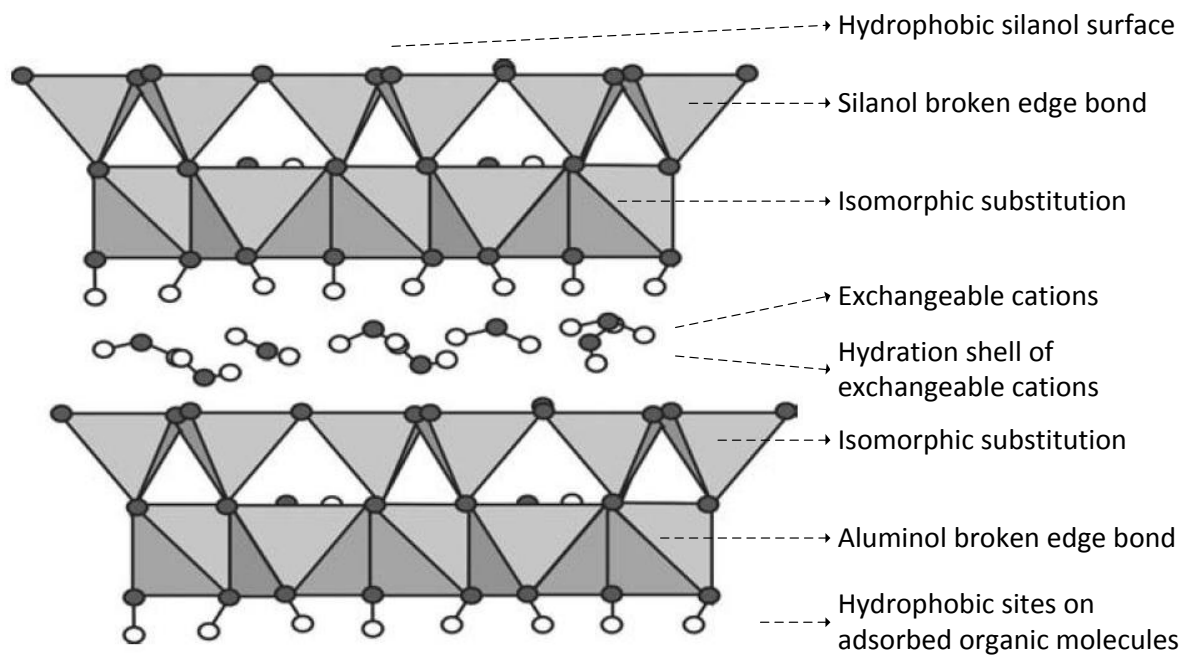
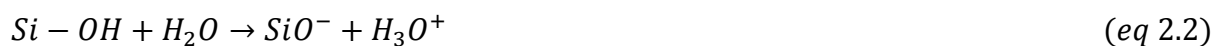


**Figure 2.9 Halloysite-10Å schematic drawing showing active sites (adapted from Joussein, 2005 and Zhou and Keeling, 2013)**

The halloysite-10 Å sheets allow water molecules and hydrated cations to move in between them. However, the major cause of kaolinite and halloysite’s cation capacity is mostly due to broken bonds (Grim, 1962). Broken bonds at the edges of the silica and alumina units would be balanced by adsorbed cations. As the particle size decreases, the number of broken bonds and hence CEC would increase. Broken tetrahedral units would have hydroxyls attached to the silica which would ionise via equation 2.2 to cause a negative charge on the lattice.



It’s been found that 60 - 90 % of REEs are physically adsorbed on kaolin minerals, which can be recovered by simple ion-exchange leaching, with the remaining being chemically bonded, requiring much more acidic conditions to extract (Papangelakis and Moldoveanu, 2014).

#### 2.2.4. Halloysite-7Å and Halloysite-10Å

Halloysite is closely related to, but distinct from, kaolinite. It has the same chemical structure as kaolinite, but with added water  $(\text{OH})_8\text{Si}_4\text{Al}_4\text{O}_{10}\cdot 4\text{H}_2\text{O}$ . There are two main types of halloysite, one is white and porous while the other nonporous and porcelain-like. The difference is related to the halloysite's hydration state. In the past, many researchers thought the most hydrated form of halloysite was a different mineral to the least hydrated form of halloysite. Later work has shown that halloysite can occur in the whole spectrum from fully dehydrated to fully hydrated, showing a variation in the average interlayer water content from zero to two  $\text{H}_2\text{O}$  molecules per  $\text{Al}_2\text{Si}_2\text{O}_5(\text{OH})_4$  unit cell (Churchman *et al.*, 1972). This structure is shown in Figure 2.9.

Hydrated halloysite has a basal spacing of 10 Å which is 3 Å larger than kaolinite. Therefore hydrated halloysite is termed halloysite-10Å and its corresponding dehydrated form halloysite-7Å. The interlayer water is weakly held so halloysite-10Å can readily and irreversibly dehydrate to halloysite-7Å, making it difficult to handle halloysite-10Å without altering its hydration state (Joussein *et al.*, 2005).

#### 2.2.5. Crystallinity

Soil kaolins (kaolinite and halloysite) differ from reference mineral kaolins in a many regards. As the kaolin crystals grow from an *in-situ* environment, they commonly show highly-defective structures, relatively smaller crystal sizes and appreciable amounts of iron in the structure (Hughes *et al.*, 2009). The main discriminating factors when analysing kaolin samples is the particle shape (relative proportions of platy-tubular-spherical particles) and degree of crystal disorder.

The relative degree of crystal perfection can be measured using X-ray diffraction. For many years investigators noticed and ranked the sharpness and resolution of their diffractogram. Highly crystallised kaolin shows sharp narrow peaks on the diffraction pattern, with the peaks getting broader and less distinguished with a decrease in crystallinity and incorporation of impurities.

The Hinckley index was developed by Hinckley (1962) to quantify the degree of crystallinity. With Cu K $\alpha$  source radiation, the peaks at 20.4 ° ( $1\bar{1}0$ ) and 21.3 ° 2 $\theta$  ( $11\bar{1}$ ) are used as the resolution of these peaks improve as crystal perfection improves, where the Miller indices

such as  $1\bar{1}0$  and  $11\bar{1}$  refer to discrete crystal faces. This method, illustrated in Figure 2.10, consists of constructing a line gradient from the dip between peaks  $020$  and  $1\bar{1}0$ , and the background after the  $11\bar{1}$  peak. The heights of  $1\bar{1}0$  (denoted as  $A$ ) and  $11\bar{1}$  ( $B$ ) are measured relative to this gradient line. The index is the sum of  $1\bar{1}0$  and  $11\bar{1}$  peaks relative to the gradient line ( $A + B$ ) divided by the  $1\bar{1}0$  peak relative to the background ( $A_T$ ). This is expressed in equation 2.3.

$$\text{Hinckley Index} = \frac{A + B}{A_T} \quad (\text{eq 2.3})$$

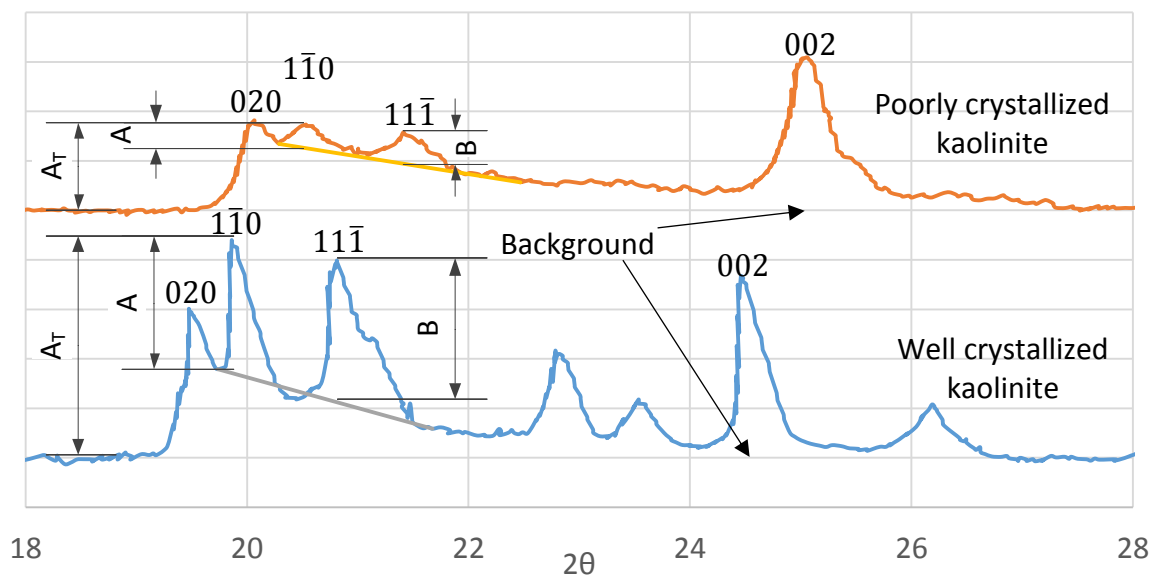


**Figure 2.10 Crystallinity index diffractogram for kaolinite (adapted from Plançon *et al.* (1988))**

#### 2.2.6. Morphology

Clay minerals are characteristically flake-, lath- or needle-like in shape. This affects the suspension behaviour, rheology and surface area of the minerals, with the surface area decreasing from sheet – to lath – to needle. This variety of particle morphology is related to the crystallisation conditions and geological occurrences, affecting the degree of alteration, chemical composition and effects of dehydration (Joussein, 2005). The chemical composition of kaolinite and halloysite can be difficult to determine as Fe oxides are common impurities.

Kaolinite sheets have a platy morphology, whilst the dominant morphology of halloysite is tubular. These tubes can be long and thin, short and stubby, or even emerging from other

tubes. The tubes can extend from 0.02 up to >30  $\mu\text{m}$ , their radius range between 0.05 and 0.5  $\mu\text{m}$ .

The morphology of a clay mineral can be determined from the use of transmission electron microscopy (TEM). This technique, along with scanning electron microscopy (SEM), has been used in the past to distinguish between halloysite and kaolinite. Relative abundance of tubes would approximate the halloysite content, however distinctions based on particle shapes is misleading as some studies identify platy halloysite typical of kaolinite and tubular kaolinite commonly associated with halloysite (Churchman, 1990). The three different kaolin morphologies are shown in Figure 2.11.

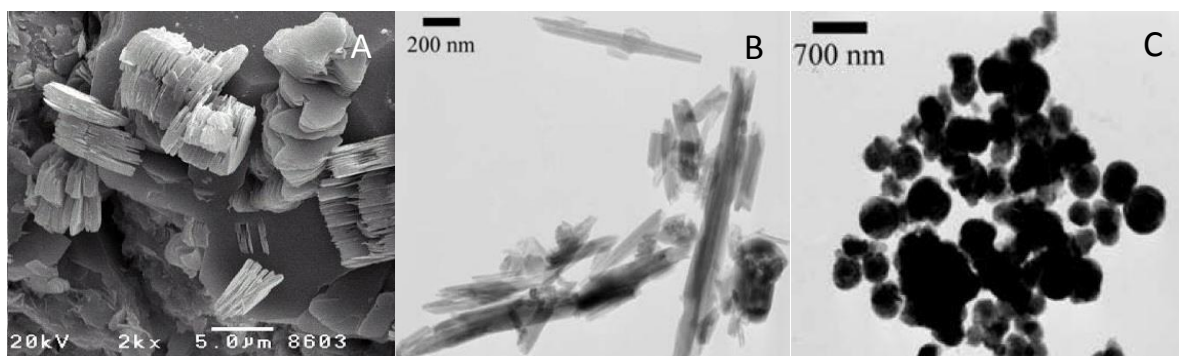


**Figure 2.11 A SEM image of kaolinite (Webmineral.com, 2017), B TEM image of tubular halloysite, C TEM image of spheroidal halloysite (Joussein, 2005)**

Spheroidal halloysite occurs widely, occurring in weathered volcanic ashes and pumices. The diameter of the particles ranges from 0.05 to 0.5  $\mu\text{m}$ . Spherical morphology is related to precipitation from highly supersaturated solutions.

Chemical analysis of halloysite deposits shows significant amounts of Fe, up to 12.8 wt % (Joussein, 2005), however this is largely attributed to Fe oxides native to *in-situ* environments. Although Fe can exchange for Al in the octahedral sheet, it has not been reported to exchange for Si in the tetrahedral sheet for halloysite. Platy kaolinites therefore always contain some amount of Fe, while tubular particles are relatively Fe-poor.

The role of Fe in particle morphology has been well documented (Churchman and Theng, 1984), and Figure 2.12 shows the relationship between the three main morphologies (platy, large and small tubular, and spherical) and the Fe content.



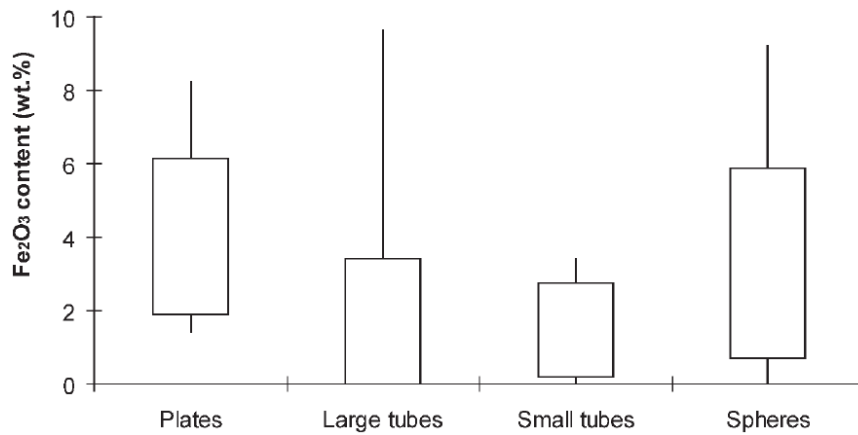


**Figure 2.12 Main halloysite morphologies as a function of Fe content (Joussein, 2005)**

Figure 2.12 shows that the platy morphology contains a relatively larger amount of Fe than tubular particles, with spherical halloysite ranging from almost zero to content similar to platy morphology. The iron content therefore seems to affect kaolinite and tubular halloysite rolling, and spherical morphology is more a factor of crystallisation conditions.

As per Figure 2.8, the long axis of the tube is in the b-direction, as halloysite has a preference to rolling its a-axis. The cause for halloysite rolling lies in the mis-fit of the larger tetrahedral sheet to the smaller octahedral sheets. This misfit causes stress on the basal oxygen plane as well as the inner OH, apical O plane shared by the tetrahedral and octahedral sheets. The stress on the basal oxygens is relieved somewhat by the presence of water and the separation of the layers, but the stress on the shared OH, apical O plane is unaffected by hydration (Singh and Mackinnon, 1996).

The mis-fit can be corrected by either tetrahedral rotation or by rolling of the 1:1 layer. The requirement of these two processes is to equal the dimensions between apical oxygen and inner OH plane. Tetrahedral rotation involves the rotation of adjacent tetrahedral in the opposite directions, thus pulling basal oxygens to the centre of the ring (centre of the ring in Figure 2.7 B) adopting a di-trigonal ring configuration. In the rolling mechanism, basal oxygens are translated towards the interlayer space, contracting the apical oxygen distance.

The fundamental difference in the two mechanisms is simply the direction in which the basal oxygen translates, which is dependent on the hydration state of the halloysite. Non-hydrated structures would have hydrogen bonding as the dominant force to overcome in correcting the misfit. Tetrahedral rotation results in a shorter hydrogen bonds between basal oxygens

and outer OH groups. When hydrated, the hydrogen bonds are weakened allowing for the more efficient mechanism of rolling.

Therefore platy halloysite would be expected to roll once hydrogen bonding has been weakened by hydration, and the reverse is true when prolonged dehydration allows the hydrogen bonding to strengthen, shifting the rolling mechanism to tetrahedral rotation, causing tubes to produce laths by unrolling (Singh, 1996).

Iron plays a deciding factor in this process, as substitution of the larger  $\text{Fe}^{3+}$  cation in the octahedral sheet eliminates the mismatch. This means that the presence of Fe allows layers to adopt planar shapes as opposed to tubes. The content of Fe can also affect the size of the tubes formed, with low levels favouring long tubes and higher levels leading to shorter tubes due to increased nucleation (Joussein, 2005).

#### *2.2.7. Interactions with organic compounds and salts*

The intercalation (inclusion into layered structure) of salts and organic compounds with halloysite and kaolinite are well known in literature (Joussein *et al.*, 2005). This process is significant for estimating the proportion of expandable halloysite from non-expandable kaolinite. Scientifically we can observe the process of intercalation readily with XRD, since intercalation leads to layer expansion along the c axis.

Organic compounds that complex with halloysite are polar, are basic or acidic, and contain two functional groups such as -OH and -NH<sub>2</sub>. A simple and rapid method was developed by Churchman and Theng (1984) for formamide (HCONH<sub>2</sub>) intercalation, which is completed for halloysite in under 1 hr whereas kaolinite needs 4 hr minimum. Other compounds used decrease in the ease of intercalation in the order of: dimethylsulfoxide (DMSO, (CH<sub>3</sub>)<sub>2</sub>SO) > HWG (hydrazine/water/glycerol, NH<sub>2</sub>NH<sub>2</sub>/H<sub>2</sub>O/(CH<sub>2</sub>OH)<sub>2</sub>CH(OH)) > formamide > K-acetate (KCH<sub>3</sub>COO) (Churchman (1990); Theng *et al.* (1984)). A number of salts can replace the monolayer of water in halloysite, and it was found that halloysite intercalates the chlorides of K<sup>+</sup>, Cs<sup>+</sup> and NH<sub>4</sub><sup>+</sup> but not Na<sup>+</sup> or Mg<sup>2+</sup> and Ca<sup>2+</sup> (Wada, 1961).

#### *2.2.8. Formation of clay minerals*

The majority of Earth's crust is made up of silicate minerals, including quartz, feldspar, mica, amphibole, pyroxene, olivine and clay minerals. The building blocks of these minerals is the

silica tetrahedron, and in silicate minerals these are arranged in a variety of ways, from isolated tetrahedrons (nesosilicates such as olivine and zircon) to single chains (inosilicate such as pyroxenes) to 3-dimensional structures (tectosilicate such as feldspars and quartz). The composition of the feldspar group is given in Figure 2.13.

The three main feldspar minerals are potassium feldspar ( $\text{KAlSi}_3\text{O}_8$ ) and two types of plagioclase feldspar, albite (Na only -  $\text{NaAlSi}_3\text{O}_8$ ) and anorthite (Ca only -  $\text{CaAl}_2\text{Si}_2\text{O}_8$ ). The calcium ion ( $\text{Ca}^{2+}$ ) is almost identical in size to the sodium ion ( $\text{Na}^+$ ), 1.00 Å versus 0.99 Å respectively, so there exists a continuous range of solid solution substitution between albite and anorthite in plagioclase. K-feldspar has a slightly different structure to plagioclase due to the large K ion (1.37 Å), and as such Na can only substitute for K at high temperatures in volcanic rocks.

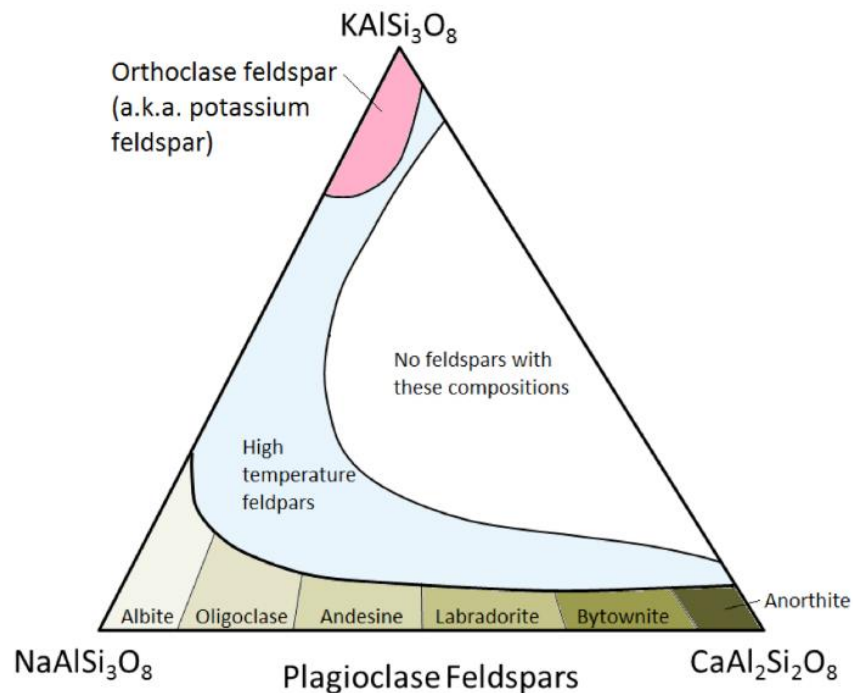
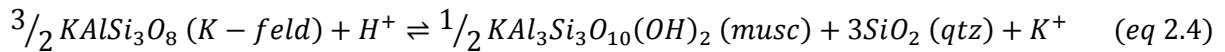


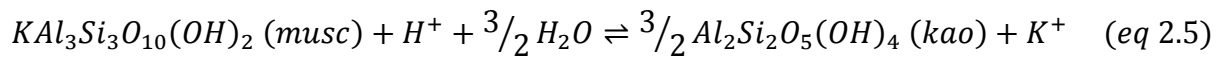
**Figure 2.13 Composition of the feldspar minerals (Earle, 2015)**

Kaolin deposits can be either primary (hydrothermal / residual) or secondary (sedimentary). They are formed *in-situ* from feldspar rich rocks, such as granites and rhyolites. Hydrothermal alteration is the process of fluids passing through a rock and marked by the development of a mineral assemblage that is different to the original rock but reflects its elemental composition. In its simplest form, the hydrothermal fluid is water with its dissociated components  $\text{H}^+$  and  $\text{OH}^-$  as well as the dissolved constituents of the aqueous solution (Robb,

2005). One of the most common forms of alteration in nature is the reaction of K-feldspar to muscovite in the presence of a hydrothermal fluid (Robb, 2005):



If the product is permitted to react further with the hydrothermal fluid ( $H^+$ ), muscovite would react to form kaolinite:



This reaction shows that fluid/rock ratios will change the alteration mineralogy by continued reaction, and generally forms an assemblage of phases.

Apart from hydrothermal alteration, the majority of clay minerals are produced from weathering. The exact process of hydrothermal/weathering clay production is difficult to separate, as weathering fluid would access material previously accessed by high temperature fluids. Chemical weathering can be divided into three main processes, shown in Figure 2.14.

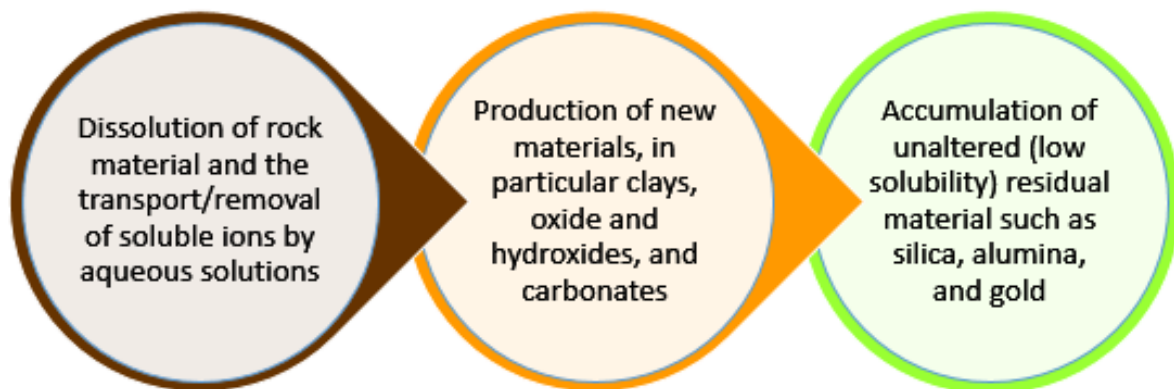


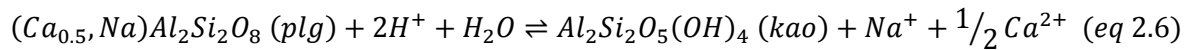
**Figure 2.14 Principles of chemical weathering (Robb, 2005)**

The main chemical processes that contribute to weathering include dissolution, oxidation, hydrolysis, and acid hydrolysis. In the process of weathering, fine clay particles are produced, which promotes cation exchange and further breakdown of minerals in the weathering zone.

Kaolinite is formed from acid hydrolysis of feldspar-bearing rocks in laterites (clay rich soil horizon formed in moist warm climates), whereas illite (2 : 1 clay mineral) forms under more alkaline conditions of feldspars and micas. Smectite also forms under alkaline conditions, from weathered intermediate to basic rocks. Rainfall can also affect the formation of clay

minerals, with smectite forming in arid to semi-arid conditions and kaolinite dominating wetter climates.

Kaolinite is preferentially developed from the plagioclase feldspar in granite, the reaction shown in equation 2.6, releasing Na and Ca into solution. This process is most relevant at acidic pH, and its actual mechanism is more complicated, involving multiple stages during weathering.



The preference for kaolinite to form from plagioclase rather than K-feldspars is due to the ease at which these minerals weather. Minerals which crystallise from a magma at lower temperatures are less susceptible to weathering (Churchman and Lowe, 2012). Therefore volcanic glasses that are basaltic or rhyolitic would weather first, followed by olivines and the plagioclase feldspars. K-feldspars and muscovite are less susceptible to weathering with quartz being the most stable due to its complex silica tetrahedra arrangement. The mobility of the different elements varies considerably during the weathering process, as illustrated in Figure 2.15.

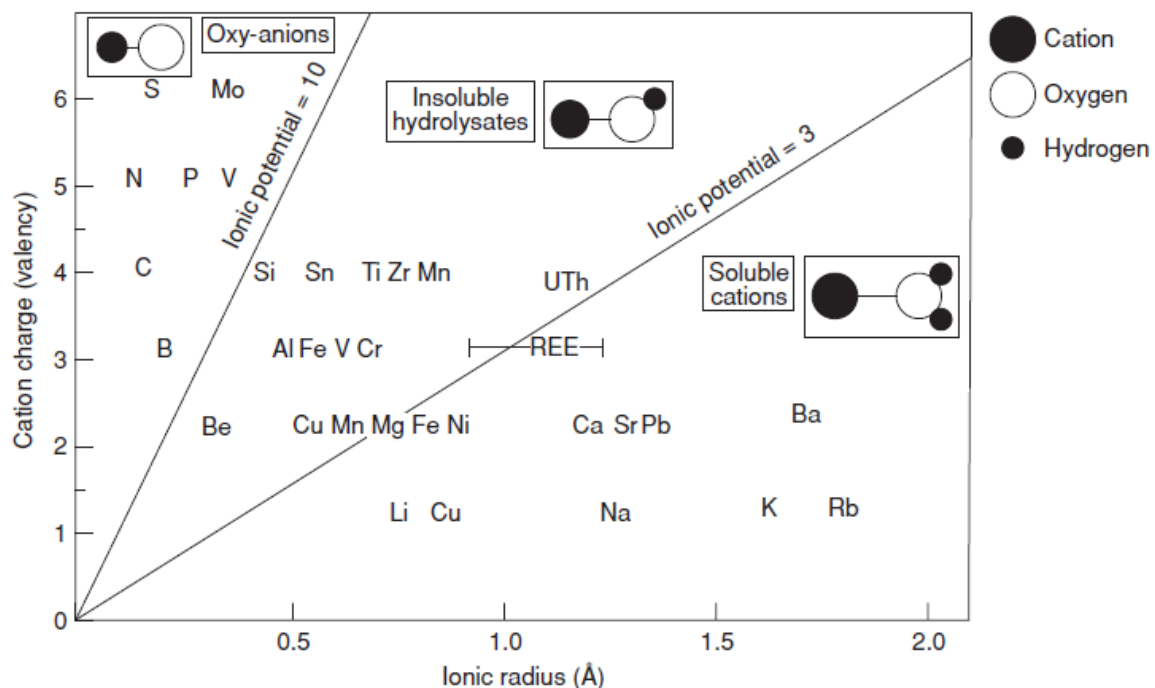
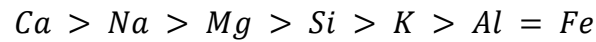
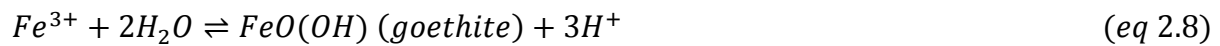
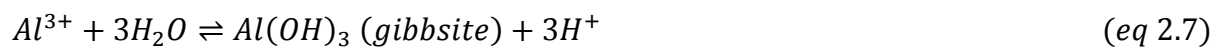


**Figure 2.15** Relative mobility of selected ions in aqueous solutions in the surficial environment, on the basis of ionic potential (ionic charge / ionic radius) (adapted from Robb, 2005)

The elements liberated from the weathering of the feldspars are hydrated cations which will precipitate under alkaline conditions, and are adsorbed on clay minerals. There exists a hierarchy of mobile elements, which follows the order:



Calcium and sodium are released from the easily weathered plagioclase feldspars, magnesium from olivines and pyroxenes, silica from feldspars and potassium from K-feldspars. The hydrolysed elements Al and Fe are relatively soluble in acidic solutions, but precipitate as a result of hydrolysis, as shown in equations 2.7 and 2.8.



The process of mineral breakdown, reaction with acidic solutions and resulting soluble cations and precipitation is most active at fractures, cleavages and lattice defect sites.

#### 2.2.9. Laterite regolith formation

Soil formation, or pedogenesis, is a complex process which reflects the local climate and rock mineralogy. All of the unconsolidated material that rests upon the bedrock is the associated regolith. Many different metals are concentrated at the surface, the most important being Al, Ni, Mn, Fe, Cu, Au, Pt and U. Laterites are associated with enrichments of Al, Ni, Au and platinum group elements, and are the principal environment for bauxite (Al) ore to form.

Regolith describes the weathered material above un-weathered bedrock and its formation depends on a number of factors:

- Climate
- Bedrock composition and structure
- Rate of weathering
- Rate of erosion
- Tectonic history
- And anthropogenic activity

Climate plays the greatest role in laterite formation due to the presence of rainfall and elevated temperatures. Laterites are a product of this downward percolation of rainwater and upward movement of moisture during dry spells, resulting in the development of a well-layered profile.

There are two primary subdivisions, the pedolith and the saprolith. The pedolith includes residual *in-situ* weathering where all the original bedrock textures are completely destroyed, and includes the soil, ferruginous zone, mottled zone and plasmic zone. The saprolith comprises bedrock that is highly weathered, but some primary minerals are preserved. This zone is subdivided into saprolite (more than 20 % primary materials altered) and saprock (rock which is partially weathered and less than 20 % of weathered material replaced). This is illustrated in Figure 2.16.

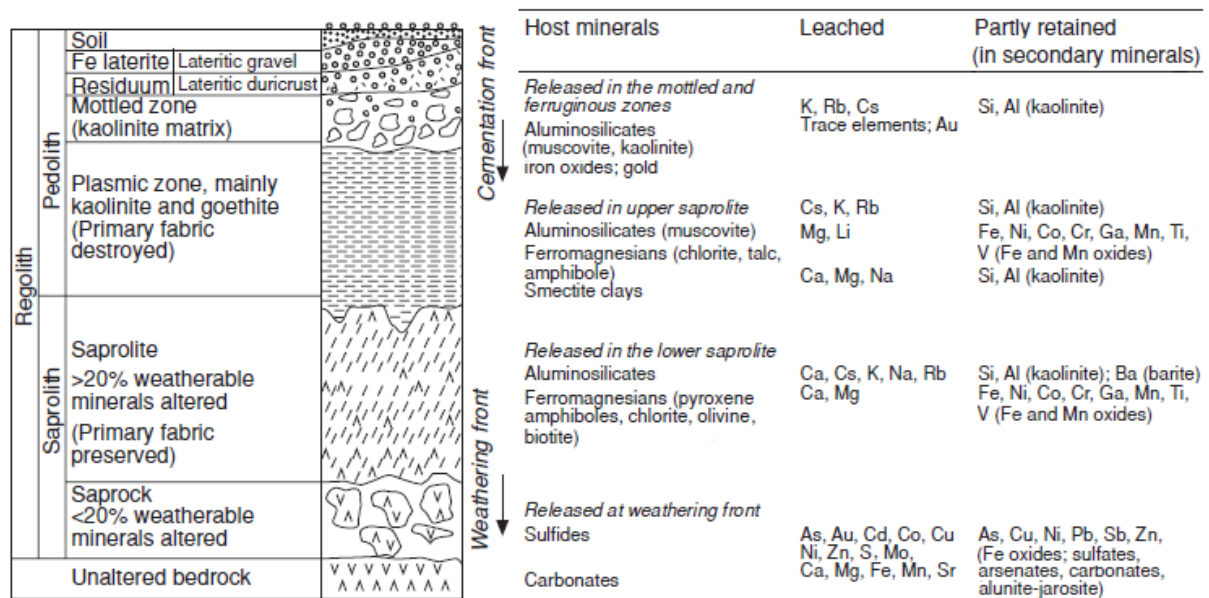


**Figure 2.16 Generalised lateritic regolith profile showing different horizons and a generalised pattern of element mobility within the regolith (adapted from Robb, 2005)**

As the weathering increases, contents of Ca, Mg, Na and K decrease, with the weathered material enriched in Al. The Chemical Index of Alteration (CIA), shown in equation 2.9, is used to indicate the degree of alteration, with more weathered material having a higher CIA value because the Na, K and Ca values decrease with weathering.

$$CIA = \frac{Al_2O_3}{Al_2O_3 + Na_2O + K_2O + CaO(in\ silicates)} \times 100 \quad (eq\ 2.9)$$

Boa and Zhou (2008) shows the weathering profile changes from hydro-mica and montmorillonite > halloysite (7 Å) and kaolinite > gibbsite (plus hematite). Churchman and Gilkes (1989) investigated a lateritic weathering profile and determined that there is a range of clay intermediates from halloysite to kaolinite. This is shown in Figure 2.17.

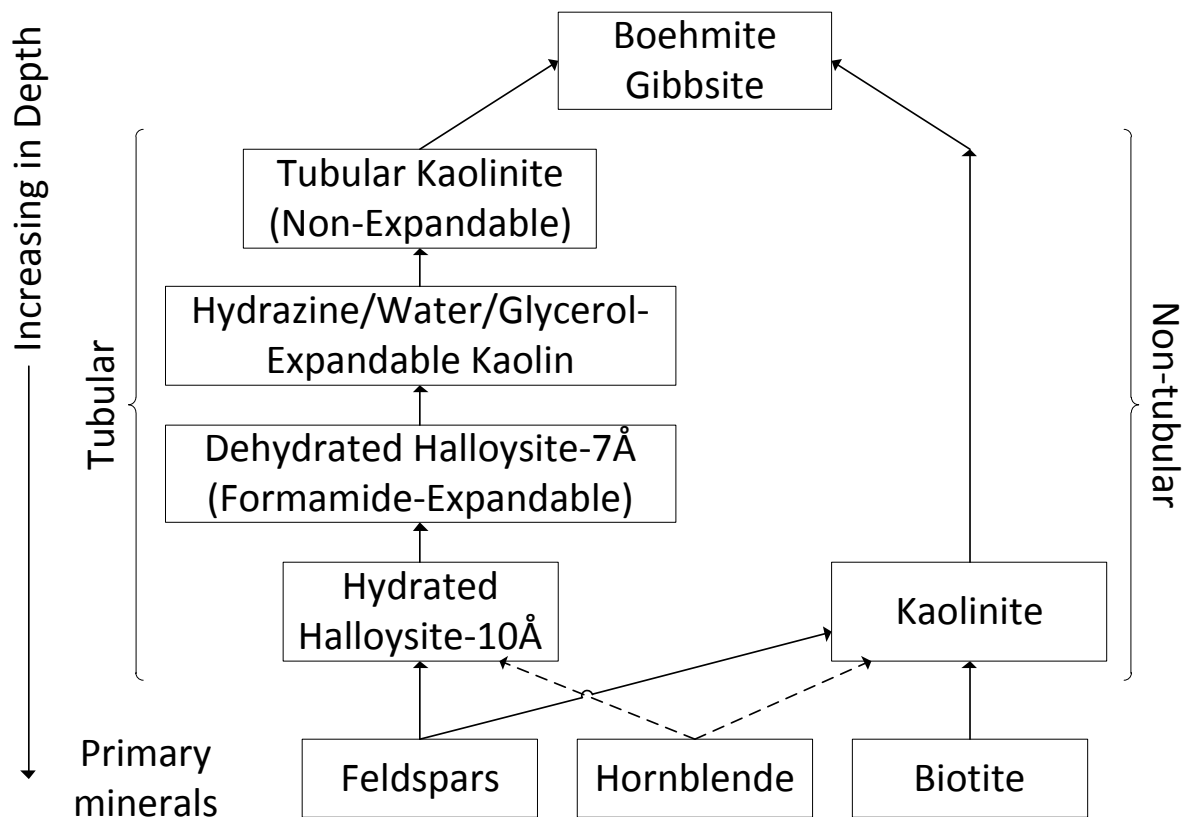


**Figure 2.17 Probable weathering paths in lateritic weathering of granite and dolerite involving kaolinite and halloysite (Western Australia) (adapted from Churchman and Gilkes, 1989)**

At the base of the weathered profile is the saprock and bedrock containing the primary silicate material, such as feldspars, hornblende and biotite. Above this is hydrated halloysite-10Å, which transforms into intermediates upwards through the weathered profile, with a decrease in the total kaolin (kaolinite and halloysite) mineral content towards the surface. This transformation is characterised by the ability or inability of the kaolin to react with certain organic compounds (Churchman and Theng, 1984). Kaolin can form interlayer complexes with a wide range of organic compounds, and hydrated halloysite can intercalate organic compounds such as amides with ease depending on the properties of the organic species. As the kaolin becomes dehydrated, complex formation is influenced by particle size, crystallinity and Fe content. The larger the particle, well crystallised and with low Fe content are conducive to complex formation.



The top of the profile is typically rich in Fe and Al oxides/oxyhydroxides such as boehmite (AlO(OH)). These minerals are created when Fe and Al ions are attracted to clay minerals and get deposited, a complex process which is simplified in Figure 2.18.

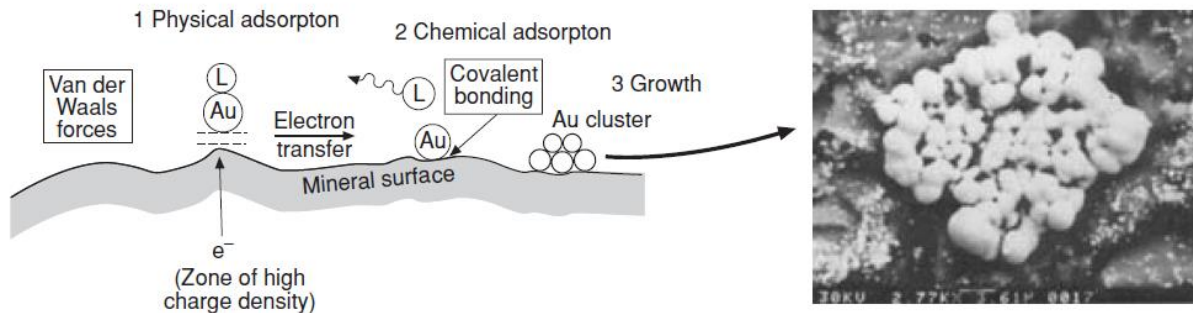


**Figure 2.18 Sequence of steps illustrating the steps involved in adsorbing metal ions onto a mineral surface (Robb, 2005)**

In this example, gold-ligand (Au-L) complexes are attracted to the mineral surface (in this case a negatively charged sulphide mineral, but clay minerals act in a similar way). This is the first stage of physical adsorption. The second stage involves chemical adsorption and covalent-like bonding, migrating along the surface to form clusters (as shown in the adjacent SEM image).

#### 2.2.10. REE enrichment

Many researchers have assumed that the REEs are relatively immobile but this assumption has been challenged by numerous authors, who have shown that chemical weathering causes REE mobilisation and fractionation (Williams-Jones *et al.* (2012); Bao and Zhao (2008)). REE have also been shown to be mobilised by hydrothermal fluids, concentrating them to economic levels such as the Bayan Obo REE in China (Migdisov *et al.*, 2016), dominantly of hydrothermal origin. The ability of REE to mobilise largely depends on REE complexes with ligands. It was shown by Migdisov *et al.* (2016) that the main transporting ligands are chloride (Cl<sup>-</sup>) and sulphate (SO<sub>4</sub><sup>2-</sup>), whereas fluoride (F<sup>-</sup>), carbonate (CO<sub>3</sub><sup>2-</sup>) and phosphate (PO<sub>4</sub><sup>3-</sup>) are more important as depositional ligands.

Balashov *et al.* (1964) showed that REE were mobilised during chemical weathering under warm and humid conditions. Möller and Giese (1997) conducted leaching experiments on silicate-dominant rocks (including granites) which showed that REE were fractionated during alteration and weathering. The fractionation was mainly controlled by accessory minerals.

Studies have shown that only a small portion of REEs exist in the rock forming minerals, and that most of the REE is incorporated in accessory minerals (Alderton *et al.* (1980); Sawka and Chappell (1988)). The behaviour of major REE-bearing accessory minerals under chemical weathering is the decisive factor in the accumulation and differentiation of REE in the weathered ore profile. REE-bearing accessory minerals are divided into three groups (Wu *et al.*, 1995):

1. Strongly resistant to weathering i.e. Xenotime and zircon
2. Moderately resistant to weathering i.e. Fergusonite, monazite and allanite
3. Weakly resistant to weathering i.e. Bastnaesite, parasite, gadolinite-(Y) and doverite

The proportion of REEs in ion-exchangeable form will therefore increase for accessory minerals which are more weakly resistant to chemical weathering. Kaolinite is one type of clay mineral that has been shown to remove REE cations from aqueous solutions (Aja, 1998).

Figure 2.19 summaries the numerous different pathways for REE migration.

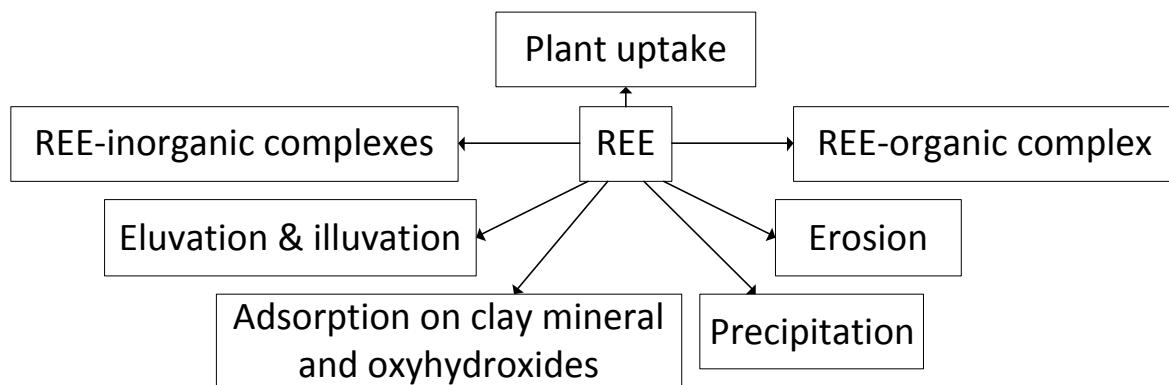


**Figure 2.19 Potential pathways for REE migration and sequestration (adapted from Aide and Aide (2012))**

Percolating water, containing CO<sub>2</sub>, allows for the leaching of REE-inorganic complexes as carbonates, and REE-organic complexation can result in either the mobilisation or immobilisation of the REEs. Eluviation (clays and solutes are removed) and illuviation (material accumulates) contribute to soil development with precipitation removing REEs from percolating water. Adsorption onto clay minerals and oxyhydroxides was suggested as the major cause of secondary enrichment of REEs in the weathering process (Bao and Zhou, 2008).

Duddy (1980) proposed that REEs accumulate in the deeper portions of soils developed from volcanic rocks which, along with the work of Nesbitt and Markovics (1997), indicate that REE leaching and surficial erosion combined to promote the continuous cycling of REE to deeper soil regions (Aide and Aide, 2012).

#### *2.2.11. Vegetation*

The behaviour of REE during weathering varies widely due to the location specific physiochemical and biological factors of rock weathering (Fritz, 1988). As Figure 2.19 suggests, REEs can be taken up by vegetation, usually accumulating in the roots and leaves. Much research in China (Pang *et al.*, 2002) has looked at the benefits of REEs to plant growth and have shown that crops treated with REEs result in productivity increases of between 5 to 15 % (Hu *et al.*, 2004). Increases in plant growth from applications of  $\text{CeCl}_3$  suggested they were enhanced by improved photosynthesis, as REEs can combine with pigments. These effects are related to improved chloroplast development and count rate, with many of the LREEs bound to the chlorophyll.

REEs play a role in the solum (uppermost “living” part of the soil) where humic substances can aid in the transport of REEs (Wood, 1996) and can play a role in the fractionation of these elements (Pourret *et al.*, 2007). This region is commonly different to the underlying saprolitic kaolin (Gilkes and Prakongkep, 2016), as weathering is most intense at the surface, resulting in kaolin that Churchman (2010) argues should be viewed more as secondary inorganic compounds of clay size, rather than kaolin of non-soil/geographical source. This is evidenced by its larger specific surface areas and higher cation exchange capacities compared to reference kaolins.

Soil kaolins common to tropical regions have the capacity to retain the water received from rainfall and release this water to plants in response to the demands of the growing plants. Singh (1991) showed that potassium and other plant nutrients are present in soil kaolin, which are partly available to plants. This is due to a stable and porous soil structure with an abundance of connected pores in the 0.1 to 10  $\mu\text{m}$  size range (Gilkes and Prakongkep, 2016). Kaolin-rich tropic soils, in particular oxisols, have a stable, low-density, porous “card house” structure where the kaolin plates are secured in place by iron oxide crystals attached to kaolin crystals through electrostatic attraction, as shown by Tawornpruek *et al.* (2006)

Plant roots are predominantly located in the top 30 cm of soil, with 95 % of global roots found in the top 2 m (Hasenmueller *et al.*, 2017). These biological factors aid in the soil generation, breaking down rocks to allow their minerals to be available for plants. This zone is particularly important since IAC deposits in China can be leached as close as 2 m from the surface.

### 2.3. *In-situ* Ion-adsorption Clays

#### 2.3.1. *In-situ* leaching

Percolation leaching is the process of selective removal of valuable metals from a mineral by introducing a solvent/leaching agent/lixiviant that seeps into and through an ore body that contains this mineral (Ghorbani *et al.*, 2016). This process can be grouped as follows (John, 2011):

- 1) *In-situ* leaching (also called in-place leaching or solution mining) (Underground)
- 2) Dump Leach (Run of Mine (uncrushed) ore)
- 3) Heap Leach (Crushed and/or agglomerated ore)
- 4) Vat Leach (usually crushed ore or concentrates)
- 5) Agglomerated Fines Heap Leach (crushed ore or concentrates)

As mentioned, ion-adsorption clays have a relatively low content of REEs. The use of percolation leaching has been vital in the treatment of low grade ores, as the process has the advantage of low capital and operating costs. The Chinese began leaching in the early 1970s using vat leaching in barrels with 1 M NaCl, followed by oxalic acid precipitation. This extremely low cost and fast processing method was set back by its small scale, low yield, high lixiviant concentration requirement and poor product quality. By the 1980s, batch leaching was conducted using a 0.3 M ammonium sulphate (NH<sub>4</sub>)<sub>2</sub>SO<sub>4</sub> solution, due to the improved desorption capabilities of NH<sub>4</sub><sup>+</sup> compared to Na<sup>+</sup>. This led to improved product purity (Moldoveanu and Papangelakis, 2016).

By the 1990s, heap leaching was implemented to replace dump leaching due to devastating mining-related deforestation and unregulated discharge of tailings. The traditional heap would consist of a 1.5 to 5 m high soil pile, built on a flat impermeable cofferdam with lixiviant injected into the top at a solid to liquid (S/L) ratio of 0.25 to 1. After washing at S/L ratio of 0.6 to 1, leach time can be from 100 to 320 hours and REE extraction can reach 90 % (Moldoveanu and Papangelakis, 2016).

China banned surface mining in 2011 (Wübbeke, 2013), in an effort to regulate the REE industry, and made *in-situ* leaching mandatory. This technology is more advantageous over surface mining in terms of vegetation and soil disturbance (Yang *et al.*, 2013). A typical *in-situ* leach profile is given in Figure 2.20, indicating the regolith layers.

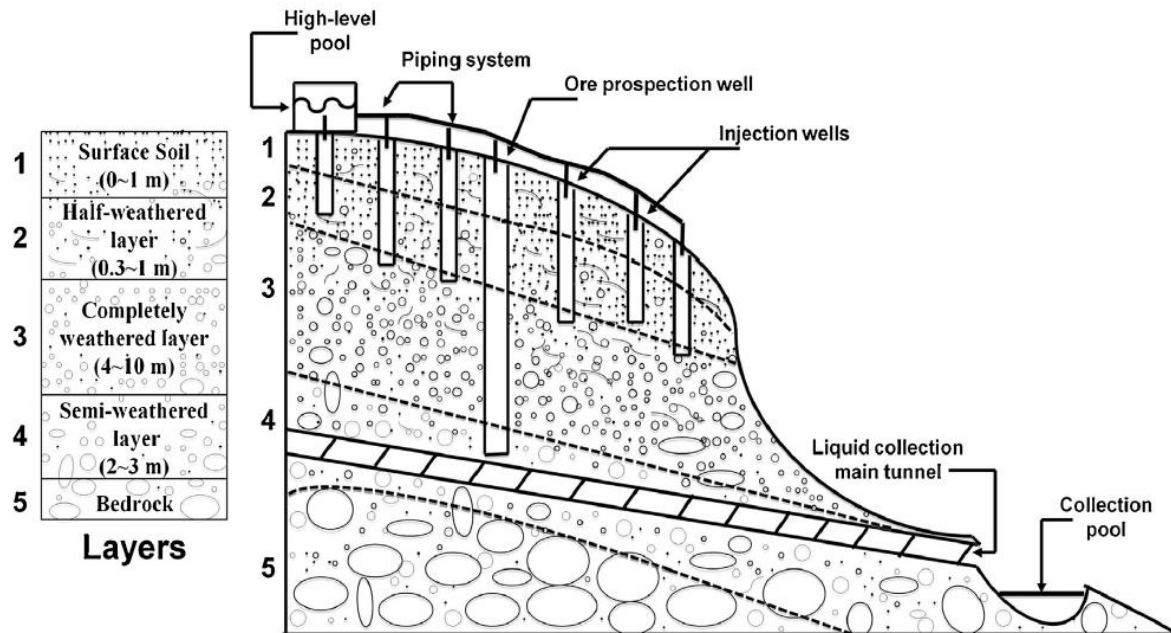


**Figure 2.20** Cross section view of a typical *in-situ* leach of an ion-adsorption clay (Vahidi, 2016)

Lixiviant (0.3 M  $(\text{NH}_4)_2\text{SO}_4$ ) is pumped at high pressure in holes of depth 1.5 – 3 m and diameter 0.8 m drilled 2 – 3 m apart. This fluid flows through the pores of the ore body and the loaded solution is pumped above ground or collected at the base of regolith. The whole process, including water injection for washing, can take up to 400 days (Moldoveanu and Papangelakis, 2016).

This process can only be implemented after comprehensive geological surveys are conducted, specific to the *in-situ* environment, determining the hydrogeological structure of the area. As layer 5 suggests in Figure 2.20, this procedure can only be applied to an orebody with suitable permeability in layers 1 to 4 and placed over a solid bedrock (5) without fissures. Otherwise underground water could be contaminated, losing lixiviant and REE recovery and leading to environmental disasters such as mine collapse and landslides (Moldoveanu and Papangelakis, 2016).

### 2.3.2. Properties of ion-adsorption clays

In kaolinite, the tetrahedral face has a permanent negative charge due to isomorphous substitution of  $\text{Si}^{4+}$  for  $\text{Al}^{3+}$ , whereas the octahedral face and edges are pH dependent (Tombácz and Szekeres, 2006). This is due to the reaction of the octahedral aluminium, giving a positive charge in acidic pH (equation 2.10) and negative charge in alkaline pH (equation 2.11).



The main advantage of ion-adsorption clay deposits is the relative ease of extraction. This is because at  $\text{pH} < 6.5 - 6.8$ , 60 – 90 % of the surface adsorbed extractable REEs occur as simple or hydrated cations held by physisorption at negative sites of the kaolin. For  $\text{pH} > 7$  the REEs become irreversibly-fixed as hydrolysed Clay-O- $\text{REE}^{2+}$  species, derived from chemisorption with amphoteric surface hydroxyl groups (Piasecki and Sverjensky, 2008).

There are three main forms of REE present in ion-adsorption clays, which is illustrated along with proposed mechanisms in Figure 2.21.

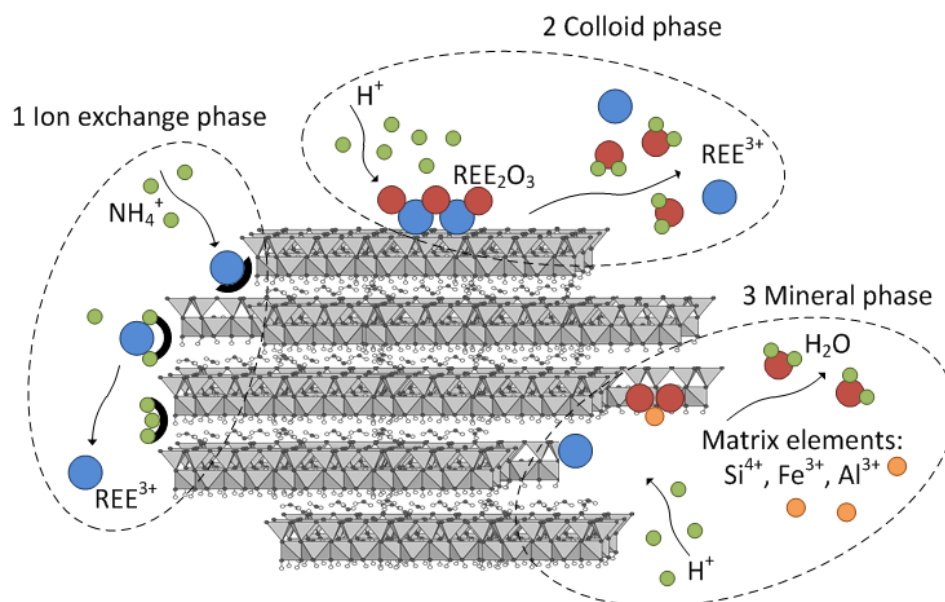
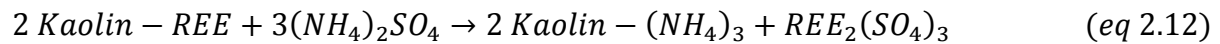
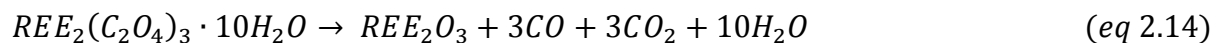
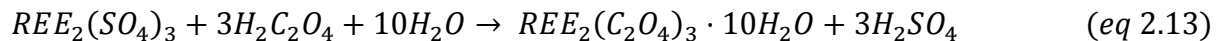


**Figure 2.21 Proposed leaching mechanisms on platy hydrated halloysite-10Å: 1. Ion exchange phase. 2. Colloid phase. 3. Mineral phase (adapted from Joussein (2005) and Voßenhaul *et al.* (2015))**

Phase 1 can be recovered by simple ion-exchange of a monovalent cation (such as  $\text{NH}_4^+$ ), following a theoretical 3:1 stoichiometry, and transferring into solution as a soluble sulphate ( $\text{SO}_4^{2-}$ ) or chloride ( $\text{Cl}^-$ ) as shown in equation 2.12.



As Figure 2.5 shows, these dissolved REEs are selectively precipitated with oxalic acid to form oxalates, which are subsequently roasted at 900 °C, as shown in equations 2.13 and 2.14.



The actual amount of lixiviant needed usually exceeds the stoichiometric amount due to competing desorption of other cations such as Al, Na, K, Mg, Ca, Mn, Zn and Fe which, in portion, are also adsorbed physically on the clay surface.

The second phase is the colloid phase where REE are deposited as insoluble oxide, hydroxides or colloidal polymeric organometallic compounds. These require more aggressive acidic conditions to leach. The organic matter can be leached with 0.1 M sodium pyrophosphate ( $\text{Na}_4\text{P}_2\text{O}_7$ ) (Sanematsu and Kon, 2013). The final phase is REE integrated in the crystal lattice, requiring the decomposition of the phyllosilicate mineral phase to recover.

One of the characteristics of the majority of IAC is the poor recovery of Ce by ion-exchange. This is due to the oxidised  $\text{Ce}^{4+}$  ion precipitating as cerianite  $\text{CeO}_2$ , leading to a relative depletion of this REE as ion-exchangeable. This process can be enhanced by manganese minerals in the same deposit, as it has been shown that  $\text{Ce}^{3+}$  can be oxidised during adsorption on Mn oxides (Ohta and Kawabe, 2001). It has also been shown that kaolinite in the presence of Mn was synthesised at lower temperatures, indicating that it might also play a positive role in the crystallisation of kaolinite (Zhang *et al.*, 2010).

### 2.3.3. Current work

The major research on REE extraction, especially of IAC deposits, has been conducted in China. Outside China, recent geological surveys have shown that the sub-tropical regions of Brazil and Madagascar show similarities with the Chinese ore (Rocha *et al.* (2013); Moldoveanu and Papangelakis (2016)). Work in China (Yang and Zhang, 2015) and in Canada

at the University of Toronto (Moldoveanu and Papangelakis, 2012) conducted batch leach and column experiments to determine the optimum conditions for REE extraction.

The current trend in IAC research focusses on the ammonia pollution caused by ammonium sulphate. Research has therefore looked at adding leaching enhancing additives to the conventional  $(\text{NH}_4)_2\text{SO}_4$  lixiviant or using alternative lixiviants to varying proportions. Seawater is also a convenient source of water in coastal regions. The second main trend is the reduction of impurities in the leached solution such as Al, Fe, and Mn.

This research is conducted in batch reactors or with column leaching, with some authors using chromatographic plate theory (Tian *et al.*, 2013a). Moldoveanu and Papangelakis (2012) found that batch reactions can be completed in as little as 5 min.

Many researchers in China have applied the shrinking core model to the leaching of WCDREO, and have showed that the rate is controlled by diffusion of leaching agent into the solid particle (Yanfei *et al.* (2015a); Zhang and Edwards (2013); Zhengyan *et al.* (2016)). Because REEs are mostly adsorbed onto the kaolinite broken bonds, the inner diffusion is likely through some agglomerated portion of the mineral, rather than inner diffusion through the clay layers. Therefore, to enhance the leaching of REEs, the hydrophilicity and permeability of the lixiviant must be improved.

The ability of REEs to form complexes with organic reagents has been used to enhance the ammonium sulphate leaching (Peelman *et al.*, 2015). Carboxymethyl sesbania gum is added (0.03 – 0.1 %) to aid in the hydrophilicity of lixiviants, due to the abundance of hydroxide radicals (Tian *et al.*, 2013b). Fulvic acid (Luo *et al.*, 2015) and humic acid (Pourret, 2007) have also been used, improving total REE extraction by up to 8 %. Other uses of organic compounds include adsorption of REE by blue-green algae (Kim *et al.*, 2011) and bacteria (Takahashi *et al.* (2005); Bonificio and Clarke (2016); Ozaki *et al.* (2006)).

The two main anion systems investigated are sulphate ( $(\text{NH}_4)_2\text{SO}_4$ ) and chloride systems (NaCl), but authors in China have shown that the exchangeability and permeability of  $\text{NH}_4\text{Cl}$  and  $\text{NH}_4\text{NO}_3$  both surpass that of ammonium sulphate (Zhengyan *et al.*, 2016). They had determined that conditions were optimal at 1:1  $\text{NH}_4\text{Cl}$  to  $\text{NH}_4\text{NO}_3$  ratio, at 0.2 mol/L ammonium concentration at pH 4 – 8. Voßenhaul *et al.* (2015) also investigated sulphate,



chloride and nitrate systems, but they introduced much more acidic conditions which would improve REE recovery but at the cost of increased impurities recovered to the leachate.

Moldoveanu and Papangelakis (2012) investigated the desorption abilities of a select group of cations in two anion systems. They found that the leaching efficiency decreased in the order of  $Cs^+ > NH_4^+ > Na^+ > Li^+$  and that sulphates are approximately 10 % better than chlorides. This trend was explained in terms of their hydration enthalpy, with the more hydrated cations (greater  $-\Delta H_{hyd}$ ) favouring the solution phase over the dehydrated surface-adsorbed ion (Teppen and Miller, 2006). Teppen and Miller (2006) had determined this relationship in swelling clays, which as described in previous sections, has fundamentally different cation interactions compared with the non-swelling kaolin group. This trend therefore could be a result of un-characterised smectite or montmorillonite minerals in the sample, or because hydrated halloysite is mimicking this smectite process. Additionally, it is possible that the REEs don't fully dehydrate and may be partially hydrated on the clay surface. The effect has also been limited to monovalent cations.

During *in-situ* leaching, ions such as Mg and Ca are leached out as impurities, which leads to a loss in soil nutrients. To combat ammonium-nitrogen pollution and correct this nutrient deficiency, leaching effects were investigated using Mg and Ca in sulphate and chloride systems (Yanfei *et al.* (2015b); Yanfei *et al.* (2016)). Results from this show that the leaching efficiency decreases in the order  $(NH_4)_2SO_4 > NH_4Cl > MgSO_4 > CaCl_2 \approx MgCl_2$ . It was found that the best Mg –  $NH_4$  – Ca ratio was 15:25:60, giving a REE recovery above 94 %. However the use of  $MgSO_4$  has the drawback of reduced REE extraction (between 5 – 7 %) compared to ammonium sulphate, but the advantage is long term environmental considerations and a 10 – 15 % reduction in aluminium desorption to only 49.2 %.

Aluminium is the main impurity in the leachate, and the demands on REO purity requires  $RE_2O_3 / Al_2O_3$  above 600 and Al content in the RE product < 0.3 %. The ion-exchangeable Al can be hydrolysed and precipitated as  $Al(OH)_3$  (equation 2.15), allowing it to remain in the ore body (Wang, 1995).



Therefore the main factor in controlling the Al levels is pH (Yang and Zhang, 2015). Optimum pH values were determined by Moldoveanu and Papangelakis (2012) to be between 3 (any

lower causes breakdown of Al in the silicates) and 6 (REEs become hydrolysed at pH 6.8). The hydrolysis of Al can occur at pH 5 and produce H<sup>+</sup>, and to keep the pH from dropping the solution can be buffered with the use of ammonium acetate (equation 2.16).



The optimal conditions for REE extraction above 80 % were 2 % compound lixiviant of ammonium nitrate to sulphate molar ratio 4:1 and a 0.05 % ammonium acetate inhibitor (Yang and Zhang, 2015).

## 2.4. Research Approach

The literature presented highlights the key characteristics associated with rare earth elements, kaolinite and halloysite-7Å, clay and regolith formation, in-situ leaching and current work in REE recovery. The REEs are described mainly by the fraction of LREEs from HREEs with some Chinese deposits showing HREE enrichment. Soil kaolins show highly defective crystal structures relating to the *in-situ* environment formation and sample mineralogy. This highly defect structure increases the surface area and broken bonds allowing for the enrichment of LREEs and HREEs by adsorption. Soil kaolin contains varying amounts of kaolinite and halloysite which can show a variety of hydration states. Halloysite has a slightly greater cation-exchange capacity than kaolinite and can show a range of morphologies. Kaolinite is formed from the weathering of granites and usually contains impurities relating to the sample texture. These impurities also have cations liberated on the clay surface which are leached with the REEs consuming lixiviant and needing removal. In-situ leaching currently incorporates ammonium sulphate but other lixiviants are investigated such as sodium chloride, magnesium sulphate and ammonium nitrate. Impurities such as Al are pH dependant and can be inhibited by use of a buffer such as ammonium acetate in ammonium sulphate leaching.

Based on the literature review presented in this chapter, the following characterisation suite was formulated:

- Particle Size Distribution (PSD) to investigate the distribution of fine grain kaolin and coarser impurity content in the samples.
- X-ray Fluorescence (XRF) to determine the bulk chemical composition of the sample and degree of alteration.

- X-ray Diffraction (XRD) to determine the clay crystal structure including quantification by Rietveld Analysis and halloysite content.
- Quantitative Evaluation of Minerals by Scanning Electron Microscopy (QEMSCAN) to determine the clay sample texture and identify key mineral phases.
- Inductively Coupled Plasma-Mass Spectrometry (ICP-MS) to determine the REE content including variation between key phases.
- Scanning Electron Microscopy (SEM) to determine clay morphology.
- Transmission Electron Microscopy (TEM), including elemental mapping, to determine the effects of iron incorporation into the clay mineral structure.

The following leaching experiments were also formulated:

- Step-wise leaching to determine the REE associated with kaolinite, halloysite, organic matter and mineral phases. Step one involves the targeting of kaolinite with sodium chloride, step two targets halloysite with sodium acetate, step three targets organic matter with tetra-sodium pyrophosphate and the fourth step targets the mineral phase with Aqua Regia.
- Step-wise leaching replacing sodium chloride with ammonium chloride and magnesium chloride and sodium acetate with ammonium acetate and potassium acetate (alternative to magnesium acetate). This is to compare the ion-exchange characteristics for  $\text{Na}^+$ ,  $\text{NH}_4^+$  and  $\text{Mg}^{2+}$  ions.
- Simulated seawater leaching, as the mine has easy access to seawater, with increasing amounts of ammonium sulphate added to increase the REE extraction.
- Compound leaching with ammonium sulphate and magnesium sulphate to investigate the effect of the magnesium ion on REE extraction which when incorporated will solve a well-known magnesium deficiency in soils after leaching.
- Compound leaching with ammonium sulphate and ammonium nitrate to investigate the effect of the nitrate ion on REE extraction due to improved permeability effects.
- To investigate the effects of buffer addition to inhibit the leaching of Al by increasing the concentration of ammonium acetate in an ammonium sulphate leach.

### 3. EXPERIMENTAL METHODOLOGY

This chapter is divided into 3 sections. The first section presents the materials under investigation, including regional geology and sample preparation. The second section presents the suite of characterisation techniques used to fulfil characterisation objectives. The final section presents the batch leach reactor setup and leaching program.

#### 3.1. Materials

##### 3.1.1. Regional geology

The island of Madagascar is well known for its unique climate and wildlife. In recent geological history (late Cenozoic era), rifting caused by tectonic activity has produced accompanying igneous activity and volcanism. The igneous rocks form part of what is called the Ampasindava alkali-bearing province, which occupies the peninsula to the north of the country (Figure 3.1).

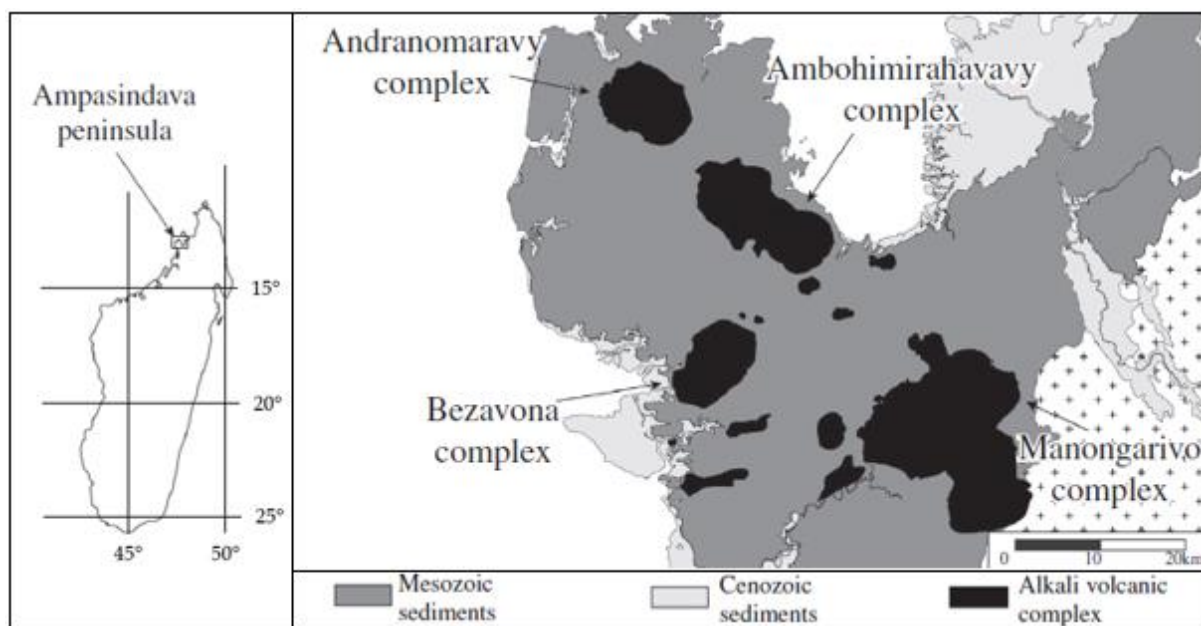


**Figure 3.1 Geological map of Madagascar, with locality shown to the left, showing the location of the complexes in the Ampasindava peninsula (Estrade *et al.*, 2014)**

There exists a NW-SE alignment of three alkaline complexes, named the Andranomaravy, Ambohimirahavavy and Manongarivo, which intrude Mesozoic sediments deposited mainly in a marine environment. The rocks range from ultramafic (rich in Mg and Fe) to acidic.

The REE mining company, Tantalus has their entire site situated in the Ambohimirahavavy igneous complex, a Cenozoic annular complex approximately 18 km across. It encompasses

an area of approximately 150 km<sup>2</sup>. It consists of two intrusive bodies, predominantly syenites, the Tsarabariabe intrusion to the NW and the Ampasibitika intrusion to the SE (Figure 3.2)

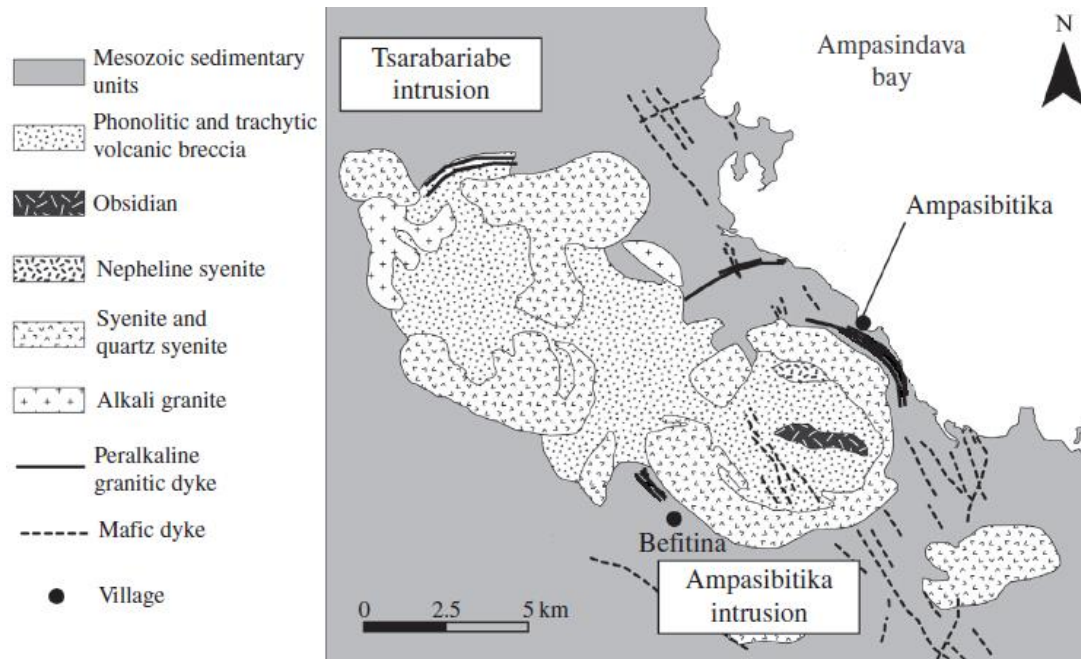


**Figure 3.2 Geological map showing Tsarabariabe and Ampasibitika intrusions (Estrade *et al.*, 2014)**

The igneous rocks of interest occur as massifs and include alkali syenite, alkali granite, rhyolite and volcanic breccia. Peralkaline granitic dykes flank the Ampasibitika intrusion to the north and, to a lesser extent, in the south. These intrusions are characterised by central depressions known as calderas and include volcanic rocks of trachyte composition. The rim of the caldera has a higher terrain comprised of syenite resistant to weathering.

The granite is more susceptible to weathering and forms the low terrain with the exception of a small central rhyolite at the centre of the intrusion, forming a cone of high terrain. The granite is locally termed fasibitikite. Research shows that this ore could potentially supply REEs (Ganzeev and Grechishchev, 2003).

The primary magmatic assemblage for this region is composed of alkali feldspar ((K,Na)AlSi<sub>3</sub>O<sub>8</sub>), aegirine (clinopyroxene - NaFeSi<sub>2</sub>O<sub>6</sub>), arfvedsonite (a type of sodium amphibole - [Na][Na<sub>2</sub>][(Fe<sup>2+</sup>)<sub>4</sub>Fe<sup>3+</sup>][(OH)<sub>2</sub>Si<sub>8</sub>O<sub>22</sub>]) and quartz (SiO<sub>2</sub>). The accessory minerals responsible for REE enrichment include chevkinite ((Ce,La,Ca,Th)<sub>4</sub>(Fe<sup>2+</sup>,Mg)<sub>2</sub>(Ti,Fe<sup>3+</sup>)<sub>3</sub>Si<sub>4</sub>O<sub>22</sub>), eudialyte (Na<sub>15</sub>Ca<sub>6</sub>(Fe,Mn)<sub>3</sub>Zr<sub>3</sub>SiO(O,OH,H<sub>2</sub>O)<sub>3</sub>(Si<sub>3</sub>O<sub>9</sub>)<sub>2</sub>(Si<sub>9</sub>O<sub>27</sub>)<sub>2</sub>(OH,Cl)<sub>2</sub>), monazite ((Ce,La,Nd,Th)PO<sub>4</sub>), pyrochlore ((Na,Ca)<sub>2</sub>Nb<sub>2</sub>O<sub>6</sub>(OH,F)) and zircon (ZrSiO<sub>4</sub>).

### 3.1.2. Sample preparation

The climate in Madagascar is divided into two seasons, a dry season from April to October, and a wet season from November to March. The accessibility of the mine is limited during the wet season, so the sampling was conducted in the dry season. Samples provided for this project were sampled from a regolith with a vertical pit, 1 m x 1 m with a depth of 10 m. Figure 3.3 shows the vertical pit, sampling procedure and samples A1, A2, B and F received. Sample A1 (5 – 6.5 m) was obtained in the pedolith layer above the saprolite samples A2, B and F (6.5 – 10 m).



**Figure 3.3 Pit excavation showing pit sampling procedure, manual techniques and samples received (A1 (5 – 6.5 m), A2, B and F (all 6.5 – 10 m)) (Desharnais *et al.*, 2014)**

The provided samples (5 kg each) were de-bagged and approximately 500 g of each sample kept as '*in-situ*' material. The remaining material was sub-sampled to provide suitable portions for QEMSCAN, which were dried and mounted. A negligible amount of discrete clay material based on colour was separated by hand using tweezers for XRF and ICP-MS characterisation. The bulk of the remaining material was then dried overnight in an oven at 60 °C (Moldoveanu and Papangelakis, 2012) to drive off water without affecting the clay mineral structure. The dried clay material was then hand crushed and mixed to form a homogenous powder using a metal rolling pin. The final powder was then split using a rotary splitter to create representative samples for the experiments.

### 3.1.3. Reagents

All reagents used to make the lixiviants are of Analytical Reagent standard and sourced from Monitoring and Control Laboratories (Pty) Ltd and Merick (Pty) Ltd. A list of chemicals used can be found in the Appendix 6.2.1 Table 6.2. The lixiviants were prepared from known masses of reagents in distilled water.

## 3.2.Characterisation Techniques

### 3.2.1. PSD (Particle Size Distribution)

Dried and crushed clay material was added to a stack of sieves of varying passing sizes and vibrated on a Screen Shaker (Retsch AS 200). The screens used were Retsch, Endocotts and Kingtest sieves, the largest sieve was 150  $\mu\text{m}$  then decreasing in size from 150 to 106, 75, 53, and the smallest 38  $\mu\text{m}$ . Retsch rubber balls (20 mm) were added to each stage to aid separation. The smallest particles, passing the 38 micron sieve, were analysed on a Malvern Instruments Mastersizer 2000 (version 5.60). The sample was dispersed in water at 750 rpm with a pump of 1 250 rpm and 5 % Sodium hexametaphosphate (5 mL) to act as a dispersant.

### 3.2.2. XRF (X-ray Fluorescence)

The equipment used was a Panalytical Axios wavelength-dispersive XRF spectrometer with rhodium end-window X-ray tube. Approximately 10 g of homogenised, dried and split clay material of particle size < 38  $\mu\text{m}$  was used for XRF measurements to determine the major and minor chemical elements oxides. The sample was then milled in a carbon steel ring and disk mill to a maximum particle size of approximately 20  $\mu\text{m}$ . From this milled sample, 2 g was weighed into a ceramic crucible of known mass, and placed in an oven at 110 °C for a period of 8 to 16 hours. This drives all the adsorbed water out of the sample. The weight loss from the combined sample and crucible mass was calculated as weight percent "H<sub>2</sub>O-".

The crucible with sample was then placed into a muffle furnace and heated to 800 °C for a period of 4 hours, cooled and weighted again. The weight difference was calculated as a percentage and designated as "loss on ignition (LOI)". This represents the weight percentage lost due to the loss of any structural volatiles (e.g., H<sub>2</sub>O, CO<sub>2</sub>) as well as the weight gain due to oxidation of FeO to Fe<sub>2</sub>O<sub>3</sub>.

The major elements were measured by preparation of fused disks. Approximately 0.7 g of the dried, ignited sample powder was mixed with 6 g of a flux composed of lithium metaborate (LiBO<sub>2</sub>) and lithium tetraborate (Li<sub>2</sub>B<sub>4</sub>O<sub>7</sub>). This flux lowers the melting temperature of the sample, allowing it to be melted over a gas burner. An automated fluxer was used to mix and homogenise the sample-flux mixture in a platinum crucible, and the molten mixture was poured into a heated platinum mould, which cools slowly into a fusion disk. The advantage of this method is that the minerals in the sample are entirely melted into an amorphous glass,

so any matrix effects due to sample mineralogy are eliminated (which increases precision). The fusion disks were calibrated against a series of well-characterised rock standards that have also been prepared as fusion disks (Norrish and Hutton, 1969).

The minor and trace elements were measured using pressed pellets. Approximately 6 g of un-ignited sample powder was thoroughly mixed with a drop of polyvinyl alcohol (as binder) and compacted into a cylindrical disk shape with a steel die using a 10 ton hydraulic press. The advantage of the pressed pellet sample preparation method is that the sample powders are not diluted, and thus they yield maximum sensitivity. However, the presence of contrasting mineralogies between samples means that matrix effects are greater, resulting in some additional uncertainty.

Major oxide and trace element concentrations were determined by comparing measured, corrected characteristic X-ray intensities of unknowns to calibration curves obtained from the measurement of up to 40 well-characterised, natural standards prepared identically to the samples. The calibration curves were generated by plotting elemental or oxide concentration (in ppm or weight percent) versus characteristic X-ray intensities for each element. The X-ray intensities represent peak minus background intensities and were corrected for matrix effects such as absorption and enhancement of analysed X-rays, and, where necessary, are also corrected for spectral peak overlap.

### *3.2.3. XRD (X-ray Diffraction)*

Powder X-ray diffraction is a well-established method for determining the crystalline structure of minerals. This technique uses the emission of X-rays (typical source of X-rays is Cu K $\alpha$  (1.54 Å)) targeted at the mineral containing a regular array of atoms, which scatter the X-rays, forming constructive interference in a few specific directions. These specific directions appear as spots on the diffraction pattern, which is used to identify the crystal structure of the mineral. The characteristic diffraction pattern can be compared to standard reference patterns in crystallographic databases (such as the Powder Diffraction File (PDF) database issued by the Int. Centre for Diffraction Data) (De Villiers, 2016).

XRD analysis of 4 clay samples was performed to determine whole rock mineralogy focussing on clay species characterisation. The material was dried and split; sub-samples were milled and homogenised to a fine powder at approximately 20  $\mu\text{m}$  in size. The clay fraction was



extracted from ~ 5 g crushed remainder of each sample and oriented slides were prepared in duplicates.

X-ray diffraction (XRD) measurements were performed on random whole rock powder preparations and orientated clay fraction preparations. Random powder diffraction on micronised material was carried out to determine the bulk mineralogy of the samples. Diffraction data from oriented measurements at air-dried state and after various treatments were used to characterise the clay species. Clay minerals were identified by diffraction peak locations of their basal (00l) reflections at air-dried (AD) state. X-ray data were recorded on a Bruker D8 Advance diffractometer with 2.2 kW Cu K $\alpha$  radiation ( $\lambda = 1.54060 \text{ \AA}$ ), LynxEye detector with active area of 230.4 mm<sup>2</sup> and Ni filter. Rietveld refinement and quantification was done with Bruker diffraction Topas V4.2 software.

#### 3.2.4. *Halloysite differentiation*

Halloysite differentiation can be problematic if the sample is dehydrated, as halloysite-7 $\text{\AA}$  has the same chemical structure as kaolinite. The formamide intercalation test is widely used for this differentiation (Joussein *et al.*, 2007).

Halloysite has a capacity for interlayer adsorption with formamide, a polar molecule with a dipole moment of 3.71 Debye, irrespective of sample crystallinity, morphology and iron content (Churchman and Theng, 1984). There is no significant intercalation in kaolinite in 4 hours of contact. If the sample is sprayed with formamide and X-rayed after 1 hour, halloysite will give a basal peak at 10.3-10.4  $\text{\AA}$ . Kaolinite does not expand beyond 7.2  $\text{\AA}$ .

Intercalation methods have the advantage over other techniques in that they apply to the whole sample, negating the need for fractionation and pre-treatment (Theng *et al.*, 1984). Two widely used techniques involve sequential treatment with potassium acetate and then water (Wada, 1961), or hydrazine and then water and glycerol. In both methods, treatment with water or water and glycerol causes the initially expanded kaolinite to collapse to its original basal spacing of 7  $\text{\AA}$ . Hydrazine suffers from the disadvantage of being highly toxic and flammable, therefore will not be used in this study.

### 3.2.5. QEMSCAN (*Quantitative Evaluation of Minerals by Scanning Electron Microscopy*)

QEMSCAN (Quantitative Evaluation of Minerals by Scanning Electron Microscopy) is a top of the range automated mineral analyser. Its key advantage is its ability to rapidly collect quantitative data for many thousands of particle sections with minimal operator intervention. This method has been successfully used on Ni laterites (Andersen *et al.*, 2009).

The machine used was a 650 F QEMSCAN using a field emission gun-scanning electron microscope (FEG-SEM) from FEI combined with high resolution BSE (Backscattered Electron), Bruker XFlash 6130 (25 kV, 5 nA beam current) Energy Dispersive Spectrometers (EDS) and a Spectral Analysis Engine (SAE) to analyse phases.

Samples were prepared by first selecting small sections of clay, cutting it to fit a 30 mm circle, leaving an unaltered, relatively smooth and even surface for drying. The cut sections were dried at 60 °C to leave a ceramic type surface ready for mounting and polishing. The sample was mounted in resin and allowed to cure (30 mm round mould). The cured mount was carefully dry hand polished (more control than machine polish) with diamond sandpaper of different roughness, from coarse to fine, taking care to expose the clay from the resin without forming depressions and bubbles.

The polished block was carbon coated in a Quorum Q150T E coater before mounting in the machine. The beam current was first optimised at 10 nA on the Faraday Cup, with chamber vacuum  $< 1 \times 10^{-4}$  atm. Back-scattered Electron Detector (BSE values) calibration are related to each other at a working distance of  $Z = 13.0$  mm, using Gold Standard at BSE 232, Quartz Standard at BSE 42, Copper Standard at BSE 130. To develop the SIP (Species Identification Protocol) file, single fields were run at a field size of 100 microns, with a step size of 5 microns, of known pure mineral sections. Field images were also run with field size of 1 500 microns, step size of 10 microns.

### 3.2.6. SIP (*Species Identification Protocol*) list development

The SIP list is the cornerstone of the QEMSCAN analysis; it is the list by which elemental information from the Bruker EDS detectors is converted to identify minerals present. These lists are developed over many years and analysing many mineral blocks. A new list had to be built since no existing files were suitable for this type of sample. The procedure is outlined in

the Appendix 6.2.2. Multiple techniques were used to validate these data such as Quantitative XRD and back calculation from XRF.

### *3.2.7. ICP-MS (Inductively Coupled Plasma-Mass Spectrometry)*

Rare Earth Elements are difficult to analyse in the environment due to their low concentration. Many techniques have been developed to analyse these elements, the most powerful being Inductively Coupled Plasma-Mass Spectrometry (ICP-MS). The instrument used is a Thermo-Fisher X-series II quadrupole ICP-MS system. Samples are added, and the plasma ionises the elements in the samples and generates a range of charged species which move through the ion lens and are focussed in the mass spectrometer. This separates the ions by their mass-to-charge ratio and measured by the detector. The signal intensities are measured and converted into elemental concentrations proportional to the amount of species present. These are calibrated against multi-element synthetic certified standard solutions. Precision and accuracy are determined against digested USGS rock standards.

### *3.2.8. Clay digestion*

There is evidence that certain clays are incompletely digested with standard methods of digestion (Wilson *et al.*, 1997), so hydrofluoric acid is used for its ability to dissolve silicate minerals efficiently. After the clay samples have been dried and split, 50 mg of material is weighed and added to 5 mL of HF with 1 mL Aqua Regia, for 5 hours on a hotplate at 110 °C to dissolve the sample. The solution is then sent for ICP-MS analysis.

### *3.2.9. SEM (Scanning Electron Microscopy)*

To provide detailed images at high resolution which show distinct morphology of the clay, the structure was examined under Field Emission Gun (FEG) high resolution Nova NanoSEM. The machine was equipped with an In-lens SE and In-lens BSE detectors with analysis using Oxford EDS systems. Samples were prepared from the finest size fraction (< 38 micron); a small sample was added to a stub with glue and allowed to dry. Care was taken that there is sufficient clay on the stub. Excess clay was removed with a dust spray, and the stub was carbon coated in a Quorum Q150T E coater to disperse the electron charge.

### *3.2.10. TEM (Transmission Electron Microscopy)*

Transmission electron microscopes are capable of capturing fine detail such as a single column of atoms owing to the smaller de Broglie wavelength of electrons and was used to determine the effects of iron incorporated in the clay mineral structure and provide elemental mapping.

Samples were characterised using a Thermo Fischer Scientific / FEI Tecnai F20 equipped with a FEG and operated at 200 kV at the University of Cape Town (UCT). Samples were dispersed in ethanol and deposited on Quantifoil® carbon films supported on copper TEM grids.

Scanning Transmission Electron Microscopy – Bright Field (STEM-BF) and High-Angle Annular Dark Field (HAADF) transmission electron microscopy images were recorded using a JEOL JEM-ARM200F double Cs-corrected TEM equipped with a FEG, a STEM unit and an HAADF detector, operated at 200 kV at the Nelson Mandela Metropolitan University (NMMU).

Samples were dispersed in ethanol and deposited on Quantifoil® carbon films supported on copper TEM grids. To reduce carbon contamination during the TEM imaging, they were subjected to mild plasma cleaning (25 W in 20 sccm air flow for 45 s) using a Gatan Solarus model 950 plasma cleaner. EDX mapping was performed using an Oxford Instruments XMaxN100TLE detector and the Aztec software package.

## 3.3. Batch leach tests

### *3.3.1. Batch-stirred tank reactors*

Ion exchange of the lixiviant with the REEs adsorbed on the clay micro-structure is best facilitated if the lixiviant has easy access to the clay surface. This is done with a batch-stirred tank reactor, with 150 mL 0.5 M lixiviant in a 500 mL glass flask with magnetic stirrer. The temperature is kept constant at 25 °C with the use of a water bath. To keep the solid:liquid ratio 1:2, 75 g of dried, sub-sampled clay is added to the reactor. The experimental setup is shown in Figure 3.4.

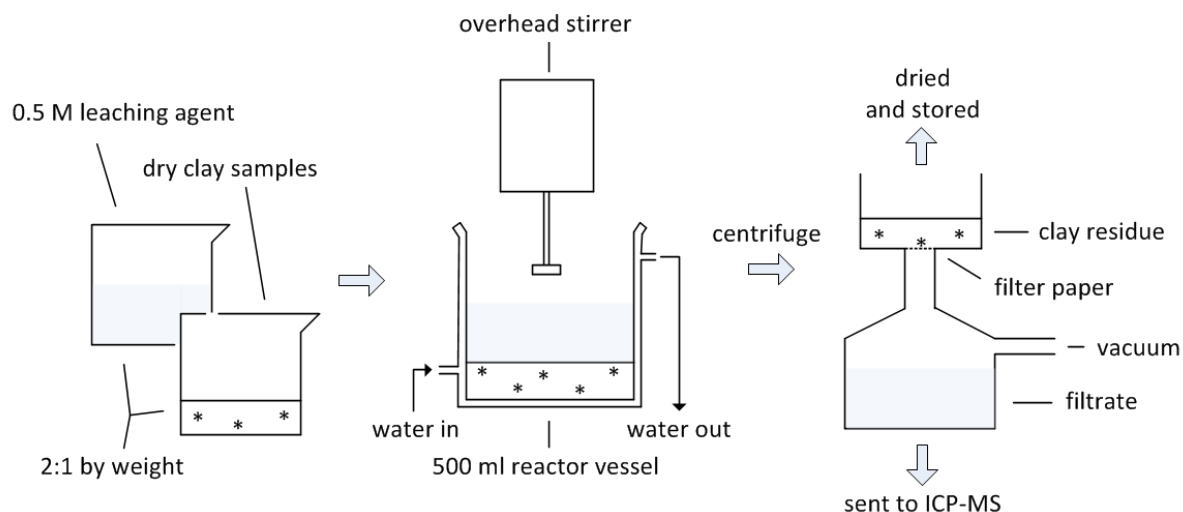


**Figure 3.4 Batch-stirred reactor experimental setup**

The reaction is allowed to proceed for 15 minutes. Previous experiments conducted using this setup have shown that the reaction proceeds to completion within this time, and that extended stirring time might lead to loss of REE due to hydrolysis (Moldoveanu and Papangelakis, 2012). After the reaction, the contents are put into containers for separation on a centrifuge. The material is centrifuged for 15 min to separate the solid and liquid contents. The liquid is filtered via vacuum filtration using 0.2 micron filter paper. The liquid is sampled and sent for ICP-MS. The solid residue is either kept for further experiments or it is stored.

### 3.3.2. Experimental program

To investigate the REE association with different phases in the deposit, Sanematsu and Kon (2013) studied the geochemical characteristics of a Chinese IAC deposit by multiple sequential extraction procedures, initially targeting the ion-exchangeable kaolinite with NaCl, then targeting ion-exchangeable halloysite with NaCH<sub>3</sub>COO. The third step is to target REE-organic compounds using tetra-sodium pyrophosphate (Na<sub>4</sub>PO<sub>3</sub>OPO<sub>3</sub>). This was the approach used in experiment (Exp) 1 shown in Table 3.1. All experimental residues are digested following the procedure in section 3.2.8 to determine the non-ion exchangeable REE in the mineral phase. Experiments 1 to 3 follow the step-wise extraction adapted from Sanematsu and Kon (2013), with the cation of the respective salt used changing from Na<sup>+</sup> to NH<sub>4</sub><sup>+</sup> to Mg<sup>2+</sup>. This is to compare the performance of these cations in a chloride system. Instead of using Mg-acetate in step 2 of experiment 3 (as it gives an alkaline solution), K-acetate is used due to the strong

affinity of halloysite for  $K^+$  (Joussein, 2005). The test is performed on samples A1 and A2 (experiments 4 to 6), two different regolith layers. Samples B and F were not analysed because the saprock samples were all sampled from the same depth and thus would perform similarly to sample A2, and are used instead for further tests.

Experiments 7 to 11 use 0.5 M NaCl to simulate seawater (approximately 0.47 M) as the samples originate from a coastal region where seawater could be used as a lixiviant. Ammonium sulphate is added to improve the performance. These experiments are conducted on sample A2 so that they compare to the geochemical characterisation in experiments 4 to 6.

**Table 3.1 Experiment number and lixiviant make up**

Exp		Lixiviant	Exp		Lixiviant			
1	Sample A1	1 M NaCl	12	Sample B	0.5 M $MgSO_4$			
		1 M $NaCH_3COO$	13		0.1 M $(NH_4)_2SO_4$ + 0.4 M $MgSO_4$			
		0.1 M $Na_4PO_3OPO_3$	14		0.25 M $(NH_4)_2SO_4$ + 0.25 M $MgSO_4$			
1 M $NH_4Cl$		15	0.4 M $(NH_4)_2SO_4$ + 0.1 M $MgSO_4$					
1 M $NH_4CH_3COO$		16	0.5 M $(NH_4)_2SO_4$					
2		Sample A2	0.1 M $Na_4PO_3OPO_3$	17	Sample B	1 M $NH_4NO_3$		
			0.5 M $MgCl_2$	18		0.1 M $(NH_4)_2SO_4$ + 0.8 M $NH_4NO_3$		
			1 M $KCH_3COO$	19		0.25 M $(NH_4)_2SO_4$ + 0.5 M $NH_4NO_3$		
0.1 M $Na_4PO_3OPO_3$			20	0.4 M $(NH_4)_2SO_4$ + 0.2 M $NH_4NO_3$				
1 M NaCl			21	0.5 M $(NH_4)_2SO_4$				
3			Sample A2	1 M $NaCH_3COO$	22	Sample F	0.05 M $(NH_4)_2SO_4$	
	0.1 M $Na_4PO_3OPO_3$			23	0.1 M $(NH_4)_2SO_4$			
	1 M $NH_4Cl$			24	0.25 M $(NH_4)_2SO_4$			
1 M $NH_4CH_3COO$	25			0.5 M $(NH_4)_2SO_4$				
0.1 M $Na_4PO_3OPO_3$	26			1 M $(NH_4)_2SO_4$				
4	Sample A2			0.5 M $MgCl_2$	27	Sample A1	0.5 M $(NH_4)_2SO_4$ + 0.0025 M $NH_4CH_3COO$	
		1 M $KCH_3COO$		28	0.5 M $(NH_4)_2SO_4$ + 0.005 M $NH_4CH_3COO$			
		0.1 M $Na_4PO_3OPO_3$		29	0.5 M $(NH_4)_2SO_4$ + 0.01 M $NH_4CH_3COO$			
0.5 M NaCl (SS)		30		0.5 M $(NH_4)_2SO_4$ + 0.02 M $NH_4CH_3COO$				
5		Sample A2		SS + 0.05 M $(NH_4)_2SO_4$	31		Sample F	0.5 M $(NH_4)_2SO_4$ + 0.05 M $NH_4CH_3COO$
				SS + 0.1 M $(NH_4)_2SO_4$	32	0.5 M $(NH_4)_2SO_4$ + 0.0025 M $NH_4CH_3COO$		
			SS + 0.25 M $(NH_4)_2SO_4$	33	0.5 M $(NH_4)_2SO_4$ + 0.005 M $NH_4CH_3COO$			
6			Sample A2	SS + 0.4 M $(NH_4)_2SO_4$	34	Sample F		0.5 M $(NH_4)_2SO_4$ + 0.01 M $NH_4CH_3COO$
					35			0.5 M $(NH_4)_2SO_4$ + 0.02 M $NH_4CH_3COO$
					36		0.5 M $(NH_4)_2SO_4$ + 0.05 M $NH_4CH_3COO$	

Experiments 12 to 16 vary the compound lixiviants  $(\text{NH}_4)_2\text{SO}_4$  and  $\text{MgSO}_4$  in the charge ratios of 0:1, 1:4, 1:1, 4:1 and 1:0 to investigate the effect of supplementing the lixiviant with Mg ions. The ratios used are similar to the experiments by Yanfei *et al.* (2016). Experiments 17 to 21 vary the compound lixiviants  $(\text{NH}_4)_2\text{SO}_4$  and  $\text{NH}_4\text{NO}_3$  in the ratios 0:1, 1:4, 1:1, 4:1 and 1:0 to test the permeability effects of the nitrate ion. The ratios used are similar to the experiments by Zhengyan *et al.* (2016). These experiments are conducted on sample B.

Experiments 22 to 26 varies the ionic strength of the ammonium sulphate lixiviant from 0.05 to 1 M. These are conducted on sample F. Experiments 27 to 36 vary the buffering agent ammonium acetate in a constant 0.5 M ammonium sulphate solution to reduce the leaching of Al. This is conducted on both regolith layers A1 and F as sample A1 is likely to be Al enriched.

All the samples are prepared as described in section 3.1.2 with each sample mixed and split so that each experiment in Table 3.1 has the sample with the same REE grade. The experiments were conducted in order to maximise the range of experiments investigated and reduce costs associated with ICP-MS analysis. The main source of error was associated with the ICP-MS analysis, using small sample masses (50 mg) which require dilution, so precision and accuracy were determined against digested USGS rock standards to determine uncertainty in the measurement.

## 4. RESULTS AND DISCUSSION

### 4.1. Ore Characterisation

#### 4.1.1. Samples A1, A2, B and F

The leaching of *in-situ* ion-adsorption clays requires knowledge about the process, ore mineralogy and regional geology. Ore mineralogy is a useful tool to the engineer for process monitoring and improving process performance. For *in-situ* leaching, characterising the ore body is essential in determining the clay minerals present, the ion-exchangeable REE grade and variability in texture of gangue minerals. In *in-situ* leaching the ore body is left relatively undisturbed, therefore the texture of the ore body needs to be characterised to determine its impact on ion-exchange.

Sample A1 was sampled from the pedolith (5 to 6.5 m). It appears homogeneous and red in colour indicating that the primary texture has been destroyed in an iron oxide rich zone. Samples A2, B and F were sampled from the saprolith (6.5 to 10 m) and appear heterogeneous, indicating that the primary texture is preserved, as illustrated in Figure 4.1.

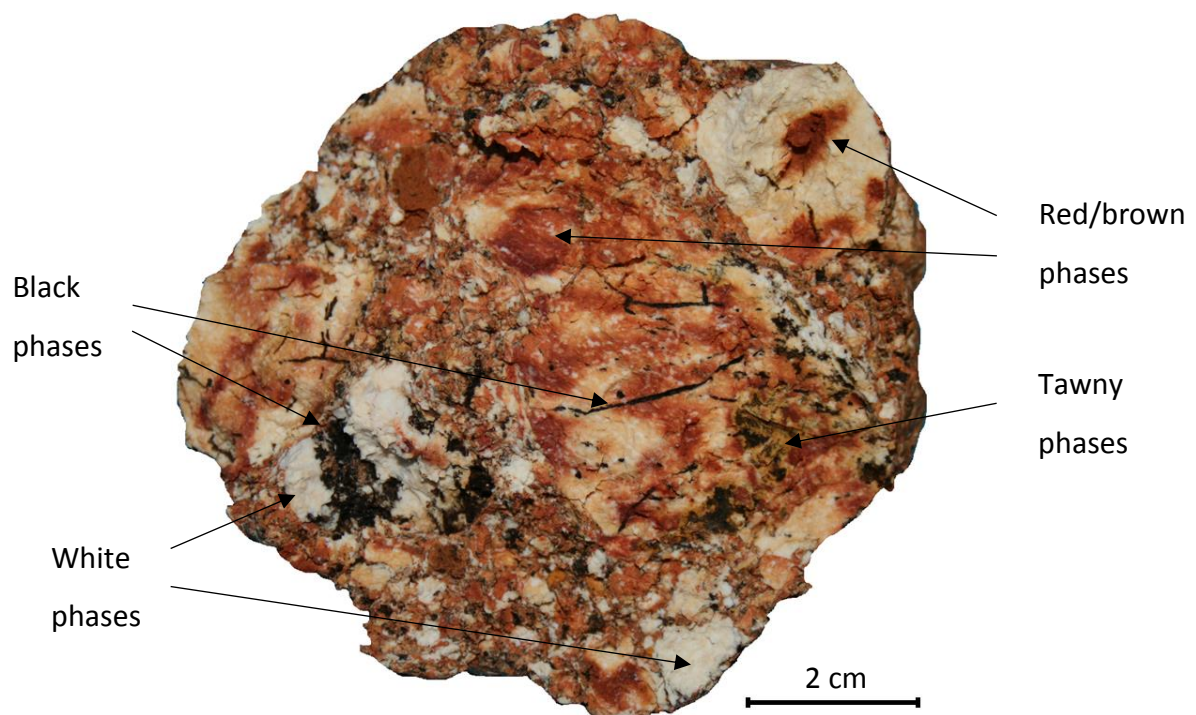


**Figure 4.1 Sample B clay and gangue mineral heterogeneity**

The main visual characteristics of samples A2, B and F are the presence of white, black, red/brown and tawny (orange/yellowish-brown) phases. The white phases indicate the type



of kaolinite used in the manufacture of fine china and the paper industry (Bertolino *et al.*, 2010). The black phases appear interspersed in the fine grained matrix, as veins, or as larger coarse grained phases. The red/brown phases appear in a variety of colours ranging from rust brown to brick red, either as discrete phases or interspersed in the white phases.

#### 4.1.2. Particle Size Distribution (PSD) results

Clay minerals are negatively charged particles, which contributes to the formation of agglomerates. A dispersant was added to combat this effect in the analysis of the sample particle size distribution; the results from the Malvern analysis are shown in Figure 4.2.

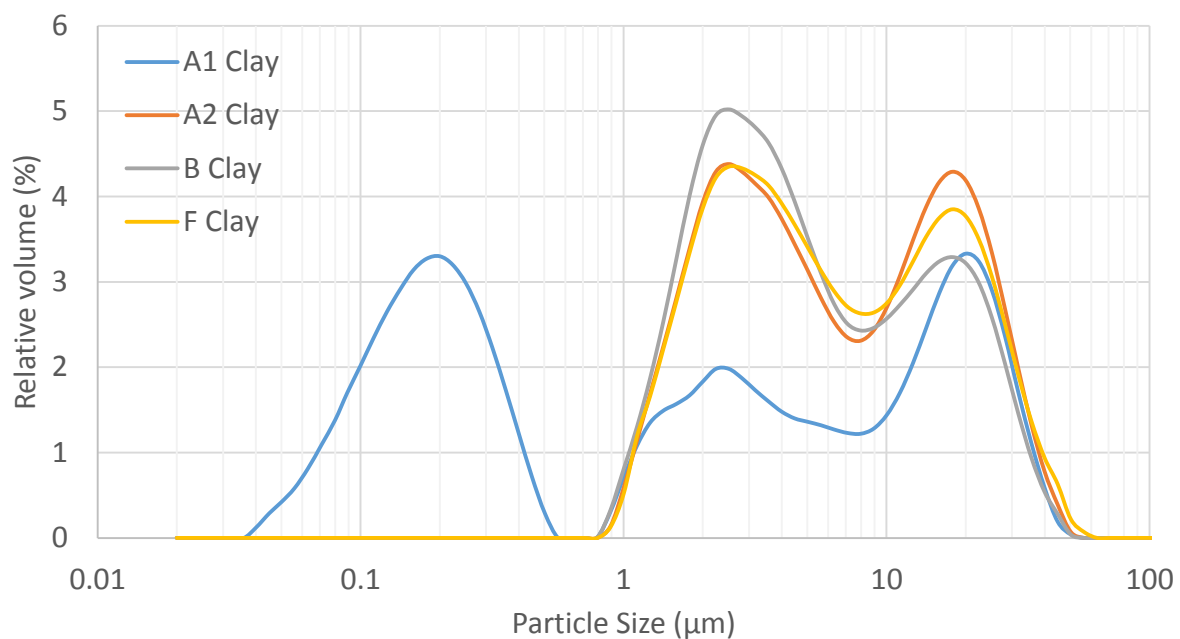


**Figure 4.2 Particle size versus relative volume of clay samples using the Malvern Masterizer (<38 μm size fraction)**

Sample A1 shows some deviation in its PSD compared with the deeper samples A2, B and F. All samples show a peak at approximately 2.2 μm, which corresponds with the particle size for kaolinite. A1 shows a relative depletion in this particle size (2.3 – 3 %) compared with the other three, indicating that the kaolin is not as well crystallised. Samples A2 and F are very similar to one another with a relative volume of 4.3 %. Sample B shows a distinct peak with the greatest relative volume at 5 %. Sample A1's depletion at 2 μm is a consequence of degradation and precipitation characteristic of pedolithic horizons as indicated from the presence of a peak at 0.2 μm (3.3 %) which could be due to poorly crystallised kaolinite and iron oxide minerals.

Samples A2, B and F have a final peak at 17.8  $\mu\text{m}$  with sample A1 peaking at 21.0  $\mu\text{m}$ . This relates to weathered primary silicates such as K-feldspar and quartz. The samples A2 and F have relatively more of these particles at 4.3 and 3.8 % respectively, compared with A1 and B at 3.2 %. As Figure 4.3 in the following section suggests, this relative predominance in A2 and F could be due to an increased presence of K-feldspar.

#### 4.1.3. X-Ray Fluorescence (XRF) results

XRF was used to determine the bulk chemical composition for the < 38 micron sample, the results given in Figure 4.3.

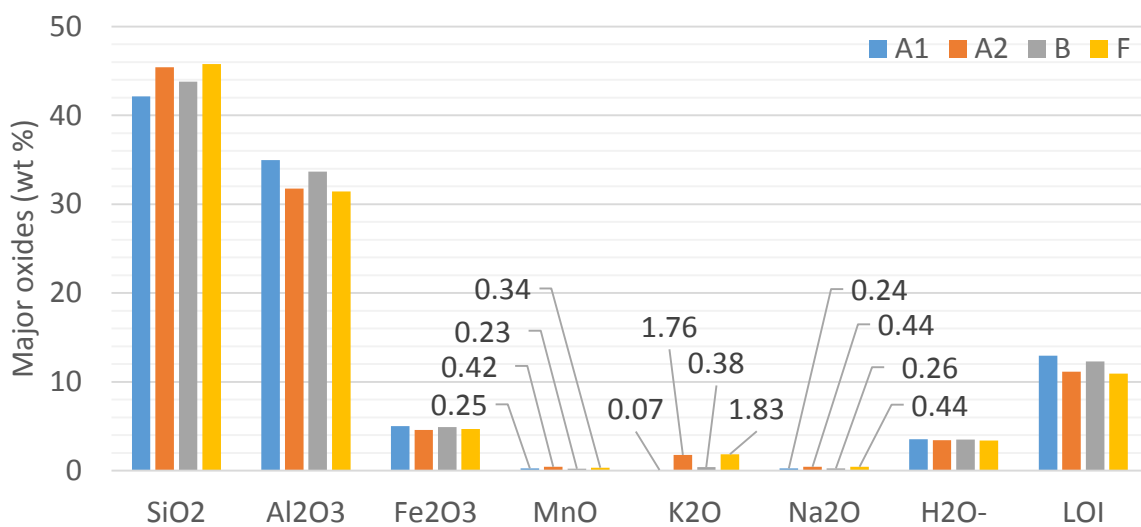


**Figure 4.3 Major oxides determined by XRF for samples A1, A2, B and F**

The major oxides are SiO<sub>2</sub> and Al<sub>2</sub>O<sub>3</sub>, the majority made up by kaolin. The Al<sub>2</sub>O<sub>3</sub> content would be increased due to Al minerals such as gibbsite, and the SiO<sub>2</sub> content due to quartz. The Si to Al ratio for the sample A1 is 1.21 (reference kaolinite Si/Al ratio is 1.18), which is the lowest of the four samples. This is likely due to increased concentrations of gibbsite towards the surface of the weathering front (as per figure 2.16). The Si to Al ratios for samples A2 and F are similar at 1.43 and 1.46 respectively. This trend follows from the PSD suggesting the increased ratios for sample A2 and F are due to other silicate minerals present such as quartz and K-feldspar. Sample B has a ratio of 1.30 which suggests less Si enrichment from quartz and K-feldspar (also suggested from the low K<sub>2</sub>O content of 0.38 wt %). All the samples contain Fe<sub>2</sub>O<sub>3</sub> (5.01, 4.58, 4.89 and 4.67 wt % respectively) with A1 being the most enriched. All the samples contain a small amount of MnO (0.25, 0.42, 0.23 and 0.34 respectively), indicating that only a small portion of Mn particles are below 38 microns.

The Chemical Index of Alteration (CIA) values for the four samples A1, A2, B and F are 99.1, 93.5, 98.1 and 93.3 respectively. Samples A1 and B show almost complete alteration due to very low K<sub>2</sub>O and Na<sub>2</sub>O contents (CaO was below detection limit of < 0.01 wt %) whereas samples A2 and F retain a small portion of their original silicate structure (1.76 and 1.83 wt % respectively). The contents of K, Na and Ca show that Ca-feldspars are weathered first, followed by Na-feldspars and K-feldspars, as discussed in section 2.2.8.

Minor elemental analysis results are shown in the Appendix 6.3.1 Table 6.5, showing the presence of manganese and zirconium in all the samples.

#### 4.1.4. X-Ray Diffraction (XRD) results

The chemical structures of the samples were analysed using X-ray diffraction; the results are shown in Figure 4.4.

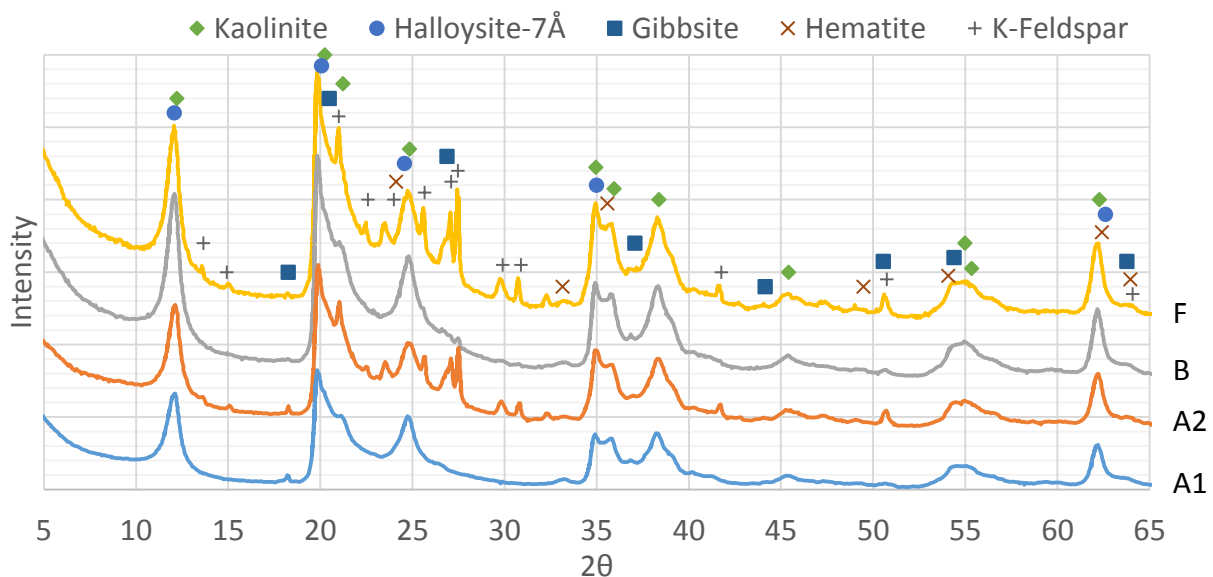


**Figure 4.4 X-ray diffractogram and mineral analysis**

Clay minerals were identified by their diffraction peak locations of their basal (00 $l$ ) reflections. Kaolinite was shown to be the major clay component with reflection of 001 at 7.20 Å (12.3 ° 2 $\theta$ ). The distinct sharp peak at 1.49 Å (62.2 ° 2 $\theta$ ) showing 060 reflection confirms the dioctahedral character of the clay. The presence of a slightly stronger peak of 020 reflection at 4.45 Å (20.0 ° 2 $\theta$ ) compared with the first peak at 12.3 ° 2 $\theta$  indicates the presence of either halloysite or kaolinite-smectite. The diffraction pattern is highly disordered due to the presence of gibbsite, hematite and K-feldspar as indicated.

Ethylene glycol (EG) saturation was applied to all the samples aimed at expandable clays (smectite) and formamide saturation was aimed at differentiating halloysite from kaolinite at the 7.20 Å overlap. The results from the EG treatments showed no apparent movement of the basal reflections suggesting that there is no expandable smectite present. The formamide saturation showed broad but distinct reflections ranging between 10.2 and 10.5 Å caused by the complex formation that expands the halloysite structure as a result of formamide intercalation (Theng *et al.*, 1984), shown in Figure 4.5.

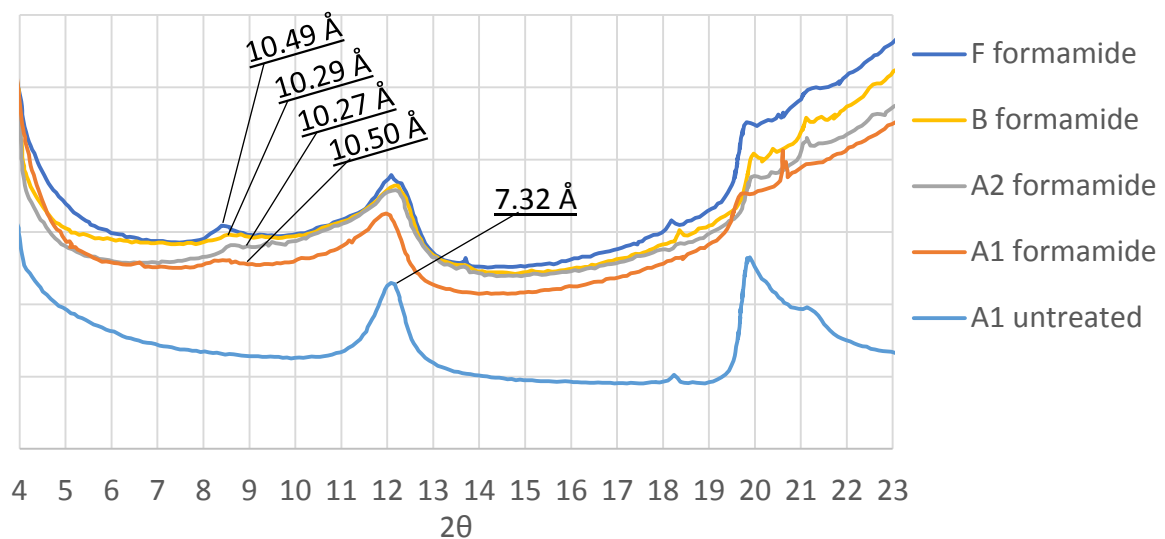


**Figure 4.5 Intercalation of formamide showing expansion of halloysite**

The quantitative proportions of kaolinite to halloysite and results of the whole rock mineralogy were determined by the Rietveld Method (Hill and Howard, 1987) and are shown in Table 4.1.

**Table 4.1 Quantitative analysis of whole rock mineralogy using the Rietveld Method (wt %)**

Mineral	Composition	A1	A2	B	F
Kaolinite	$Al_2Si_2O_5(OH)_4$	74.9	69.6	80.9	68.8
Halloysite-7Å	$Al_2Si_2O_5(OH)_4$	22.2	20.6	18.9	18.6
K-Feldspar (microcline)	$K(AlSi_3O_8)$	n.d.	9.2	n.d.	10.4
Gibbsite	$Al(OH)_3$	1.6	0.55	trace	2.2
Hematite/Goethite	$Fe_2O_3/FeO(OH)$	1.3	trace	trace	trace

Where n.d. indicates minerals not detected and trace indicates quantities < 0.5 wt %.

Kaolinite is confirmed to be the major clay mineral present. The amount of halloysite was determined to be between 18.6 and 22.2 wt %. Contrary to the weathering paths in Figure

2.17, the greatest amount of halloysite was in sample A1 and sample F has the highest amount of gibbsite (2.2 wt %). Sample A2 and F contain appreciable amounts of K-feldspar at 9.2 and 10.4 wt % respectively, confirming that weathering hasn't completely altered these samples, as opposed to sample B which is almost completely kaolin (kaolinite and halloysite). All the samples contained some amount of hematite/goethite, as indicated by the very similar contents of  $\text{Fe}_2\text{O}_3$  in the XRF results (Figure 4.3), but only sample A1 was characterised quantitatively with XRD.

The Hinckley Index values for these samples are 0.29, 0.40, 0.32 and 0.44 respectively; calculations are shown in the Appendix 6.3.2 Figure 6.7 and Table 6.6. This shows that sample A1 is the most poorly crystalline followed by sample B, while sample F and A2 are the most crystalline.

#### 4.1.5. QEMSCAN results

In traditional ore beneficiation processes the knowledge of mineralogy, together with mineral association and textural parameters, can greatly influence mineral processing routes and hence recovery (Santoro *et al.*, 2015). For *in-situ* leaching, the information provided by QEMSCAN analysis will identify gangue minerals responsible for impurities in the leachant, and investigate the mineral association with kaolinite to better understand *in-situ* leaching conditions. Figure 4.6 shows a block mount for sample A1, illustrating the characteristic red colour of the pedolith, and its associated false colour QEMSCAN field image.

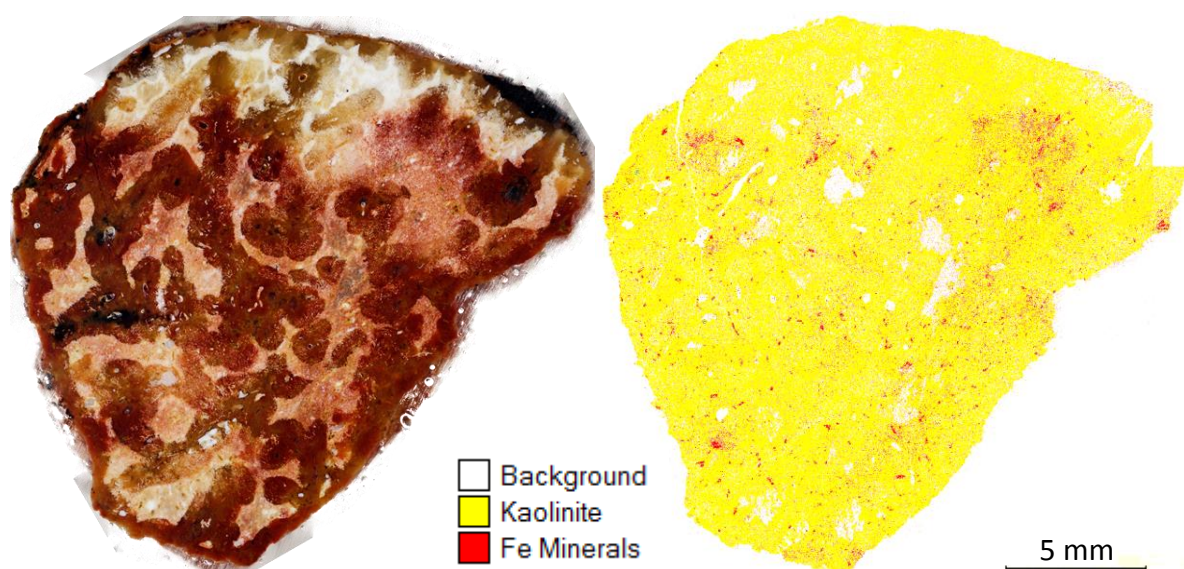


**Figure 4.6 Sample A1 block mount (left) (block 2) and false colour field scan image (right)**

Figure 4.6 confirms the red colour is due to a homogenous distribution of Fe minerals (2.22 wt %) throughout the kaolin (kaolinite and halloysite 97.1 wt %). The presence of white background phases in the false colour image indicates depressions on the surface of the block, due to the difficulties associated with polishing clay. 'Fe minerals' includes the grouping of hematite and goethite because the X-ray spectra are not precise enough to distinguish between the two phases (Santoro *et al.*, 2015). The QEMSCAN field images for saprolithic samples F and A2 are shown in Figure 4.7.

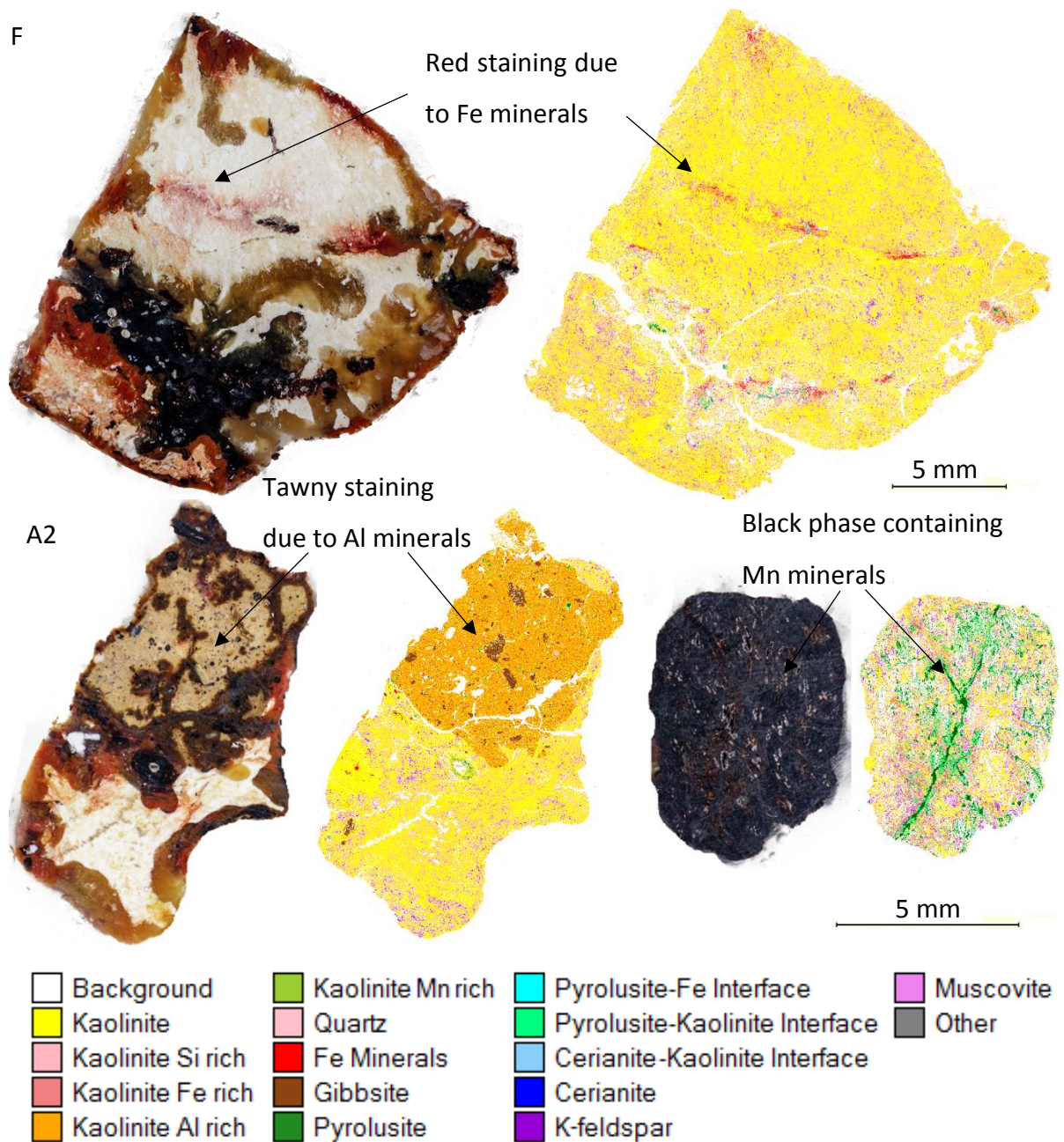
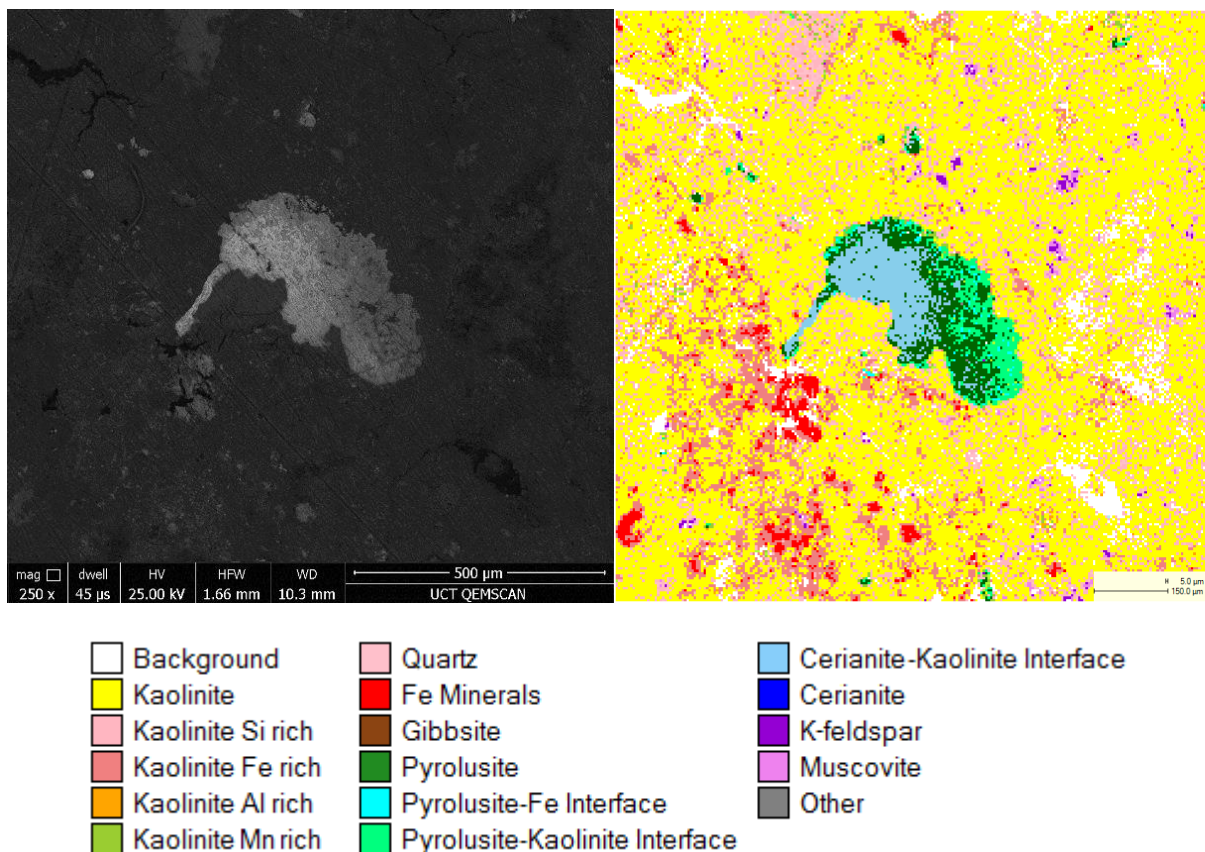


Figure 4.7 Sample F and A2 block mounts (left) (blocks 9 and 4) and false colour field scan image (right)

Contrary to sample A1, where the clay is red throughout, the saprock samples show localised regions of clay with varying degrees of discolouration. Sample F in Figure 4.7 shows that Fe is responsible for the red staining of the white kaolin. The presence of K-feldspar is confirmed in sample F, occurring throughout the clay, mainly in off-white clay phases and associated with the Mn minerals. Sample A2 in Figure 4.7 shows that the tawny phase is due to the presence of Al minerals. The surrounding kaolin also has elevated levels of Al, having a reduced Si/Al ratio in this region.

The black phase has been identified to contain Mn minerals which are associated with K-feldspar, Fe minerals and cerianite. Sample A2 in Figure 4.7 shows a Mn vein associated with K-feldspar and kaolinite. As expected from an ion-adsorption clay deposit, Ce was scavenged by Mn minerals (Ohta and Kawabe, 2001). Figure 4.8 shows a BSE image of a Mn mineral with Ce deposited on its surface.



**Figure 4.8 Sample B BSE image (left) showing Mn mineral with Ce scavenged on its surface as shown by the false colour field image (right)**

The brightness from the BSE image is a function of the average atomic number. In Figure 4.8 the brightest sections of the mineral are attributed to cerianite ((Ce,Th)O<sub>2</sub>) and pyrolusite (MnO<sub>2</sub>). More examples of block mounts for samples A1, A2, B and F are shown in the Appendix 6.3.3 Figures 6.8 to 6.12. The quantitative mineral content for all the block mounts is shown in Table 6.7 and 6.8. Field images showing Fe, Mn and Ce textures are shown in Figures 6.13 to 6.21.

Figure 4.9 shows that muscovite forms as an intermediate between the K-feldspar and the kaolinite. Kaolinite with higher levels of Fe is also found surrounding Fe minerals. The presence of quartz is also confirmed from QEMSCAN, with some regions of kaolinite showing elevated Si content. The presence of muscovite and quartz was not identified in the XRD pattern due to their low content.

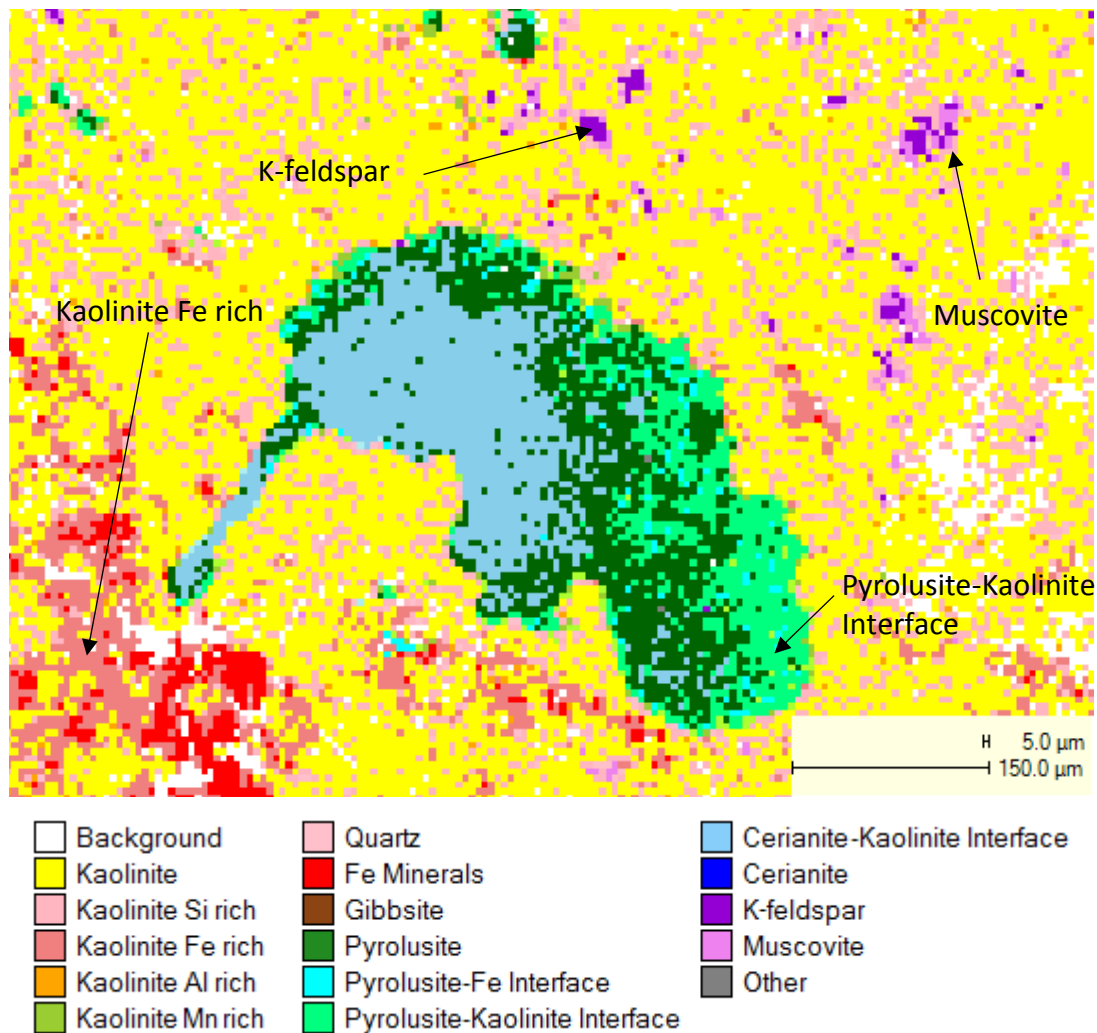


**Figure 4.9 Sample B false colour field image highlighting K-feldspar, Muscovite, Pyrolusite-Kaolinite Interface and kaolinite Fe rich**



QEMSCAN is a powerful tool used to investigate the clay surface texture, allowing for detailed mapping on the micrometre scale. The drawback to this method is that clay minerals by definition are on the 2 micron scale, thus with 10 micron pixels, the information in each will likely be that of multiple particles. Spectra containing mainly Si and Al with elevated levels of Fe are grouped together as Kaolinite Fe rich. Similarly groups are made with elevated Si, Al and Mn levels. Pyrolusite containing mixed spectra from Fe minerals are grouped as Pyrolusite-Fe Interface and Pyrolusite bordering Kaolinite are grouped as Pyrolusite-Kaolinite Interface.

The other drawback with using QEMSCAN is that it cannot distinguish between kaolinite and halloysite, which can only be distinguished with XRD.

#### 4.1.6. Scanning electron microscopy (SEM) results

To investigate the clay mineral morphology, scanning electron microscopy is used. Secondary electron images showing the morphology of the white kaolin phase is shown in Figure 4.10.

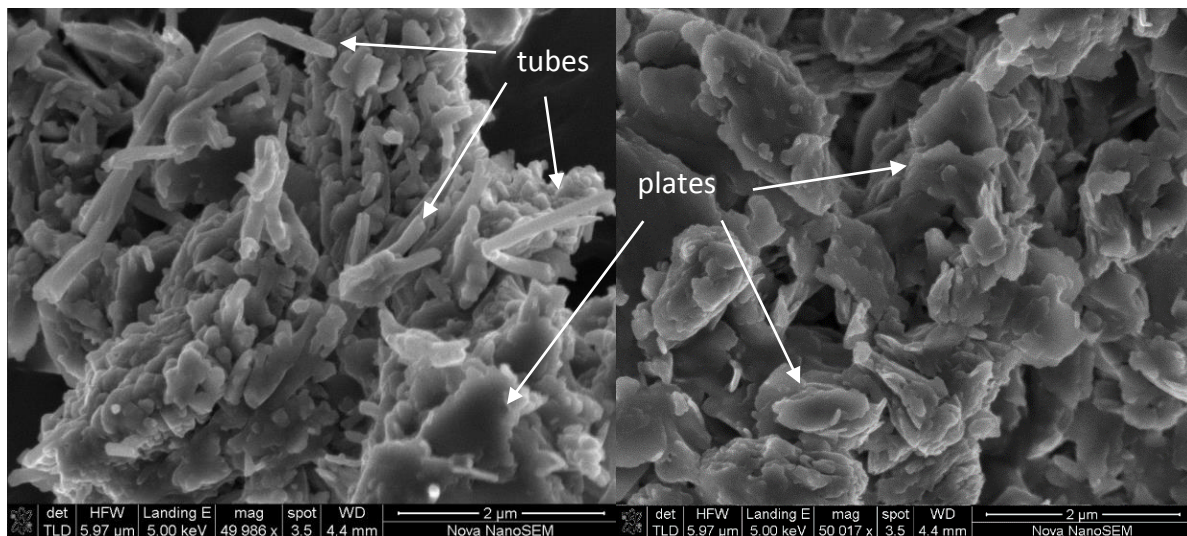


**Figure 4.10 Sample A2 white kaolin SEM images showing some tubular morphology (left) and highly disordered platy morphology (right)**

This phase shows evidence of tubular morphology, indicating the presence of halloysite-7Å. These tubes are highly disordered, ranging in length from 1 µm to 15 µm. These tubes are commonly bent and irregular, resulting from environmental growth restrictions and continuous rolling and un-rolling during weathering.

The majority of the kaolinite is platy, as expected from the amount of kaolinite determined with Rietveld Analysis using XRD. The low quantity of tubes found with SEM would suggest that the majority of the halloysite-7Å is platy/un-rolled tubes. This can be attributed to the drying process during sampling. The platy kaolin (kaolinite and halloysite) shows a highly defective structure, as shown by the low Hinckley Indexes determined from XRD. Defects in the structure of kaolinite lead to broken surface bonds allowing for greater surface charge effects (Zhu *et al.*, 2016).

The black fraction has been shown to contain Mn minerals, K-feldspar and kaolinite. Figure 4.11 shows the structure of these minerals.

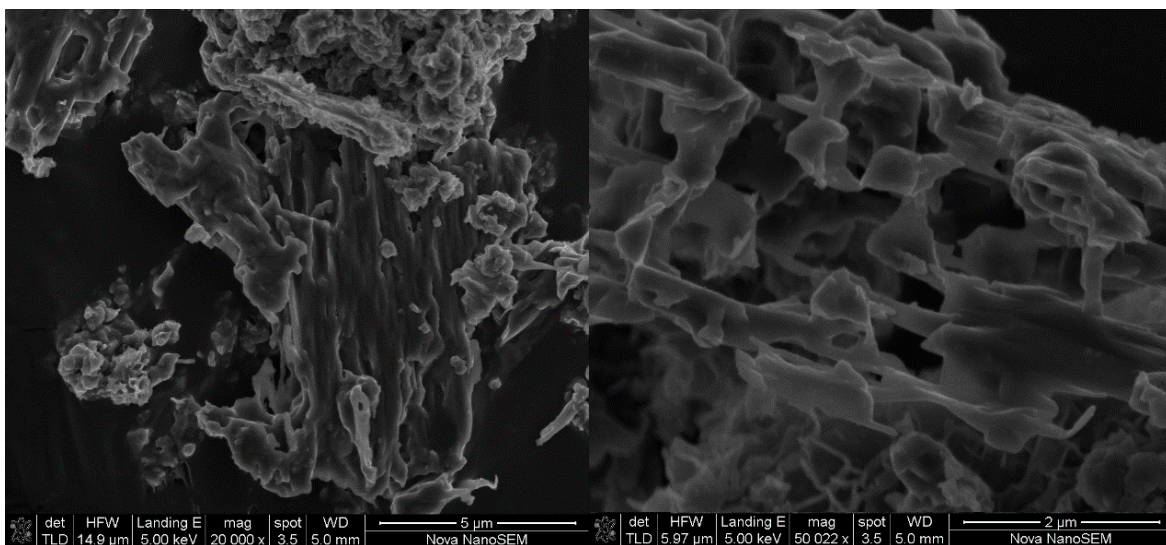


**Figure 4.11 Sample A2 black phase showing Mn minerals (left) and K-feldspar (right)**

These structures are typical of weathered material with the majority of the original structure removed. The remaining skeletal structure can have kaolinite plates attached, and is the reason for the 17.8 μm peak in the PSD analysis. Analysis of the kaolinite red phase was shown in the Appendix 6.3.9 Figure 6.25, and also shows highly defective structures, but no correlation could be made with the Fe present. The tawny phase shows kaolinite plates attached to gibbsite in Figure 6.24.

#### *4.1.7. Transmission electron microscopy (TEM) results*

The influence of Fe on the structure of kaolinite can be seen through the use of TEM imaging. Figure 4.12 shows a kaolinite particle from the white phase with its associated element map. The particle shows very little Fe incorporated in the kaolin structure.

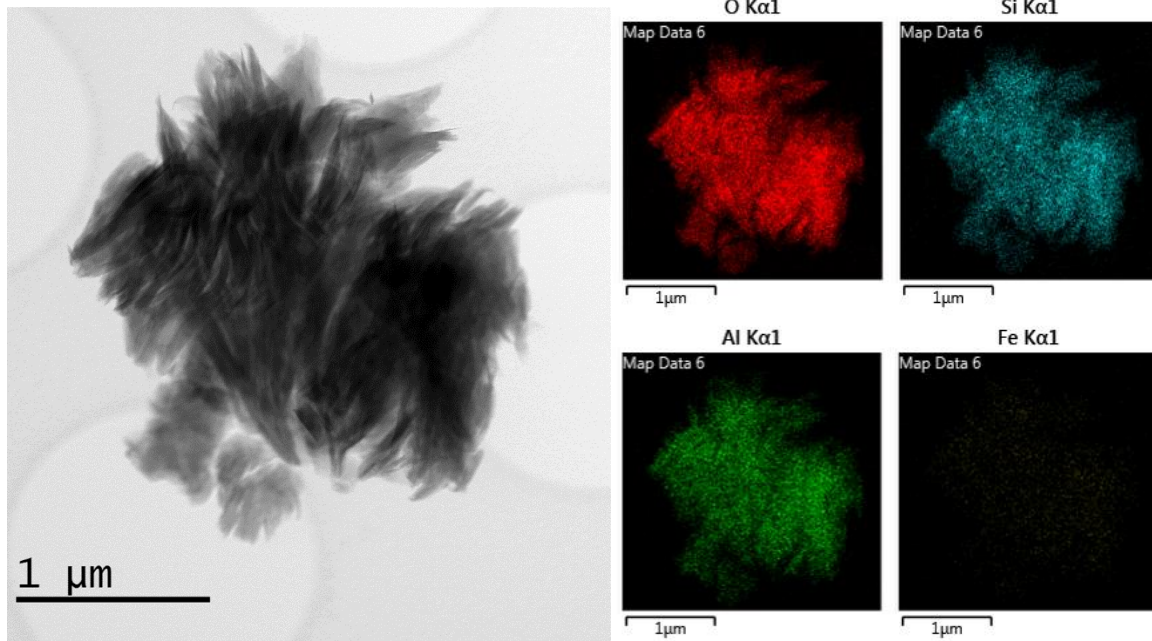


**Figure 4.12 White phase kaolinite TEM image with element map**

Figure 4.13 shows a kaolinite particle from the red phase. The surface of the kaolinite particle was shown by the element map to contain iron oxide, formed by metal adsorption illustrated in Figure 2.18.

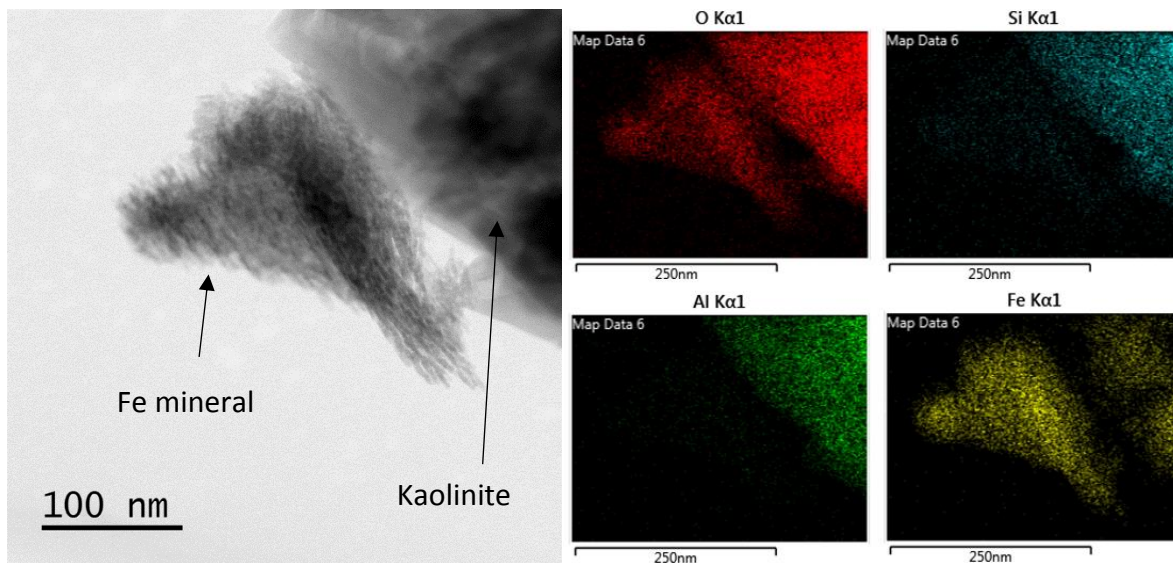


**Figure 4.13 Red phase TEM image showing Fe mineral alongside kaolinite with element map**

The element map also shows a large incorporation of Fe in the kaolinite structure, likely replacing Al in the octahedral layer. This iron oxide crystal is responsible for creating stable porous “card house” structures found in kaolin rich tropic soils (Tawornpruek *et al.* 2006).

#### 4.1.8. ICP-MS results

The overall REE grade was determined with ICP-MS using the clay digestion method described in section 3.2.8. The results are shown in Table 4.2, indicating the sample concentration in parts per million (ppm) and uncertainty associated with the measurement.

**Table 4.2 ICP-MS results for samples A1, A2, B and F prior to chondrite normalisation**

REE		Sample A1		Sample A2		Sample B		Sample F	
		ppm	±	ppm	±	ppm	±	ppm	±
La	57	411	0.7	3 033	0.7	2 461	0.4	3 269	0.8
Ce	58	538	0.5	459	0.5	633	0.2	471	0.9
Pr	59	79	0.8	557	0.4	460	0.6	603	0.3
Nd	60	223	0.6	1 488	0.3	1 235	0.2	1 603	0.5
Sm	62	31	0.7	194	0.6	158	0.4	211	0.5
Eu	63	3	0.9	20	1.0	16	0.6	22	0.0
Gd	64	21	0.7	146	0.4	113	0.6	158	0.7
Tb	65	4	0.6	25	0.3	19	0.6	27	0.2
Dy	66	22	0.7	131	1.0	101	0.2	143	0.6
Y	39	128	0.6	923	0.6	685	0.6	989	0.2
Ho	67	6	1.1	32	0.4	25	0.4	35	1.0
Er	68	16	0.5	96	1.0	73	0.5	104	0.7
Tm	69	3	1.4	15	0.8	11	0.4	16	0.4
Yb	70	15	0.7	76	0.1	60	0.8	82	0.9
Lu	71	3	0.6	15	0.3	12	0.5	16	0.1
LREE		1 285	4.2	5 751	3.4	4 963	2.3	6 179	3.1
HREE		219	7.0	1 458	4.9	1 098	4.4	1 570	4.8
TREE		1 503	11.2	7 209	8.3	6 061	6.8	7 749	7.9

The results show that the pedolith sample A1 (TREE = 1 503 ppm) is depleted in REE compared with the saprock samples (TREE = 7 209, 6 061 and 7 749 ppm respectively). This is due to REE leaching and surficial erosion, promoting the continuous cycling of REE to deeper soil regions (Aide and Aide, 2012). The REE exhibit the Oddo-Harkin's Rule with depletion in the concentrations of odd atomic number REE, therefore the samples are chondrite normalised (McDonough and Sun, 1995) to determine the REE characteristics. Figure 4.14 shows the chondrite normalised results (ratio of measured REE to chondrite REE amount) from the 4 samples alongside the composition of light and heavy Chinese ion-adsorption ores (Kynicky *et al.*, 2012).

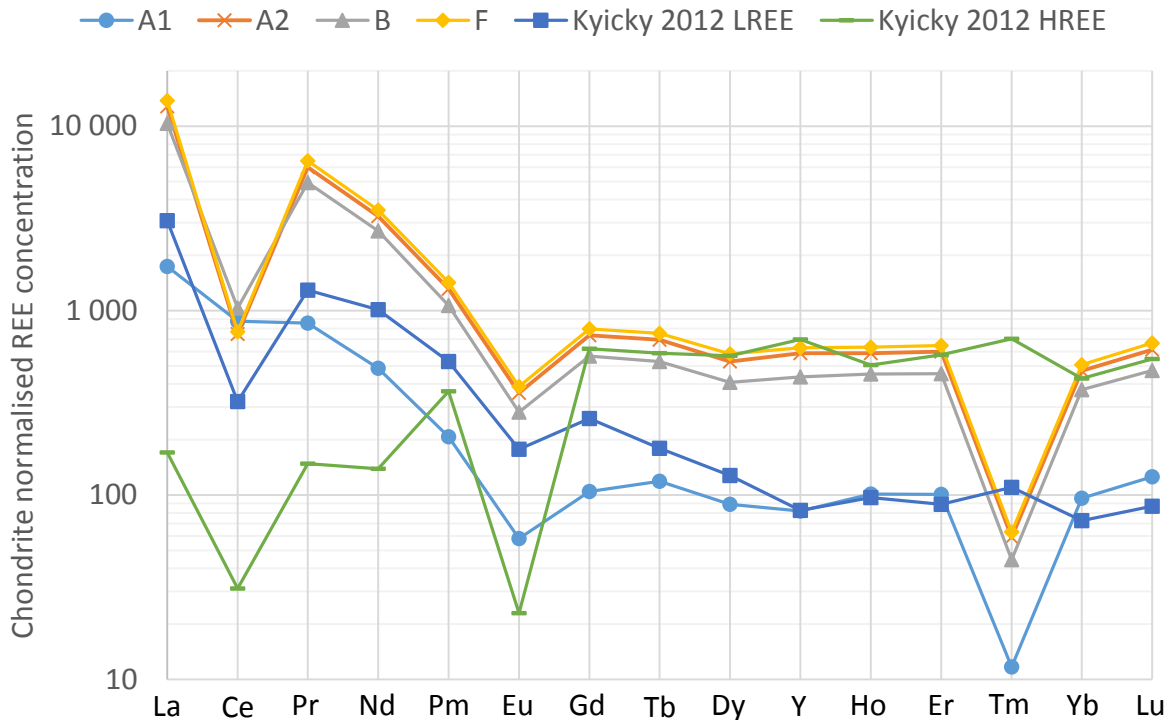


**Figure 4.14 ICP-MS results for the bulk chondrite normalised REE grade**

All the samples show negative Ce, Eu and Tm anomalies, with the exception of Ce in sample A1. The LREE slope (La / Gd) and HREE slope (Gd / Lu) as well as the negative Ce, Eu and Tm values are given in Table 4.2.

**Table 4.3 LREE and HREE slopes and negative REE anomalies values**

	A1	A2	B	F	Kyicky 2012 LREE	Kyicky 2012 HREE
La / Gd	16.6	17.4	18.3	17.4	11.9	0.27
Gd / Lu	0.83	1.20	1.19	1.19	2.98	1.14
Ce / Ce*	0.72	0.09	0.14	0.08	0.16	0.20
Eu / Eu*	0.40	0.36	0.36	0.36	0.48	0.05
Tm / Tm*	0.12	0.11	0.11	0.11	1.37	1.42

The La / Gd ratios suggest that all the samples are LREE enriched because they all are above the LREE La / Gd ratio of 11.9 from Kyicky (2012). Sample A1 follows the same profile as the LREE ore indicating no HREE enrichment in this horizon. The saprock samples show HREE enrichment, having a Gd / Lu ratio greater than the 1.14 of the HREE enriched ore by Kyicky (2012). As shown in Figure 4.14 the saprock REE profiles follow both the LREE and HREE profiles of Kyicky (2012), showing greater LREE enrichment than HREE but containing relatively more HREE than a purely LREE enriched ore.

The Ce anomaly value in sample A1 of 0.72 is greater than the saprock samples, indicating an accumulation of Ce towards the top of the horizon as shown by Bao and Zhou (2008). The Eu anomaly values are typical for peralkaline and iron-REE deposits (Castor and Hedrick, 2006), whereas the Tm anomaly is unique to this deposit. Samples A2 and F are the most REE enriched, followed by sample B. This is related to the clay crystallinity, with the XRD results showing that samples A2 and F are the most crystalline (Hinckley Indices 0.40 and 0.44 respectively) with sample B showing less crystallinity (0.32).

The heterogenic phases indicated in Figure 4.1 show variability in the REE concentration, as shown with sample A2 in Figure 4.15.

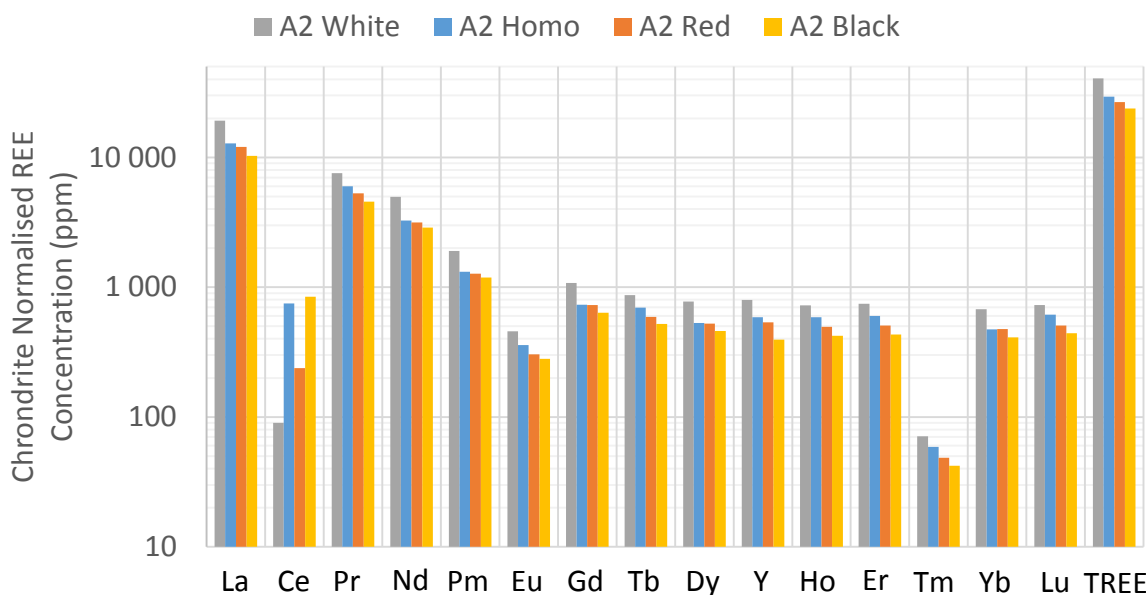


**Figure 4.15 Sample A2 REE concentration distribution among the white, red and black phase compared to homogenised concentration**

The distribution of REE in the other samples is shown in the Appendix 6.3.9 Figure 6.25 to 6.27 with all samples showing a relative depletion of REE in the red phase. This is likely due to Fe minerals (as shown in Figure 4.13) competing with the REE for surface space on the kaolin particles (Hart *et al.*, 2002). The white phase shows a variety of enrichments, being more REE rich (compared to the homogenous mixture) in sample A2 and but less rich in sample B (22 138 ppm in the white phase compared to 24 167 ppm in the homogenous mixture). The black phase is enriched in sample B, however the QEMSCAN analysis in Figure 4.7 shows that kaolinite forms part of this structure. Therefore it cannot be determined

whether the REEs are in the ion-exchangeable kaolin phase or exist as insoluble oxide or hydroxides.

## 4.2. Lixiviant Tests

### 4.2.1. Geochemical characterisation

The aim of geochemical characterisation was to determine by sequential leach extraction the REE distribution in the kaolinite, halloysite, colloidal REE-organic and mineral phases, as described in section 3.3.2. The secondary aim was to compare the ion-exchange capabilities between  $\text{Na}^+$ ,  $\text{NH}_4^+$  and  $\text{Mg}^{2+}$ . The results from the step-wise extraction for samples A1 and A2 are shown in Figure 4.16.

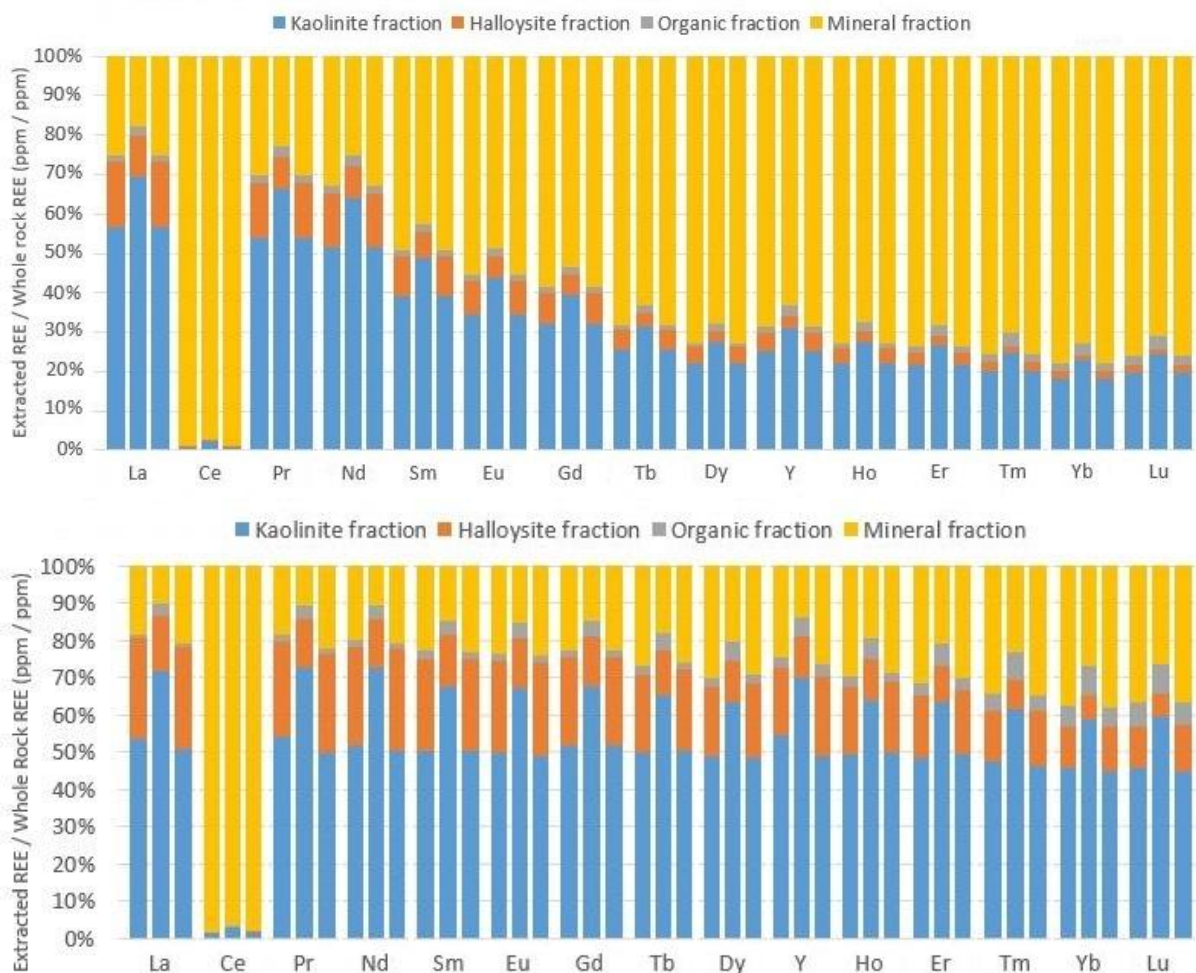


**Figure 4.16 Sample A1 (top) and A2 (bottom) sequential leach extraction comparing the recoveries between  $\text{Na}^+$ ,  $\text{NH}_4^+$  and  $\text{Mg}^{2+}$  respectively (experiments 1, 2 and 3 top; 4, 5 and 6 bottom)**

The whole rock REE concentrations for sample A1 in experiments 1 to 3 were 1 076, 1 116 and 1 471 ppm respectively and 5 046, 5 620 and 5 253 ppm for sample A2. This shows that there is variation in the REE concentration amongst the split samples. The recovery from each sequential step was determined from the REE extracted relative to the whole rock concentration for each experiment, shown in Table 4.4. The kaolinite recovery trend for sample A1 in Figure 4.16 follows a similar trend to that of the overall REE grade for this material (Figure 4.14) with improved LREE recoveries over HREEs (38.6 % compared to 32.4 %).

**Table 4.4 Geochemical characterisation sequential leach extraction recoveries**

Sample	A1				A2			
	Na <sup>+</sup>	NH <sub>4</sub> <sup>+</sup>	Mg <sup>2+</sup>	Ave	Na <sup>+</sup>	NH <sub>4</sub> <sup>+</sup>	Mg <sup>2+</sup>	Ave
Kaolinite	28.7%	37.7%	22.2%	29.5%	48.2%	66.9%	46.7%	53.9%
Halloysite	9.0%	5.1%	5.9%	6.7%	22.5%	12.7%	23.9%	19.7%
Organic	1.7%	1.6%	0.8%	1.4%	1.5%	3.5%	1.4%	2.2%
Mineral	60.5%	55.7%	71.1%	62.4%	27.8%	16.9%	27.9%	24.2%
Recovery	Na <sup>+</sup>	NH <sub>4</sub> <sup>+</sup>	Mg <sup>2+</sup>	Ave	Na <sup>+</sup>	NH <sub>4</sub> <sup>+</sup>	Mg <sup>2+</sup>	Ave
LREE	41.2%	46.0%	28.7%	38.6%	71.8%	82.9%	72.0%	75.6%
HREE	30.9%	35.9%	30.6%	32.4%	73.9%	83.9%	72.6%	76.8%
TREE	39.5%	44.3%	28.9%	37.6%	72.2%	83.1%	72.1%	75.8%
TREE Excluding Ce	59.7%	67.8%	60.5%	62.7%	79.3%	88.4%	77.5%	81.7%

The REE recovery trend from kaolinite for sample A2 in Figure 4.16 is consistent across the REEs, with the average recovery of LREEs 75.6 % compared to 76.8 % for the HREEs. Both samples show that Ce is present as part of the mineral phase, as shown in the QEMSCAN analysis. In sample A1 the TREE recovery was only 29.5 % on average for the kaolinite phase with the majority (62.4 %) of the REE in the mineral phase.

Sample A2 showed that the clay was more enriched in ion-exchangeable REEs at 53.9 %, greater than the REE associated with the mineral phase (24.2 %). The amount of REE recovered from halloysite was 6.7 % in sample A1 compared with 19.7 % from sample A2. This indicates that the halloysite content is reduced in the pedolithic sample, which was expected from the weathering paths in Figure 2.17. Both samples have only a small fraction of REE in the organic phase with 1.4 % and 2.2 % respectively.



The TREE recovery using  $\text{NH}_4\text{Cl}$  for sample A1 was 44.3 %, 39.5 % for  $\text{NaCl}$  and 28.9 % for  $\text{MgCl}_2$ . The Mg ion performs poorly in the pedolithic sample, however it is more effective in sample A2 with a TREE recovery of 72.1 % compared to 72.2 % for Na. For sample A2 the best recovery was with  $\text{NH}_4\text{Cl}$  at 83.1 %. These results show that the best lixiviant was  $\text{NH}_4\text{Cl}$  followed by  $\text{NaCl}$  and  $\text{MgCl}_2$  respectively.

#### 4.2.2. Simulated Seawater

Seawater is a potential lixiviant in coastal regions, however sodium chloride was shown in section 4.2.1 to have low recovery and therefore ammonium sulphate is added to improve the overall recovery. The results from the addition of ammonium sulphate to simulated seawater (0.5 M  $\text{NaCl}$ ) is given in Figure 4.17.

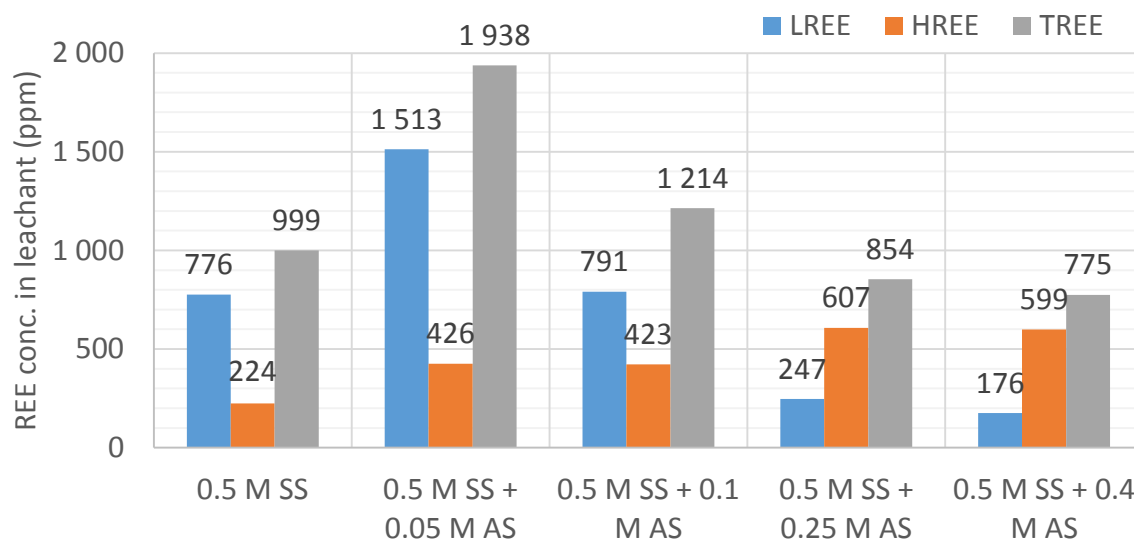


**Figure 4.17 Sample A2 REE concentration in simulated seawater (SS - 0.5 M  $\text{NaCl}$ ) lixiviant with increasing  $(\text{NH}_4)_2\text{SO}_4$  (AS) addition**

The results were given as REE concentration in the leachant because the whole rock analysis would significantly increase analysis costs. The first experiment with simulated seawater (0 M AS) gives a TREE concentration of 999 ppm compared to 2 432 ppm with 1 M  $\text{NaCl}$  in the first stage of experiment 1. The addition of 0.05 M ammonium sulphate improves concentration to 1 938 ppm, however further increases result in an overall decrease in TREE concentration. Interestingly the HREE concentration improves with the addition of ammonium sulphate until 0.25 M, but the LREE concentration falls sharply after 0.05 M. Spark *et al.* (1995) showed that leaching kaolinite with high ionic concentrations had adverse effects for lixiviant access to the

kaolinite surface due to lixiviant saturation. It has been shown that chlorine (Cl<sup>-</sup>) attracted to the gibbsite surface can help drive Na<sup>+</sup> adsorption on the octahedral site (Vasconcelos *et al.*, 2007), which would assist in HREE concentration in the leachant.

#### 4.2.3. Compound lixiviants

To investigate the effect of compound lixiviants, Mg<sup>2+</sup> is compared to NH<sub>4</sub><sup>+</sup> in a sulphate system and NO<sub>3</sub><sup>-</sup> is compared to SO<sub>4</sub><sup>2-</sup> in an ammonium system. The results from these experiments are shown in Figure 4.18 and 4.19 respectively.

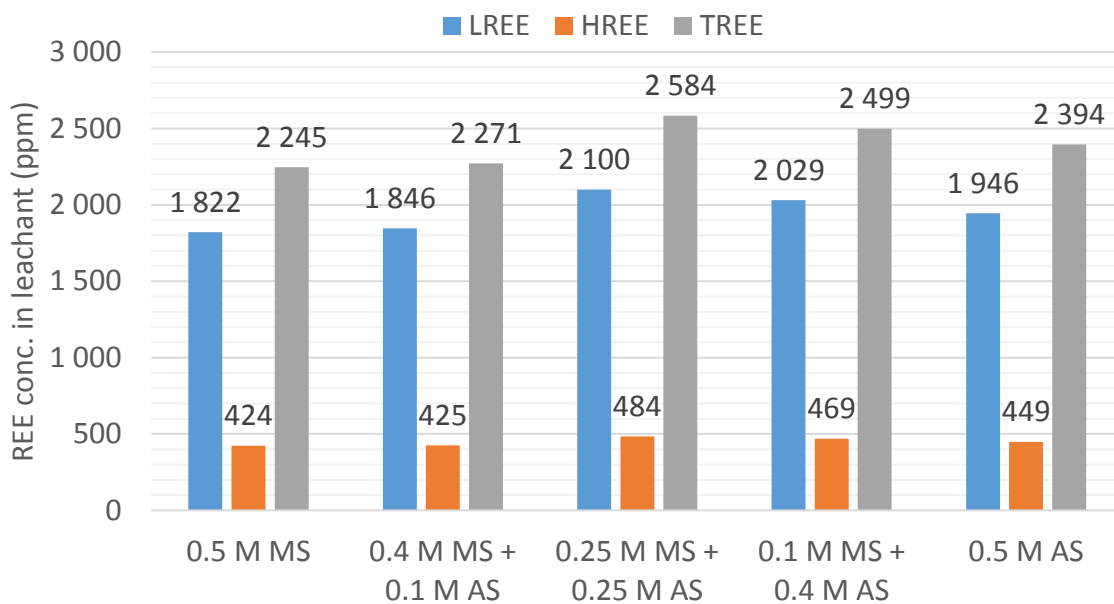


**Figure 4.18 Sample B REE concentration in leachant after addition of compound lixiviants MgSO<sub>4</sub> (MS) and (NH<sub>4</sub>)<sub>2</sub>SO<sub>4</sub> (AS)**

Figure 4.18 shows that the ammonium ion is superior in exchanging with the REEs compared to the Mg ion (2394 ppm compared to 2245 ppm TREE). The greatest concentration was 2584 ppm corresponding to an Mg<sup>2+</sup>:NH<sub>4</sub><sup>+</sup> ratio of 1:2 (equal charge ratio). This shows that the Mg ion can be beneficial to the leaching of REE, which would help to alleviate the Mg leaching problem as discussed in section 2.3.3 and correct the nutrient deficiency.

Figure 4.19 shows that ammonium sulphate (TREE 2394 ppm) is also superior to ammonium nitrate (TREE 2222 ppm) at leaching REE due to forming more stable REE sulphates. However compound leaching with a nitrate to sulphate ratio of 2:1 gives an improved TREE recovery of 2779 ppm while reducing the Al content to its lowest concentration of 151 ppm. This

improvement is due to the high permeability of the nitrate ion, as shown by Zhengyan *et al.* (2016).

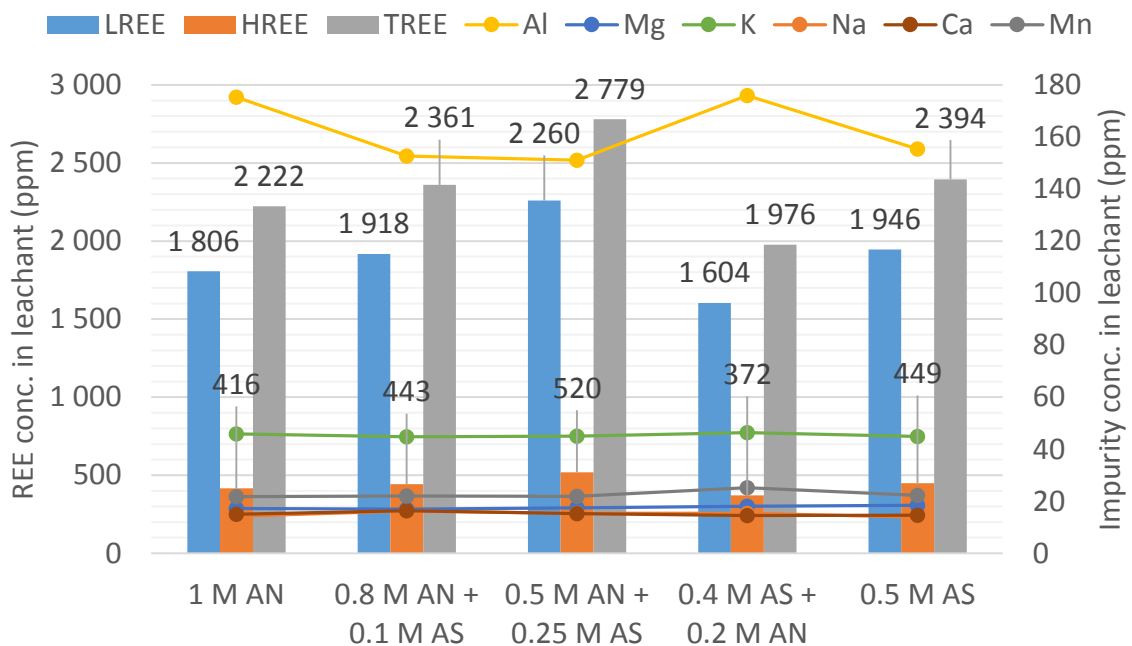


**Figure 4.19 Sample B REE concentration in leachant after addition of compound lixivants  $\text{NH}_4\text{NO}_3$  (AN) and  $(\text{NH}_4)_2\text{SO}_4$  (AS)**

The low K content is due to less K-feldspar in sample B (as shown with XRD) and the elevated Al impurities in sample B is due to Al rich kaolin. This is shown by the elevated  $\text{Al}_2\text{O}_3$  levels in Figure 4.3 and low gibbsite content shown in Table 4.1.

#### 4.2.4. Ionic strength

The results from the simulated seawater in Figure 4.17 show that the concentration of ammonium sulphate plays an important role in the recovery of REEs. Figure 4.20 shows the REE concentration in the leachant with increasing ionic strength of ammonium sulphate. At 0.05 M the concentration is low resulting in low ion-exchange with the REEs (TREE 1 247 ppm). This increases to a maximum TREE concentration of 3 555 ppm at 0.25 M ammonium sulphate. Increasing the sulphate concentration above 0.25 M results in a decrease in both LREE and HREE concentration.

The main impurity for sample F is K due to the large amount of K-feldspar in this sample. The second major impurity is Mn due to the presence of Mn minerals in all the samples. At the

lowest ionic strength (0.05 M) AS is the lowest impurity leached but as the ionic strength increases more Al was leached to become the second major impurity above Mn.

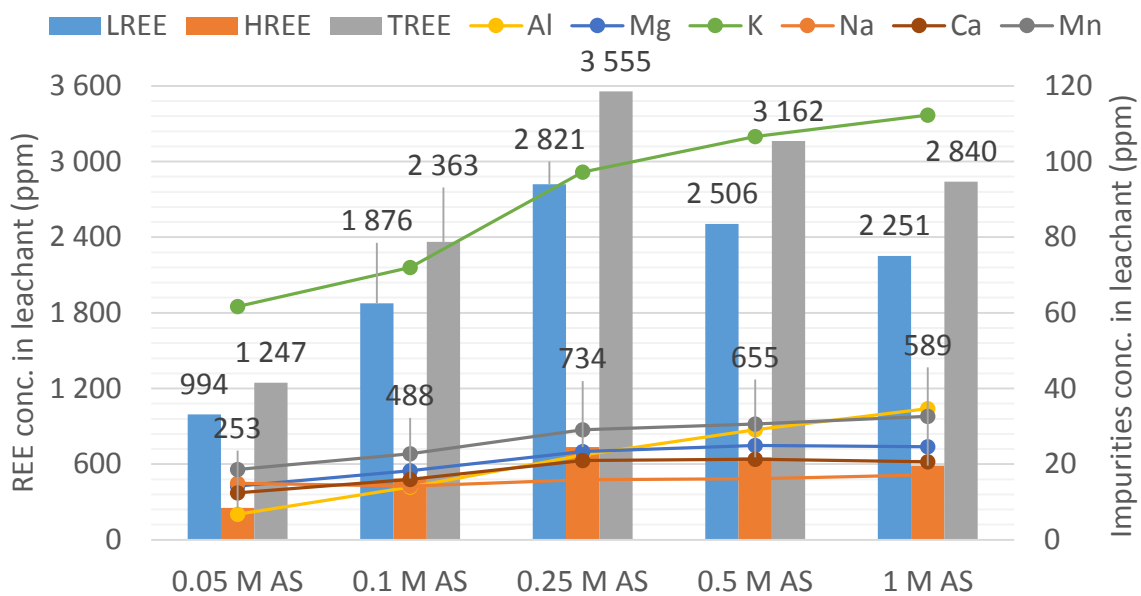


**Figure 4.20 Sample F REE and impurity concentration with increasing ionic strength of  $(\text{NH}_4)_2\text{SO}_4$  (AS)**

#### 4.2.5. Inhibitor addition

The effect of adding ammonium acetate as a buffer to inhibit the leaching of Al is shown in Figures 4.21 (sample A1) and 4.22 (sample F).

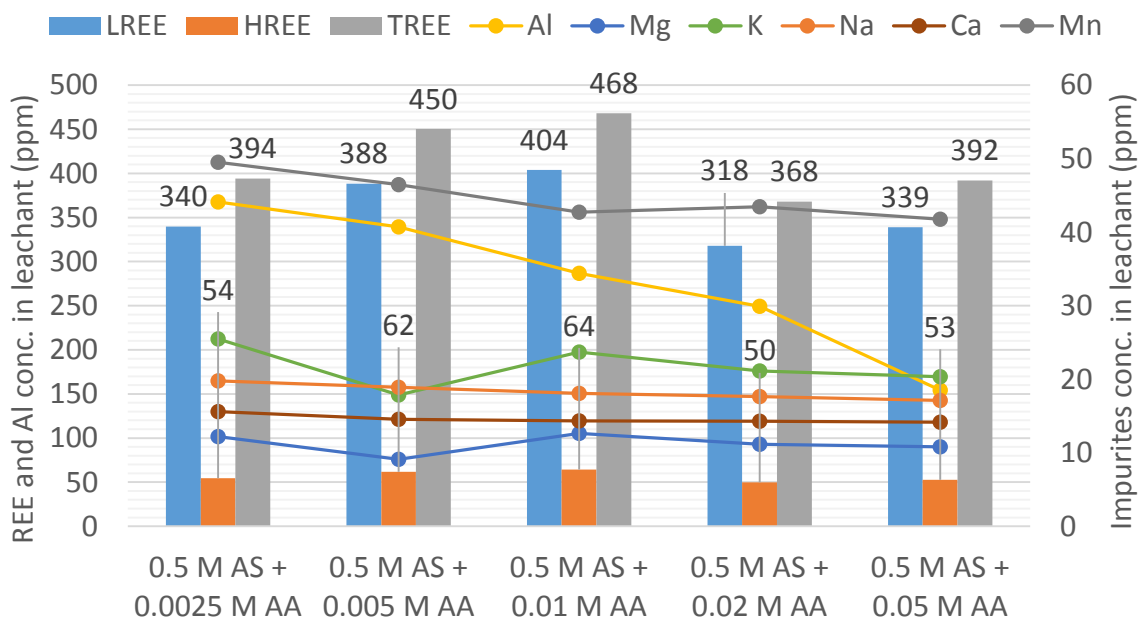


**Figure 4.21 Sample A1 REE and Al concentration (primary axis, other impurities on secondary axis) in 0.5 M  $(\text{NH}_4)_2\text{SO}_4$  (AS) with increasing  $\text{NH}_4\text{CH}_3\text{COO}$  (AA) inhibitor**

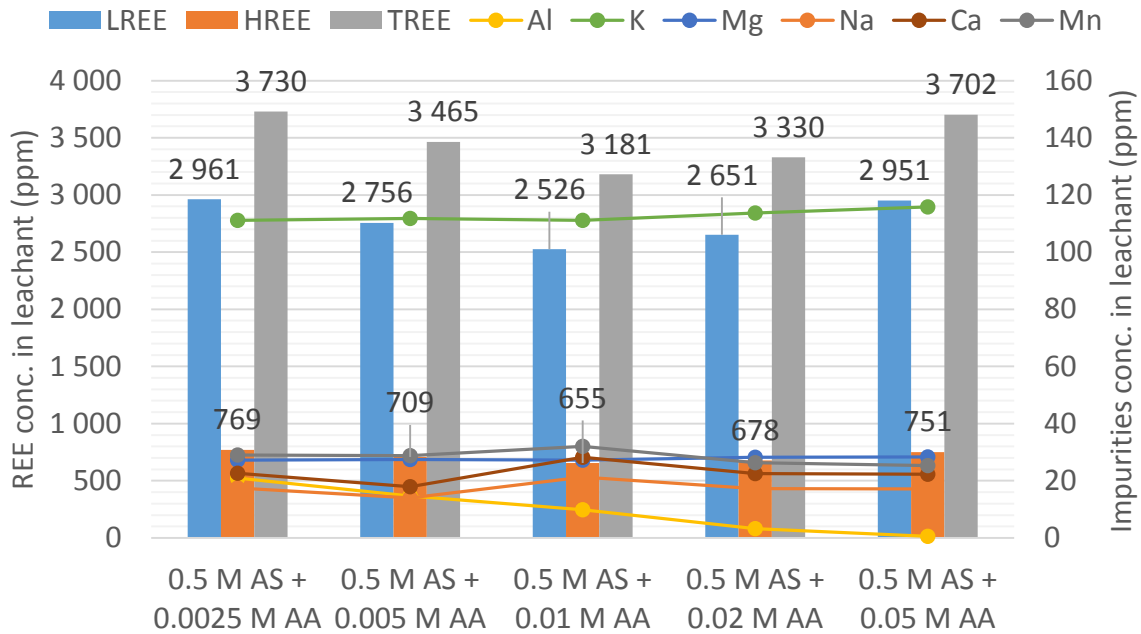


**Figure 4.22 Sample F REE concentration (primary axis, impurities on secondary axis) in 0.5 M (NH<sub>4</sub>)<sub>2</sub>SO<sub>4</sub> (AS) with increasing NH<sub>4</sub>CH<sub>3</sub>COO (AA) inhibitor**

Figure 4.21 (primary axis) shows that the Al concentration in the pedolithic sample A1 is larger than with the saprock sample F (Figure 4.22). Although sample F contains more gibbsite than sample A1 (XRD Table 4.1 Gibbsite 2.2 % in F compared to 1.6 % in A1), due to the more weathered nature of sample A1 it contains a higher proportion of Al rich kaolinite (XRF Figure 4.3 35.0 % Al<sub>2</sub>O<sub>3</sub> in A1 compared to 31.4 % Al<sub>2</sub>O<sub>3</sub> in sample F).

The addition of ammonium acetate from 0.0025 M to 0.05 M reduced the amount of Al leached from 368 ppm to 154 ppm in sample A1 and 21 ppm to 0.5 ppm in sample F. This is due to ammonium acetate acting as a buffering agent as discussed in section 2.3.3. There is no clear relationship between the addition of ammonium acetate and REE recovery in both Figure 4.21 and 4.22 as the background lixiviant is 0.5 M ammonium sulphate which was shown in Figure 4.20 to be too high.

## 5. CONCLUSION AND RECOMMENDATIONS

### 5.1. Sample Characterisation

The first objective for this study was to characterise the four clay samples (A1, A2, B and F) to determine their mineralogical characteristics. The pedolith sample (A1) varied significantly from the three saprock samples (A2, B and F). The texture of sample A1 (5 to 6.5 m) was homogenous, with the QEMSCAN results showing Fe minerals distributed through the kaolinite giving it a red appearance. The XRF and PSD results show that sample A1 is enriched in Fe (5.01 wt %) with a large amount (3.3 %) of particles in the 0.2  $\mu\text{m}$  size fraction due to poorly crystallised kaolinite and iron oxide minerals. The XRD results showed that the majority of the sample is kaolinite (74.9 %) with an appreciable amount of halloysite-7 $\text{\AA}$  (22.2 %). The  $\text{SiO}_2$  and  $\text{Al}_2\text{O}_3$  values are 42.1 % and 35.0 % respectively, the elevated Al content due to gibbsite (1.6 %). This sample showed poor crystallinity with a Hinckley index of 0.29 and high alteration index (99.1) due to the highly weathered nature of the sample where all of the primary material has been removed. The ICP-MS results showed that this sample is enriched in LREEs with a La / Gd ratio of 16.6. However the pedolith sample was depleted in REE (TREE = 1 503 ppm) compared with the saprock samples (TREE = 7 006 ppm on average).

The saprock samples A2, B and F are sampled from deeper in the regolith (6.5 to 10 m). They show a more heterogeneous texture due to the preservation of the primary texture. The QEMSCAN results showed that the white phases contain kaolin (kaolinite and halloysite) without impurities and that the red staining is due to Fe minerals. The white kaolin morphology was shown with SEM to be mainly platy kaolinite with some tubular structure. The amount of tubes suggests that the majority of halloysite-7 $\text{\AA}$  is platy due to dehydration of the sample. TEM imaging shows that there is no Fe substituted in the white kaolin structure and that the red phase has Fe oxides deposited on the surface of kaolinite with Fe substituted in the lattice.

The tawny phase was shown to contain gibbsite and that the kaolinite in this region had elevated Al levels. The black phase was shown by QEMSCAN to contain Mn minerals associated with kaolinite, K-feldspar and Fe minerals. The SEM results show that this phase is highly weathered and is responsible for PSD peak at 17.8  $\mu\text{m}$ . The QEMSCAN images show the relationship between the Mn minerals and scavenged Ce with the ICP-MS results confirming

that the black phase contains the majority of the Ce. The TREE content is depleted in the red phase due to Fe minerals competing with the REE for surface space on the kaolin particles.

The XRF, XRD and ICP-MS results indicate that sample A2 and F have similar mineralogies while sample B is similar to sample A1. Samples A2 and F both contain K-feldspar (9.2 % and 10.4 %) and gibbsite (0.55 % and 2.2 % respectively). Sample B showed greater weathering and only contained kaolin (80.9 % kaolinite and 18.9 % halloysite-7Å). This is confirmed from the PSD with an elevated peak at 2.2 µm and higher alteration index of 98.1. All four samples have a negative Ce, Eu and Tm anomaly. The saprock samples show LREE and HREE enrichment relative to the pedolith with samples A2 and F having La / Gd ratio of 17.4 and Gd / Lu ratio of 1.2. The more crystalline samples A2 and F (Hinckley index 0.40 and 0.44 respectively) are more REE enriched than the more weathered sample B (Hinckley index 0.32).

It is recommended that more saprock samples are characterised using the techniques in this study as they show HREE enrichment. These samples should be kept hydrated from the time of sampling to get a more accurate estimate for halloysite content using XRD. The effect of Mn minerals needs to be investigated in relation to kaolinite formation.

## 5.2. Batch leach tests

The second objective of this study was to geochemically characterise the samples to determine REE association with the mineral assemblage. Sample A1 showed decreasing REE recovery contributed from kaolinite from LREE to HREE whereas sample A2 showed consistent recovery across the REEs from kaolinite. Both samples show little Ce recovery from kaolinite due to Mn minerals scavenging Ce. The best lixiviant recovery was seen with  $\text{NH}_4^+$  followed by  $\text{Na}^+$  and  $\text{Mg}^{2+}$  in a chloride system. For sample A1 the recovery from the kaolinite fraction was 37.7 %, halloysite 5.1 %, organic 1.6 % and mineral 55.7 %. The proportion of ion-exchangeable REE is increased in sample A2 showing a recovery from the kaolinite fraction of 66.9 %, halloysite 12.7 %, organic 3.5 % and mineral 16.9 %.

The third objective was to determine the optimum leaching conditions. The results from the simulated seawater experiments indicate that some addition of ammonium sulphate is beneficial as the addition of 0.05 M ammonium sulphate almost doubled the concentration of REE in the leachate. The excess addition of ammonium sulphate above 0.05 M had adverse effects on the leachate concentration of LREEs but not for the HREEs. This is due to blocking

lixiviant access to the kaolinite surface as the lixiviant becomes saturated however the presence of  $\text{Cl}^-$  allows for the leaching of HREEs.

It was concluded from the compound leaching experiments that  $\text{Mg}^{2+}$  can be used to supplement  $\text{NH}_4^+$  with the greatest REE concentration in the leachate using a  $\text{Mg}^{2+}:\text{NH}_4^+$  ratio of 1:2 (equal charge). This ratio would assist in increasing the REE concentration in the leachate while keeping Mg available for plants. Compound leaching with the nitrate ion shows that the greatest REE concentration in the leachate is with a  $\text{NO}_3^-:\text{SO}_4^{2-}$  ratio of 2:1 (equal charge).

The results from increasing the ionic strength of ammonium sulphate shows that increasing the concentration above 0.25 M reduces the REE concentration in the leachate due to impeding lixiviant access. The results from the addition of ammonium acetate as a buffer showed that the buffer inhibited the leaching of Al in both samples A1 and F, with the greatest inhibition at 0.05 M. These experiments were conducted at 0.5 M ammonium sulphate concentration, therefore it is recommend that these experiments are repeated at the lower concentration of 0.25 M to avoid lixiviant saturation.



## REFERENCES

- AIDE, M. T. & AIDE, C. 2012. Rare earth elements: their importance in understanding soil genesis. *ISRN Soil Science*, 2012.
- AJA, S. U. 1998. The Sorption of the Rare Earth Element, Nd, onto Kaolinite at 25 degrees C. *Clays and Clay Minerals*, 46, 103-109.
- ALDERTON, D., PEARCE, J. A. & POTTS, P. 1980. Rare earth element mobility during granite alteration: evidence from southwest England. *Earth and Planetary Science Letters*, 49, 149-165.
- ALLABY, M. 2008. A Dictionary of Earth Sciences: Oxford University Press. *New York*.
- ALONSO, E., SHERMAN, A. M., WALLINGTON, T. J., EVERSON, M. P., FIELD, F. R., ROTH, R. & KIRCHAIN, R. E. 2012. Evaluating rare earth element availability: a case with revolutionary demand from clean technologies. *Environ Sci Technol*, 46, 3406-3414.
- ANDERSEN, J. C., ROLLINSON, G. K., SNOOK, B., HERRINGTON, R. & FAIRHURST, R. J. 2009. Use of QEMSCAN® for the characterization of Ni-rich and Ni-poor goethite in laterite ores. *Minerals Engineering*, 22, 1119-1129.
- BALASHOV, Y. A., RONO, A., MIGDISOV, A. & NV, T. 1964. Effect of climate and facies environment on fractionation of rare earths during sedimentation. *Geochemistry International USSR*, 951-969.
- BAO, Z. & ZHAO, Z. 2008. Geochemistry of mineralization with exchangeable REY in the weathering crusts of granitic rocks in South China. *Ore Geology Reviews*, 33, 519-535.
- BERTOLINO, L. C., ROSSI, A. M., SCORZELLI, R. B. & TOREM, M. L. 2010. Influence of iron on kaolin whiteness: An electron paramagnetic resonance study. *Applied Clay Science*, 49, 170-175.
- BINNEMANS, K., JONES, P. T., BLANPAIN, B., VAN GERVEN, T., YANG, Y., WALTON, A. & BUCHERT, M. 2013. Recycling of rare earths: a critical review. *Journal of Cleaner Production*, 51, 1-22.
- BONIFICIO, W. D. & CLARKE, D. R. 2016. Rare-earth separation using bacteria. *Environmental Science & Technology Letters*, 3, 180-184.
- CASTOR, S. B. & HEDRICK, J. B. 2006. Rare earth elements. *Industrial minerals volume, 7th edition: Society for mining, metallurgy, and exploration, Littleton, Colorado*, 769-792.

- CHAKHMOURADIAN, A. R. & WALL, F. 2012. Rare earth elements: minerals, mines, magnets (and more). *Elements*, 8, 333-340.
- CHEN, P.-Y., LIN, M.-L. & ZHENG, Z. 1997. On the origin of the name kaolin and the kaolin deposits of the Kauling and Dazhou areas, Kiangsi, China. *Applied Clay Science*, 12, 1-25.
- CHURCHMAN, G. 1990. Relevance of different intercalation tests for distinguishing halloysite from kaolinite in soils. *Clays and Clay Minerals*, 38, 591-599.
- CHURCHMAN, G., ALDRIDGE, L. & CARR, R. 1972. The relationship between the hydrated and dehydrated states of an halloysite. *Clays and Clay Minerals*, 20, 241-246.
- CHURCHMAN, G. & GILKES, R. 1989. Recognition of intermediates in the possible transformation of halloysite to kaolinite in weathering profiles. *Clay Minerals*, 24, 579-590.
- CHURCHMAN, G. & THENG, B. 1984. Interactions of halloysites with amides: mineralogical factors affecting complex formation. *Clay Minerals*, 19, 161-175.
- CHURCHMAN, G. J. 2010. Is the geological concept of clay minerals appropriate for soil science? A literature-based and philosophical analysis. *Physics and Chemistry of the Earth, Parts A/B/C*, 35, 927-940.
- CHURCHMAN, G. J. & LOWE, D. J. 2012. *Alteration, formation, and occurrence of minerals in soils*, CRC press.
- COTTON, S. 2006. Introduction to the Lanthanides. *Lanthanide and Actinide Chemistry*, 1-7.
- DE VILLIERS, J. 2016. *X-ray diffraction in Mineralogy*. In: Becker M, Wightman EM, Evans CL (eds) *Process Mineralogy: JKMRC Monograph Series in Mining and Minerals Processing*, No 6. Julius Kruttschnitt Mineral Research Centre, Brisbane, Australia, pp 67-78.
- DESHARNAIS, G., CAMUS, Y. & BISAILLON, C. 2014. NI 43-101 Technical Report Resources for the Tantalus Rare Earth Ionic Clay Project Northern Madagascar. Submitted to Tantalus Rare Earth AG: SGS Canada Inc.
- DOE, U. S. 2011. *Critical Materials Strategy* [Online]. Office of Policy. Available: [http://energy.gov/sites/prod/files/DOE\\_CMS2011\\_FINAL\\_Full.pdf](http://energy.gov/sites/prod/files/DOE_CMS2011_FINAL_Full.pdf) [Accessed 29/11/2018].

- DUDDY, L. R. 1980. Redistribution and fractionation of rare-earth and other elements in a weathering profile. *Chemical Geology*, 30, 363-381.
- EARLE, S. 2015. *Silicate Minerals* [Online]. Available: <https://opentextbc.ca/geology/chapter/2-4-silicate-minerals/> [Accessed 04 February 2018].
- ESTRADE, G., SALVI, S., BÉZIAT, D., RAKOTOVAO, S. & RAKOTONDRAZAFY, R. 2014. REE and HFSE mineralization in peralkaline granites of the Ambohimirahavavy alkaline complex, Ampasindava peninsula, Madagascar. *Journal of African Earth Sciences*, 94, 141-155.
- FRITZ, S. J. 1988. A comparative study of gabbro and granite weathering. *Chemical Geology*, 68, 275-290.
- GANZEEV, A. & GRECHISHCHEV, O. 2003. A new genetic type of rare-metal alkali granites of Madagascar. *GEOLOGIYA I GEOFIZIKA*, 44, 539-553.
- GHORBANI, Y., FRANZIDIS, J.-P. & PETERSEN, J. 2016. Heap leaching technology—current state, innovations and future directions: A review. *Mineral Processing and Extractive Metallurgy Review*, 37, 73-119.
- GILKES, R. J. & PRAKONGKEP, N. 2016. How the unique properties of soil kaolin affect the fertility of tropical soils. *Applied Clay Science*, 131, 100-106.
- GOLEV, A., SCOTT, M., ERSKINE, P. D., ALI, S. H. & BALLANTYNE, G. R. 2014. Rare earths supply chains: Current status, constraints and opportunities. *Resources Policy*, 41, 52-59.
- GRIM, R. E. 1962. Applied clay mineralogy. *GFF*, 84, 533-533.
- GUTFLEISCH, O. 2000. Controlling the properties of high energy density permanent magnetic materials by different processing routes. *Journal of Physics D: Applied Physics*, 33, R157.
- HART, R., ST PIERRE, T., GILKES, A., MCKINLEY, A., SIRADZ, S. & SINGH, B. 2002. Iron in soil kaolins from Indonesia and Western Australia. *Clay Minerals*, 37, 671-685.
- HASENMUELLER, E. A., GU, X., WEITZMAN, J. N., ADAMS, T. S., STINCHCOMB, G. E., EISSENSTAT, D. M., DROHAN, P. J., BRANTLEY, S. L. & KAYE, J. P. 2017. Weathering of rock to regolith: The activity of deep roots in bedrock fractures. *Geoderma*, 300, 11-31.

- HE, Y. 2014. Reregulation of China's rare earth production and export. *International Journal of Emerging Markets*, 9, 236-256.
- HELMENSTINE, T. 2017. *Science Notes* [Online]. Available: <http://sciencenotes.org/downloadable-periodic-table-circle-tiles-2015/> [Accessed 13 January 2017].
- HENDERSON, P. 1984. General geochemical properties and abundances of the rare earth elements. *Rare earth element geochemistry*, 2, 1-32.
- HILL, R. & HOWARD, C. 1987. Quantitative phase analysis from neutron powder diffraction data using the Rietveld method. *Journal of Applied Crystallography*, 20, 467-474.
- HINCKLEY, D. N. 1962. Variability in crystallinity values among the kaolin deposits of the coastal plain of Georgia and South Carolina. *Clays and clay minerals*, 11, 229-235.
- HU, Z., RICHTER, H., SPAROVEK, G. & SCHNUG, E. 2004. Physiological and biochemical effects of rare earth elements on plants and their agricultural significance: a review. *Journal of plant nutrition*, 27, 183-220.
- HUGHES, J. C., GILKES, R. J. & HART, R. D. 2009. Intercalation of reference and soil kaolins in relation to physico-chemical and structural properties. *Applied Clay Science*, 45, 24-35.
- JHA, M. K., KUMARI, A., PANDA, R., KUMAR, J. R., YOO, K. & LEE, J. Y. 2016. Review on hydrometallurgical recovery of rare earth metals. *Hydrometallurgy*, 165, 2-26.
- JOHN, L. 2011. The Art of Heap Leaching-The Fundamentals. *Percolation Leaching: The status globally and in Southern Africa. Misty Hills: The Southern African Institute of Mining and Metallurgy (SAIMM)*, 17-42.
- JOHNSTON, C. T. 2010. Probing the nanoscale architecture of clay minerals. *Clay Minerals*, 45, 245-279.
- JORDENS, A. 2015. The beneficiation of rare earth element-bearing minerals. *Department of Mining and Materials Engineering*, McGill University, Montreal, Canada, 1-203.
- JOUSSEIN, E., PETIT, S., CHURCHMAN, J., THENG, B., RIGHI, D. & DELVAUX, B. 2005. Halloysite clay minerals—a review. *Clay Minerals*, 40, 383-426.
- JOUSSEIN, E., PETIT, S. & DELVAUX, B. 2007. Behaviour of halloysite clay under formamide treatment. *Applied Clay Science*, 35, 17-24.

- KIM, J.-A., DODDIBA, G., TANIMURA, Y., MITSUHASHI, K., FUKUDA, N., OKAYA, K., MATSUO, S. & FUJITA, T. 2011. Leaching of rare-earth elements and their adsorption by using blue-green algae. *Materials transactions*, 52, 1799-1806.
- KRISHNAMURTHY, N. & GUPTA, C. K. 2004. Extractive metallurgy of rare earths. Boca Raton, CRC press, 1-56.
- KYNICKY, J., SMITH, M. P. & XU, C. 2012. Diversity of Rare Earth Deposits: The Key Example of China. *Elements*, 8, 361-367.
- LUO, J. 2012. *Cartoon* [Online]. China Daily. Available: [http://usa.chinadaily.com.cn/opinion/2012-03/16/content\\_14847478.htm](http://usa.chinadaily.com.cn/opinion/2012-03/16/content_14847478.htm) [Accessed 05 February 2017].
- LUO, X.-P., FENG, B., WANG, P.-C., ZHOU, H.-P. & CHEN, X.-M. 2015. The effect of fulvic acid on the leaching of a weathered rare-earth ore. *Metallurgical and Materials Transactions B*, 46, 2405-2407.
- MCDONOUGH, W. F. & SUN, S. 1995. The composition of the Earth. *Chemical Geology*, 120, 223-253.
- MCGILL, I. 2000. Rare earth elements. *Ullmann's encyclopedia of industrial chemistry*, 1-228.
- MIGDISOV, A., WILLIAMS-JONES, A., BRUGGER, J. & CAPORUSCIO, F. A. 2016. Hydrothermal transport, deposition, and fractionation of the REE: Experimental data and thermodynamic calculations. *Chemical Geology*, 439, 13-42.
- MOLDOVEANU, G. A. & PAPANGELAKIS, V. G. 2012. Recovery of rare earth elements adsorbed on clay minerals: I. Desorption mechanism. *Hydrometallurgy*, 117, 71-78.
- MOLDOVEANU, G. A. & PAPANGELAKIS, V. G. 2016. An overview of rare-earth recovery by ion-exchange leaching from ion-adsorption clays of various origins. *Mineralogical Magazine*, 80, 63-76.
- MÖLLER, P. & GIESE, U. 1997. Determination of easily accessible metal fractions in rocks by batch leaching with acid cation-exchange resin. *Chemical geology*, 137, 41-55.
- MURRAY, H. 1999. Applied clay mineralogy today and tomorrow. *Clay minerals*, 34, 39-39.
- NAVARRO, J. & ZHAO, F. 2014. Life-cycle assessment of the production of rare-earth elements for energy applications: a review. *Frontiers in Energy Research*, 2, 45.

- NESBITT, H. W. & MARKOVICS, G. 1997. Weathering of granodioritic crust, long-term storage of elements in weathering profiles, and petrogenesis of siliciclastic sediments. *Geochimica et Cosmochimica Acta*, 61, 1653-1670.
- NORRISH, K. & HUTTON, J. T. 1969. An accurate X-ray spectrographic method for the analysis of a wide range of geological samples. *Geochimica et cosmochimica acta*, 33, 431-453.
- OHTA, A. & KAWABE, I. 2001. REE (III) adsorption onto Mn dioxide ( $\delta$ -MnO<sub>2</sub>) and Fe oxyhydroxide: Ce (III) oxidation by  $\delta$ -MnO<sub>2</sub>. *Geochimica et Cosmochimica Acta*, 65, 695-703.
- OZAKI, T., SUZUKI, Y., NANKAWA, T., YOSHIDA, T., OHNUKI, T., KIMURA, T. & FRANCIS, A. J. 2006. Interactions of rare earth elements with bacteria and organic ligands. *Journal of alloys and compounds*, 408, 1334-1338.
- PANG, X., LI, D. & PENG, A. 2002. Application of rare-earth elements in the agriculture of China and its environmental behaviour in soil. *Environmental Science and Pollution Research*, 9, 143.
- PAPANGELAKIS, V. G. & MOLDOVEANU, G. Recovery of rare earth elements from clay minerals. ERES2014: 1st European Rare Earth Resources Conference, Milos Greece, 2014. 91-202.
- PARKER, A. & RAE, J. E. 1998. *Environmental Interactions of Clays: Clays and the Environment*, Springer Science & Business Media.
- PEELMAN, S., SUN, Z. H., SIETSMA, J. & YANG, Y. 2015. Leaching of rare earth elements: review of past and present technologies. *Rare Earths Industry*, 319-334.
- PENCHOFF, D. 2013. *United States Geographical Survey RE Usage* [Online]. Available: <http://www.jics.utk.edu/penchoff-question-and-answer> [Accessed 05 February 2017].
- PIASECKI, W. & SVERJENSKY, D. A. 2008. Speciation of adsorbed yttrium and rare earth elements on oxide surfaces. *Geochimica et Cosmochimica Acta*, 72, 3964-3979.
- PLANÇON, A., GIESE, R. & SNYDER, R. 1988. HINCKLEY INDEX FOR KAOLINITES. *Clays and Clay Minerals*, 23, 249-260.
- POURRET, O., DAVRANCHE, M., GRUAU, G. & DIA, A. 2007. Rare earth elements complexation with humic acid. *Chemical Geology*, 243, 128-141.
- ROBB, L. 2005. *Introduction to Ore-Forming Processes*, Malden, Blackwell Science Ltd, 1-368.

- ROCHA, A., SCHISSEL, D., SPRECHER, A., DE TARSO, P. & GOODE, J. Process development for the Serra Verde weathered crust elution-deposited rare earth deposit in Brazil. Proceedings of the 52rd Conference of Metallurgists (COM 2013), 2013.
- ROZELLE, P. L., KHADILKAR, A. B., PULATI, N., SOUNDARRAJAN, N., KLIMA, M. S., MOSSER, M. M., MILLER, C. E. & PISUPATI, S. V. 2016. A Study on Removal of Rare Earth Elements from US Coal By products by Ion Exchange. *Metallurgical and Materials Transactions E*, 1-12.
- RUDNICK, R. L. & FOUNTAIN, D. M. 1995. Nature and composition of the continental crust: a lower crustal perspective. *Reviews of geophysics*, 33, 267-309.
- SANEMATSU, K. & KON, Y. 2013. Geochemical characteristics determined by multiple extraction from ion-adsorption type REE ores. *Bulletin of the Geological Survey of Japan*, 64, 313-330.
- SANTORO, L., ROLLINSON, G., BONI, M. & MONDILLO, N. 2015. Automated scanning electron microscopy (Qemscan<sup>®</sup>)-based mineral identification and quantification of the Jabali Zn-Pb-ag nonsulfide deposit (Yemen). *Economic Geology*, 110, 1083-1099.
- SAWKA, W. N. & CHAPPELL, B. W. 1988. Fractionation of uranium, thorium and rare earth elements in a vertically zoned granodiorite: Implications for heat production distributions in the Sierra Nevada batholith, California, USA. *Geochimica et Cosmochimica acta*, 52, 1131-1143.
- SEREDIN, V. V. & DAI, S. 2012. Coal deposits as potential alternative sources for lanthanides and yttrium. *International Journal of Coal Geology*, 94, 67-93.
- SINGH, B. 1991. *Mineralogical and chemical characteristics of soils from south-western Australia*. Doctoral dissertation, Soil Science and Plant Nutrition, University of Western Australia, 1-231.
- SINGH, B. 1996. Why Does Halloysite Roll?--A New Model. *Clays and Clay Minerals*, 44, 191-196.
- SINGH, B. & MACKINNON, I. D. 1996. Experimental transformation of kaolinite to halloysite. *Clays and Clay Minerals*, 44, 825-834.
- SPARK, K., WELLS, J. & JOHNSON, B. 1995. Characterizing trace metal adsorption on kaolinite. *European Journal of Soil Science*, 46, 633-640.

- TAKAHASHI, Y., CHÂTELLIER, X., HATTORI, K. H., KATO, K. & FORTIN, D. 2005. Adsorption of rare earth elements onto bacterial cell walls and its implication for REE sorption onto natural microbial mats. *Chemical Geology*, 219, 53-67.
- TAWORNPRUEK, S., KHEORUENROMNE, I., SUDDHIPRAKARN, A. & GILKES, R. 2006. Properties of red Oxisols on calcareous sedimentary rocks in Thailand. *Geoderma*, 136, 477-493.
- TEPPEN, B. J. & MILLER, D. M. 2006. Hydration energy determines isovalent cation exchange selectivity by clay minerals. *Soil Science Society of America Journal*, 70, 31-40.
- THENG, B., CHURCHMAN, G., WHITTON, J. & CLARIDGE, G. 1984. Comparison of intercalation methods for differentiating halloysite from kaolinite. *Clays and Clay Minerals*, 32, 249.
- TIAN, J., TANG, X., YIN, J., CHEN, J., LUO, X. & RAO, G. 2013b. Enhanced Leachability of a Lean Weathered Crust Elution-Deposited Rare-Earth Ore: Effects of Sesbania Gum Filter-Aid Reagent. *Metallurgical and Materials Transactions B*, 44, 1070-1077.
- TIAN, J., TANG, X., YIN, J., LUO, X., RAO, G. & JIANG, M. 2013a. Process optimization on leaching of a lean weathered crust elution-deposited rare earth ores. *International Journal of Mineral Processing*, 119, 83-88.
- TOMBÁČZ, E. & SZEKERES, M. 2006. Surface charge heterogeneity of kaolinite in aqueous suspension in comparison with montmorillonite. *Applied Clay Science*, 34, 105-124.
- USGS. 2002. *Rare Earth Elements—Critical Resources for High Technology* [Online]. US Geological Survey. Available: <https://pubs.usgs.gov/fs/2002/fs087-02> [Accessed 05 February 2017].
- VAHIDI, E., NAVARRO, J. & ZHAO, F. 2016. An initial life cycle assessment of rare earth oxides production from ion-adsorption clays. *Resources, Conservation and Recycling*, 113, 1-11.
- VASCONCELOS, I. F., BUNKER, B. A. & CYGAN, R. T. 2007. Molecular dynamics modelling of ion adsorption to the basal surfaces of kaolinite. *The Journal of Physical Chemistry C*, 111, 6753-6762.
- VOßENHAUL, D., STOLTZ, N., MEYER, F. & FRIEDRICH, B. Extraction of Rare Earth Elements from non-Chinese Ion Adsorption Clays. European Metallurgical Conference, 2015. 703.
- WADA, K. 1961. Lattice expansion of kaolin minerals by treatment with potassium acetate. *Am. Miner.*, 46, 78-91.



- WANG, W. 1995. Study on aluminium forms in some acid soils in South China. *Soil and Environmental Sciences*, 1, 1-8.
- WEBMINERAL.COM. 2017. *General Kaolinite Information* [Online]. Available: <http://webmineral.com/data/Kaolinite.shtml#.WnhHOHyYN1s> [Accessed 05 February 2017].
- WENG, Z., JOWITT, S. M., MUDD, G. M. & HAQUE, N. 2015. A detailed assessment of global rare earth element resources: opportunities and challenges. *Economic Geology*, 110, 1925-1952.
- WILLIAMS-JONES, A. E., MIGDISOV, A. A. & SAMSON, I. M. 2012. Hydrothermal mobilisation of the rare earth elements—a tale of “ceria” and “yttria”. *Elements*, 8, 355-360.
- WILSON, M. A., BURT, R., LYNN, W. C. & KLAMETH, L. C. 1997. Total elemental analysis digestion method evaluation on soils and clays. *Communications in Soil Science and Plant Analysis*, 28, 407-426.
- WOOD, S. 1996. The role of humic substances in the transport and fixation of metals of economic interest (Au, Pt, Pd, U, V). *Ore Geology Reviews*, 11, 1-31.
- WU, C., YUAN, Z. & BAI, G. 1995. Rare earth deposits in China. *Mineralogical Society Series*, 7, 281-310.
- WÜBBEKE, J. 2013. Rare earth elements in China: Policies and narratives of reinventing an industry. *Resources Policy*, 38, 384-394.
- YANFEI, X., LIU, X., FENG, Z., HUANG, X., HUANG, L., CHEN, Y. & WU, W. 2015a. Role of minerals properties on leaching process of weathered crust elution-deposited rare earth ore. *Journal of Rare Earths*, 33, 545-552.
- YANFEI, X., ZONGYU, F., XIAOWEI, H., LI, H., YINGYING, C., LIANGSHI, W. & ZHIQI, L. 2015b. Recovery of rare earths from weathered crust elution-deposited rare earth ore without ammonia-nitrogen pollution: I. leaching with magnesium sulphate. *Hydrometallurgy*, 153, 58-65.
- YANFEI, X., ZONGYU, F., XIAOWEI, H., LI, H., YINGYING, C., XIANGSHENG, L., LIANGSHI, W. & ZHIQI, L. 2016. Recovery of rare earth from the ion-adsorption type rare earths ore: II. Compound leaching. *Hydrometallurgy*, 163, 83-90.
- YANG, X. & ZHANG, J. 2015. Recovery of rare earth from ion-adsorption rare earth ores with a compound lixiviant. *Separation and Purification Technology*, 142, 203-208.

- YANG, X. J., LIN, A., LI, X.-L., WU, Y., ZHOU, W. & CHEN, Z. 2013. China's ion-adsorption rare earth resources, mining consequences and preservation. *Environmental Development*, 8, 131-136.
- ZHANG, D., ZHOU, C.-H., LIN, C.-X., TONG, D.-S. & YU, W.-H. 2010. Synthesis of clay minerals. *Applied Clay Science*, 50, 1-11.
- ZHANG, J. & EDWARDS, C. 2013. Mineral decomposition and leaching processes for treating rare earth ore concentrates. *Canadian Metallurgical Quarterly*, 52, 243-248.
- ZHANG, W., REZAEI, M., BHAGAVATULA, A., LI, Y., GROppo, J. & HONAKER, R. 2015. A Review of the Occurrence and Promising Recovery Methods of Rare Earth Elements from Coal and Coal By-Products. *International Journal of Coal Preparation and Utilization*, 35, 295-330.
- ZHENGYAN, H., ZHANG, Z., JUNXIA, Y. & ZHIGAO, X. 2016. Process optimization of rare earth and aluminium leaching from weathered crust elution-deposited rare earth ore with compound ammonium salts. *Journal of Rare Earths*, 34, 413-419.
- ZHI LI, L. & YANG, X. 2014. China's Rare Earth Ore Deposits and Beneficiation Techniques. *1st European Rare Earth Resources Conference*.
- ZHOU, B., LI, Z., ZHAO, Y., ZHANG, C. & WEI, Y. 2016. Rare Earth Elements supply vs. clean energy technologies: new problems to be solve. *Gospodarka Surowcami Mineralnymi*, 32, 29-44.
- ZHOU, C. H. & KEELING, J. 2013. Fundamental and applied research on clay minerals: From climate and environment to nanotechnology. *Applied Clay Science*, 74, 3-9.

## 6. APPENDICES

### 6.1. Introduction

#### 6.1.1. Rare Earth Elements and their uses

**Table 6.1 Rare Earth Elements and their uses**

	Elements		Usages				
			Catalyst	Glass Polish	Magnets	lasers	Other
Light REE	La	57	✓	✓			H <sub>2</sub> storage, batteries, camera lenses, flint
	Ce	58	✓	✓			ceramics
	Pr	59		✓	✓	✓	ceramics, lighting, flint
	Nd	60		✓	✓	✓	ceramic capacitors
	Sm	62	Phosphors		✓	✓	neutron capture, masers
	Eu	63	✓ (Red and Blue)			✓	mercury-vapour lamps
Heavy REE	Gd	64		✓	✓	✓	X-ray tubes, computer memory, neutron capture
	Tb	65	✓(Green)			✓	fluorescent lamps
	Dy	66			✓	✓	
	Ho	67				✓	
	Er	68				✓	vanadium steel
	Tm	69					portable X-ray machines
	Yb	70				✓(Infrared)	reducing agent
	Lu	71		✓			PET Scan detectors
	Y	39				✓	superconductors, microwave filters

#### 6.1.2. Locations of major REE reserves

Figure 1.6 Legend (McGill, 2012) 1) Malaysia; 2) Singkep, Billit and Bangka, Indonesia; 3) Taiwan; 4) Korea; 5) Western Australia; 6) Mary Kathleen Mine, Australia; 7) Radium Hill, Australia; 8) New South Wales, Australia; 9) Bear Valley, Idaho/Montana; 10) Mountain Pass,

California; 11) Music Valley, California; 12) Mineral Hill/Lenhi Pass, Idaho/Montana; 13) Bald Mountain, Wyoming; 14) Powderhorn and Wet Mountains, Colorado; 15) Gallinas Mountains, New Mexico; 16) Blind River/Elliot Lake, Ontario; 17) Piedmont, Georgia; 18) Atlantic Coast placer deposits; 19) Dover, New Jersey; 20) Oka, Quebec; 21) Mineville, New York; 22) Llallagua, Bolivia; 23) Atlánida, Uruguay; 24) Araxa, Brazil; 25) Morro do Ferro, Brazil; 26) Espirito Santo, Brazil; 27) Jos Plateau, Nigeria; 28) Steenkampskraal, Republic of South Africa; 29) Glenover, Republic of South Africa; 30) Shinkolobwe, Zaire; 31) Karonge, Burundi; 32) Panda Hill, Tanzania; 33) Kangakunde Hill, Malawi; 34) Nile Delta, Egypt; 35) Mrima, Kenya; 36) Kola Peninsula, CIS; 37) Madagascar; 38) Vishnevye Mountains, CIS; 39) Kerala, India; 40) Sri Lanka; 41) Bihar and Bengal; 42) Itremo, Madagascar; 43) Pilanesberg, Boputhatswana; 44) Wigu Hill, Tanzania; 45) Bon Nage Mauretania; 46) Monrovia, Liberia; 47) Fen, Norway; 48) Kangasala, Finland; 49) Bayan Obo, Inner Mongolia; 50) Roxby Downs, Australia

## 6.2. Methodology

### 6.2.1. Reagents

**Table 6.2 Section 3.1.3 Reagents**

Description		Mr (g/mol)	Main Hazard
Sodium Chloride fine 'AR'	NaCl	58.44	N/A
Sodium Acetate trihydrate 'AR'	NaCH <sub>3</sub> COO.3H <sub>2</sub> O	136.08	Irritant
Tetra-Sodium Pyrophosphate anhydrous 'AR'	Na <sub>4</sub> PO <sub>3</sub> OPO <sub>3</sub>	256.9	Irritant
Potassium Acetate anhydrous 'AR'	KCH <sub>3</sub> COO	98.15	Irritant
Ammonium Chloride fine crystals 'AR'	NH <sub>4</sub> Cl	53.49	Irritant
Ammonium Sulphate 'AR'	(NH <sub>4</sub> ) <sub>2</sub> SO <sub>4</sub>	132.14	Environmental
Ammonium Acetate crystalline 'AR'	NH <sub>4</sub> CH <sub>3</sub> COO	77.09	Irritant
Ammonium Nitrate 'Analar'	NH <sub>4</sub> NO <sub>3</sub>	80.04	Explosive
Magnesium Chloride granular 'AR'	MgCl <sub>2</sub> .6H <sub>2</sub> O	203.3	Irritant
Magnesium Sulphate heptahydrate 'AR'	MgSO <sub>4</sub> .7H <sub>2</sub> O	246.48	Irritant
Formamide 'AR'	NH <sub>2</sub> CHO	45.04	Irritant
Dimethylsulphoxide 'AR'	CH <sub>3</sub> SOCH <sub>3</sub>	78.13	Irritant and flammable
Urea 'AR'	NH <sub>2</sub> CONH <sub>2</sub>	60.06	irritant

### 6.2.2. Sip list development

The procedure to create the SIP (Species Identification Protocol) list on proprietary software package iDiscover was firstly to select blocks with mineral phases of interest. It is important that the user knows the mineral under view so as to calibrate the mineral list. QEMSCAN is a powerful analytical tool but it is usually preceded by cheaper characterisation techniques such as XRF or XRD, so the user should know some of the mineral chemistry before QEMSCAN analysis.

In Figure 6.1, the surface examined is of white ‘china’ clay known as kaolinite. It has an empirical formulae of  $Al_2Si_2O_5(OH)_4$  and elemental composition of 55.78 wt % O, 20.90 wt % Al, 21.76 wt % Si (Webmineral.com, 2017).

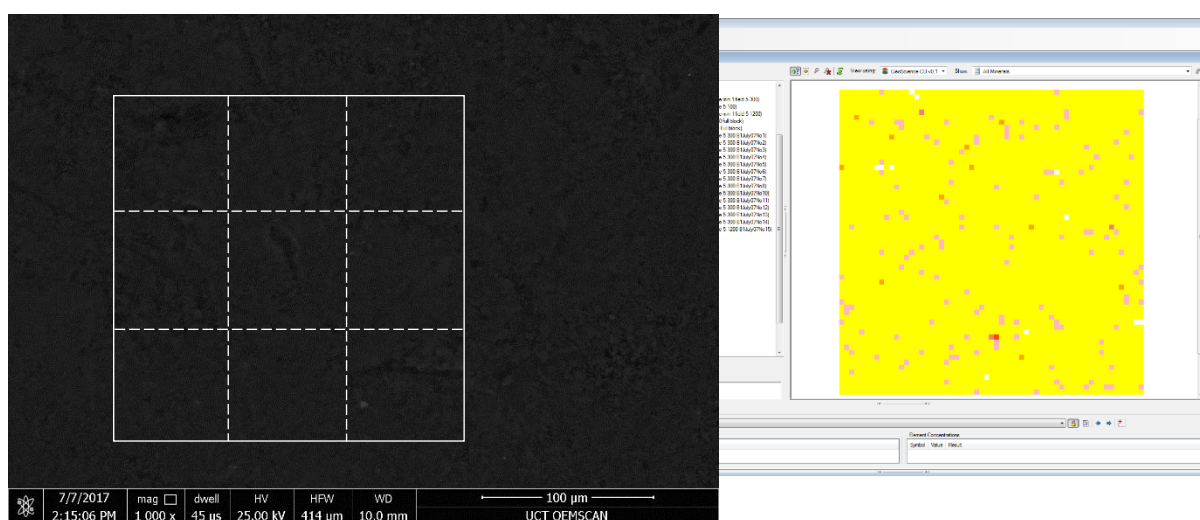


**Figure 6.1 Surface selection for SIP list editing (yellow - kaolinite)**

This surface was selected because it is known to the user and it was visually uniform. A grid the size of the field size is created by the user, and a pixel from each sub-square is chosen at random and its composition recorded. The grid for this section is shown in Table 6.3.

**Table 6.3 Average elemental concentrations for grid selections**

Grid Number:	1	2	3	4	5	6	7	8	9	ave	std dev
Al	40.5	34.7	32.1	34.5	41.1	39.9	35.0	34.4	34.3	36.3	3.1
Si	34.9	43.1	35.7	39.8	34.4	34.3	38.7	41.5	35.4	37.5	3.1

The EDS detector has more difficulty detecting lighter elements than heavier elements, thus the oxygen values were not used in the mineral identification. The Al / Si ratio (36.3 / 37.5) is similar to the Webmineral elemental concentration Al / Si ratio of 20.90 / 21.76.

The average values for kaolinite were determined from the grid section and were used as an initial value for the classification of the pixel information. This grid procedure is a standard method used in geology for sampling large areas. The SIP list uses a range of concentration for the assignment of each element in a mineral, so the lower part of the range is given as the average value minus the standard deviation, and the upper bound is the average plus the standard deviation. Multiples of the standard deviation are used to extend the element ranges. This is shown in Table 6.4.

**Table 6.4 Upper and lower conditions for SIP list mineral kaolinite**

dev	1		2		3		4		5	
	lower	upper	lower	upper	lower	upper	lower	upper	lower	upper
Al	33.2	39.4	30.1	42.5	27.0	45.6	23.9	48.7	20.8	51.8
Si	34.4	40.7	31.3	43.8	28.1	46.9	25.0	50.1	21.9	53.2

To determine the optimal standard deviation multiple, the number of pixels is recorded with increasing ranges. The results are shown in Figure 6.2.

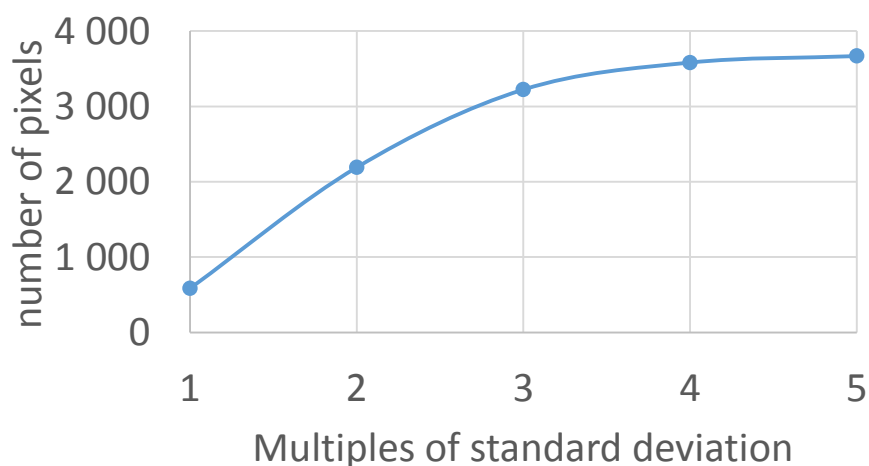


**Figure 6.2 Number of pixels assigned as kaolinite on SIP list as a function of the element range**

As the range for the elemental concentrations increases, more pixels are assigned as kaolinite. At 5 times the standard deviation, 3 668 pixels are assigned as kaolinite. This is assumed to be very close to maximum kaolinite pixels possible. At 1 times the standard deviation, only about 16 % of the pixels are selected. At 3 times the standard deviation, more than 85 % of the pixels are selected, so this range was used for further debugging.

Debugging is the major process in QEMSCAN of assigning all pixels to their respective mineral descriptions, which include the theoretical formulae, element mass and density used in the QEMSCAN calculations. The user must use a combination of BSE imaging and sample background knowledge to determine the accuracy of pixel allocation. The major issue in debugging is usually pixels out of place/inside/adjacent to unrelated phases. The other issue is extra heavy elements occurring which is outside of the list criteria.

The brightness from the BSE image is a function of the average atomic number. In this study, kaolinite is shown in darker grey levels because it is made from light elements Al and Si. Heavier elements such as Fe, Mn and Ce show as brighter white textures. This colour difference is enough to distinguish between the phases and thus compare with pixel allocations for accuracy.

Minerals created on the SIP list are arranged in a hierarchy, with the mineral at the top of the list being the first mineral to be considered when assigning pixels. Thus it is important to create minerals for the list strategically, starting with the major mineral. Less common minerals would follow it down the list. A tool to help separate one mineral from another is the designation of a trap phase. A trap is essentially a mineral created which allows for all concentrations of one element. For example, in Figure 6.3 the lighter material is potentially due to heavier elements such as Mn, Fe and Ce. These minerals are set in a darker environment made from Al and Si, with some kaolinite present as geometric shapes.

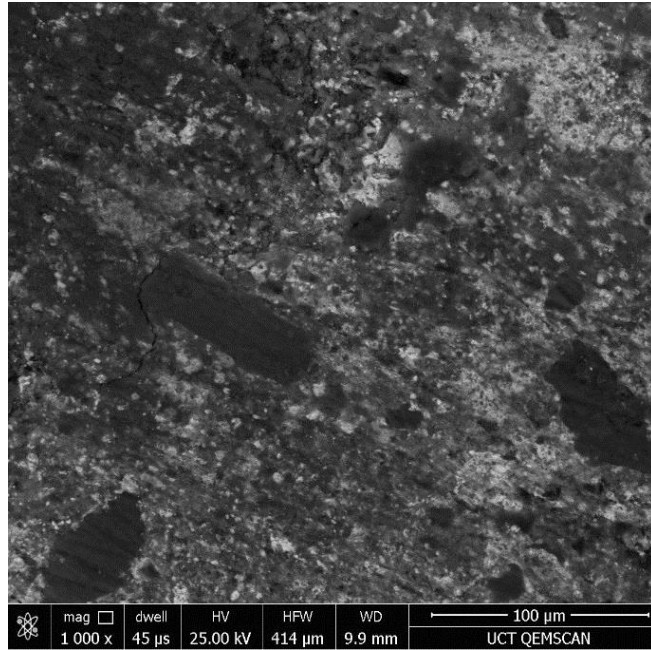


**Figure 6.3 QEMSCAN image of kaolinite with Mn, Ce phases as lighter phases**

To classify Ce minerals, a Ce trap is created which assigns all pixels to it no matter how much Ce was measured. This is shown in Figure 6.4, where the green is all pixels with Ce present. The remaining is kaolinite.

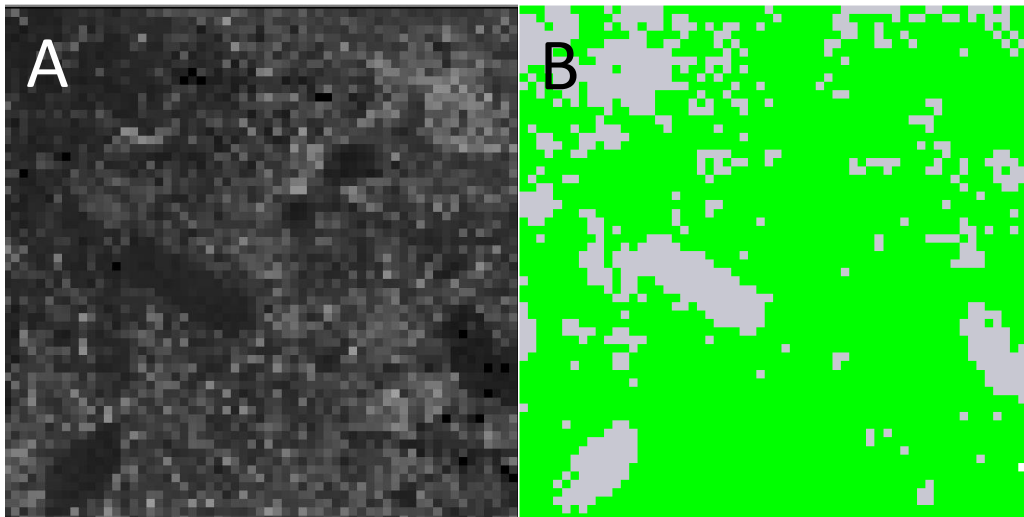


**Figure 6.4 BSE pixel field (A) and Ce trap pixel allocation (B) shown as green**

The pixels assigned to kaolinite are coloured yellow, quartz are light pink, and the Ce trap needs to be investigated. Ce minerals need to be created to distinguish the separate Ce phases. This process is shown in Figure 6.5. Figure 6.5 part C shows the kaolinite in yellow



with the light blue section bordering it. This mineral is assigned as a Clay-Ce interface. This category would have the required concentrations of Al and Si for Kaolinite but with some Ce.

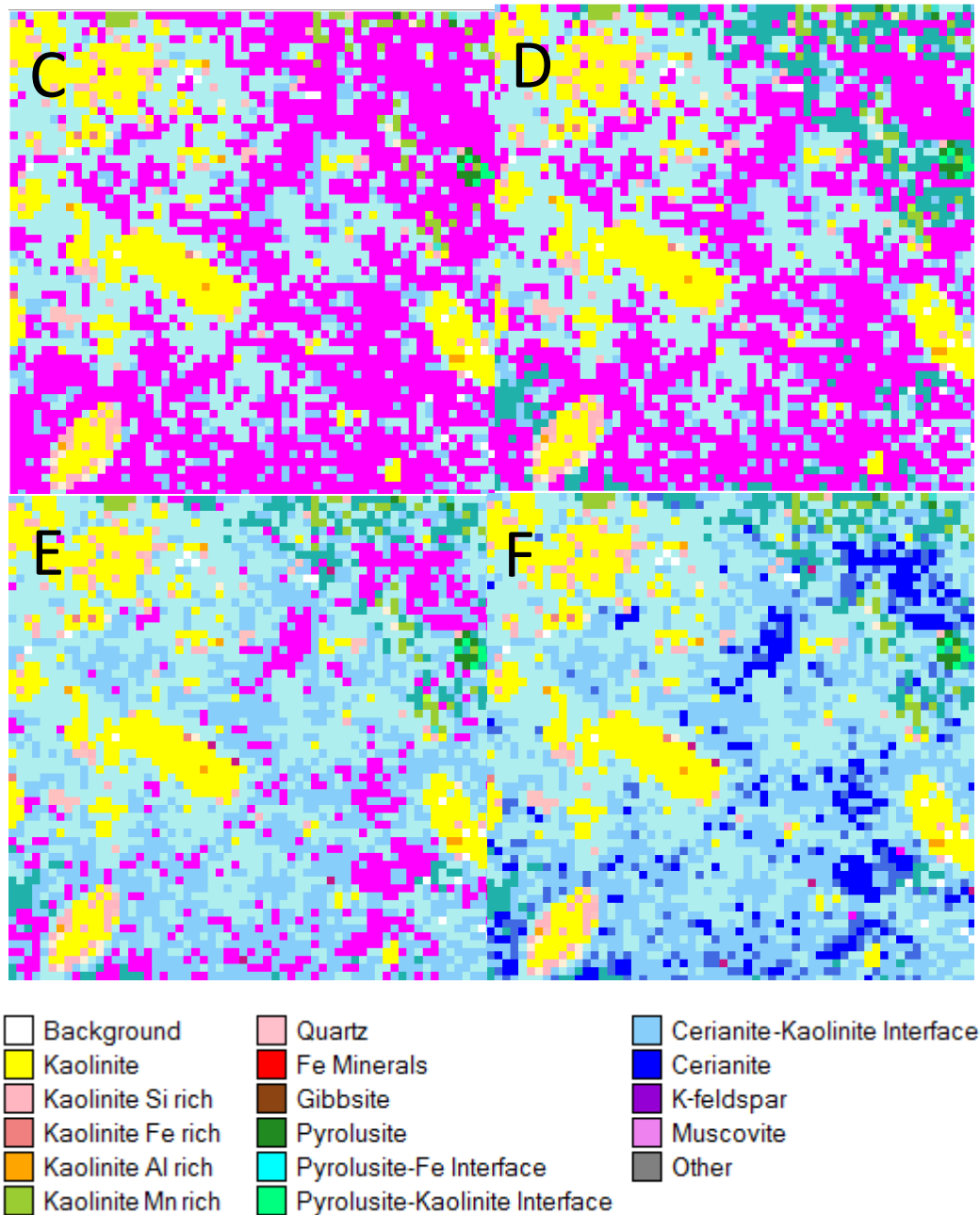


**Figure 6.5 Progressive mineral assignment using trap (pink) development, C Kaolinite and full trap assigned, D Pyrolusite-kaolinite Interface assigned, E Cerianite-kaolinite interface assigned, F Cerianite assigned**

The final process in debugging is combining the editing of multiple fields and incorporating as many of the gangue minerals present to have a comprehensive SIP list.

## 6.3. Results and Discussion

### 6.3.1. XRF trace elements

**Table 6.5 X-Ray Florescence (XRF) trace element results**

Element	Sample (ppm)			
	A1	A2	B	F
Mn	2 289	3 761	2 158	3 086
Zr	2 264	2 387	2 504	2 557
Y	142	955	691	992
Nb	354	399	402	422
Zn	276	262	247	250
F	231	298	325	292
S	378	324	316	291
Cl	108	117	126	114

### 6.3.2. Hinckley Index calculations

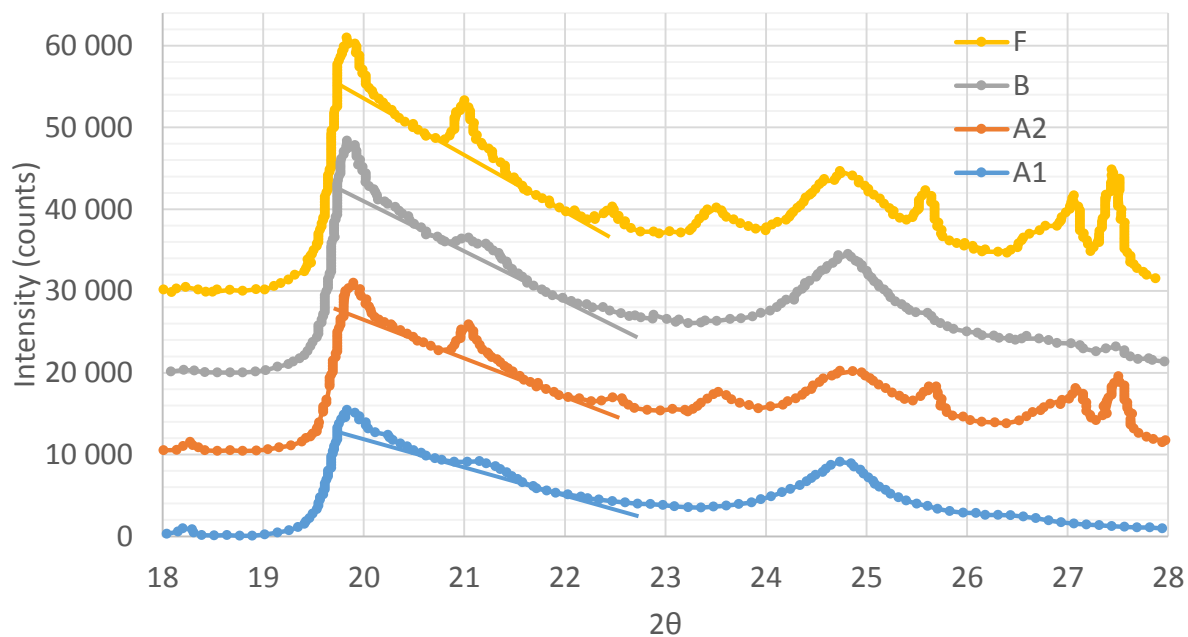


**Figure 6.6 Diffractogram for the Hinckley Index calculations shown in Table 6.6 for samples A1, A2, B and F**

**Table 6.6 Hinckley Index Calculations (counts)**

Figure 6.6 parameters	A1	A2	B	F
A	3 209	4 054	6 757	6 757
B	1 351	4 392	2 280	6 926
At	15 659	21 030	28 378	30 912
Hinckley Index	0.29	0.40	0.32	0.44

6.3.3. QEMSCAN blocks

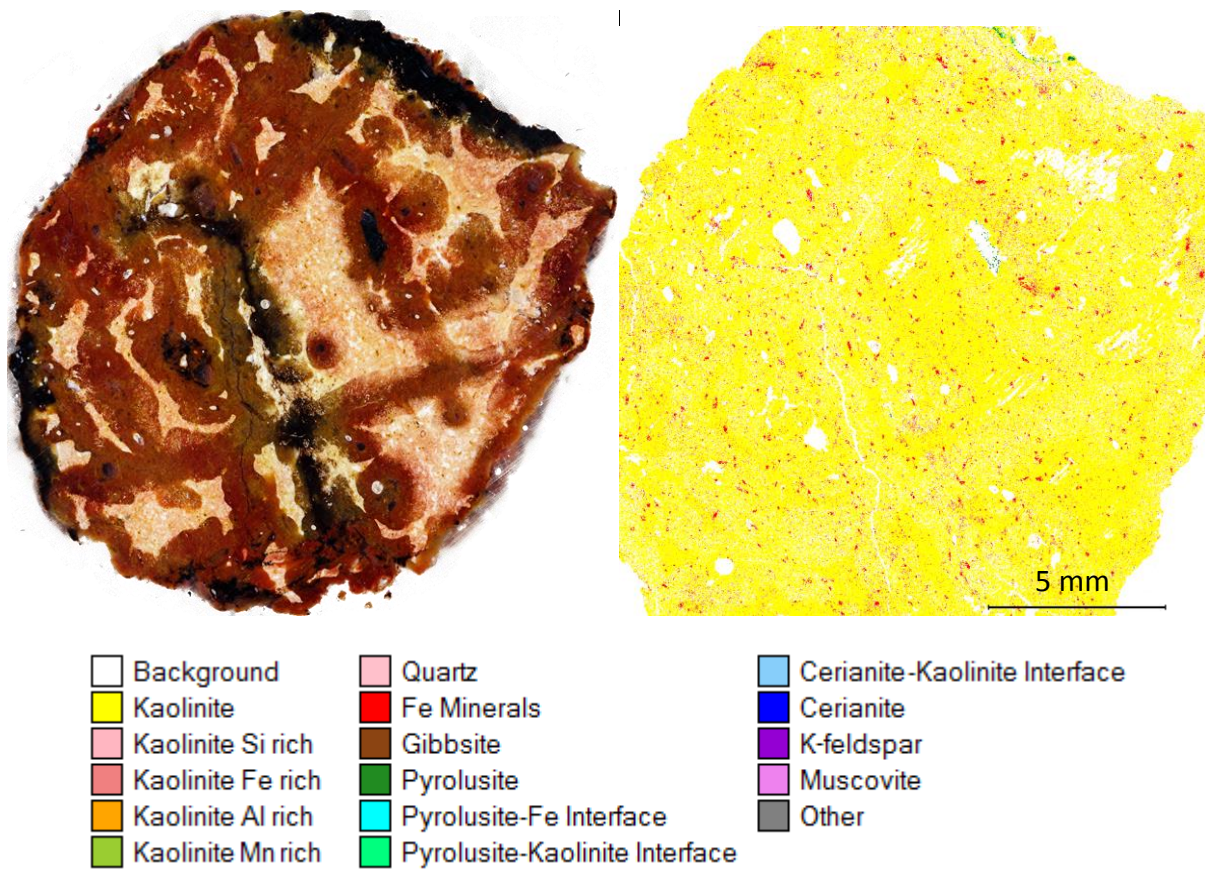


**Figure 6.7 Sample A1 block mount (left) (block 1) and false colour field scan image (right)**

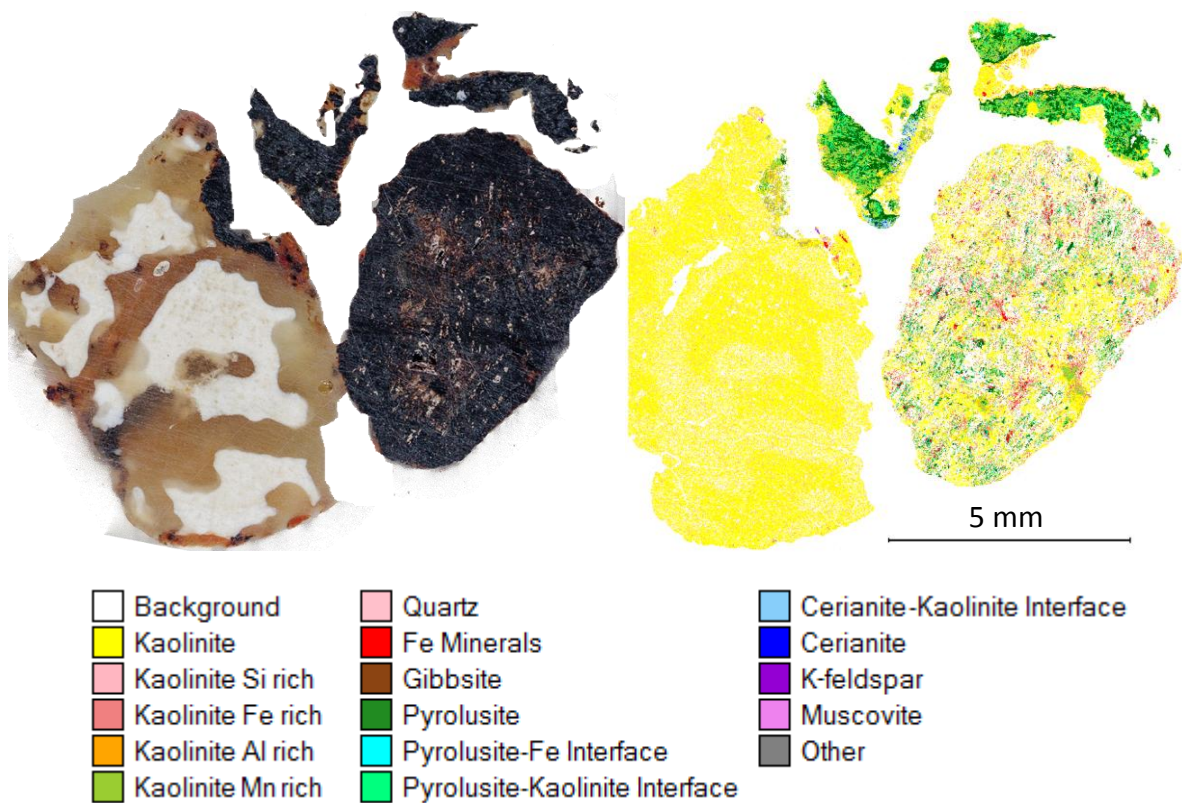


Figure 6.8 Sample A1 block mount (left) (block 3) and false colour field scan image (right)

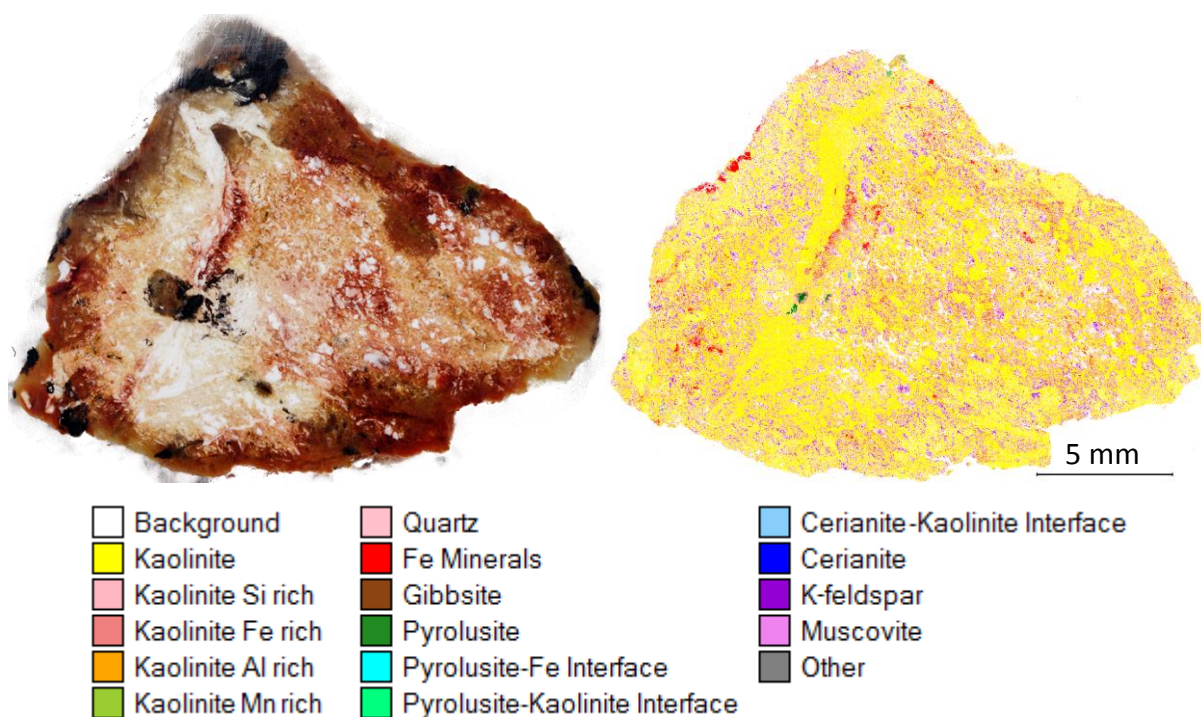


Figure 6.9 Sample A2 block mount (left) (block 5) and false colour field scan images (right)

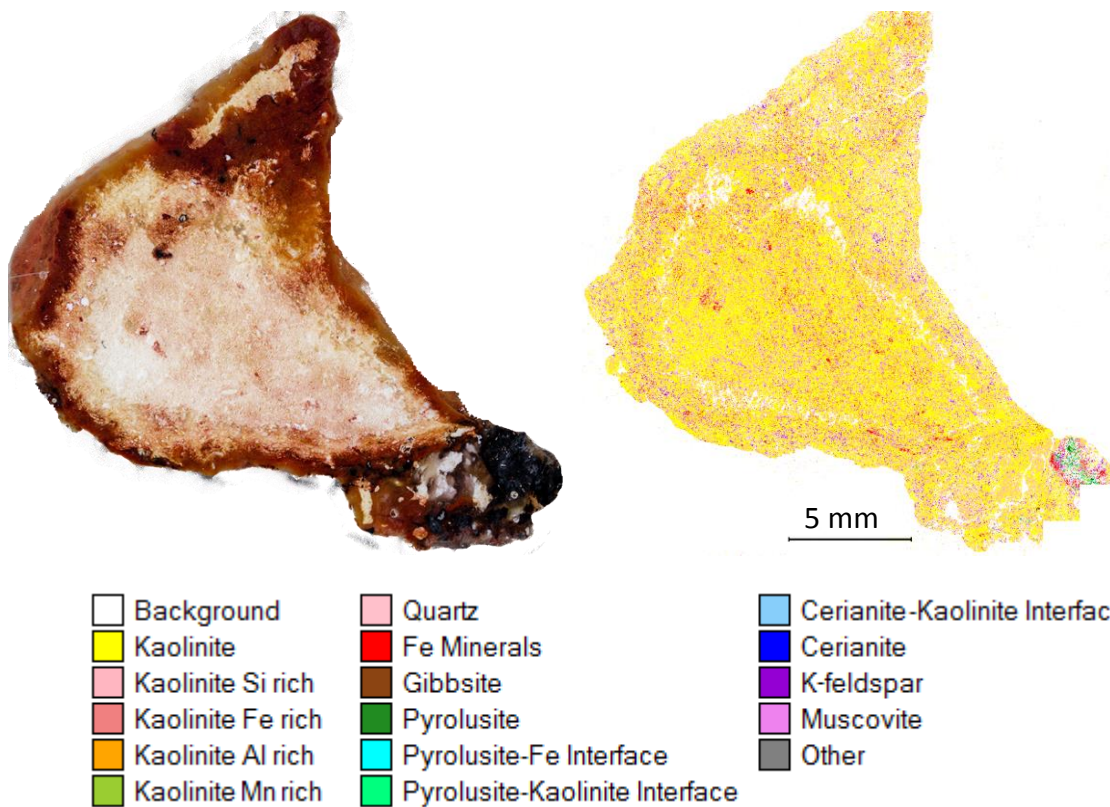


Figure 6.10 Sample A2 block mount (left) (block 6) and false colour field scan images (right)

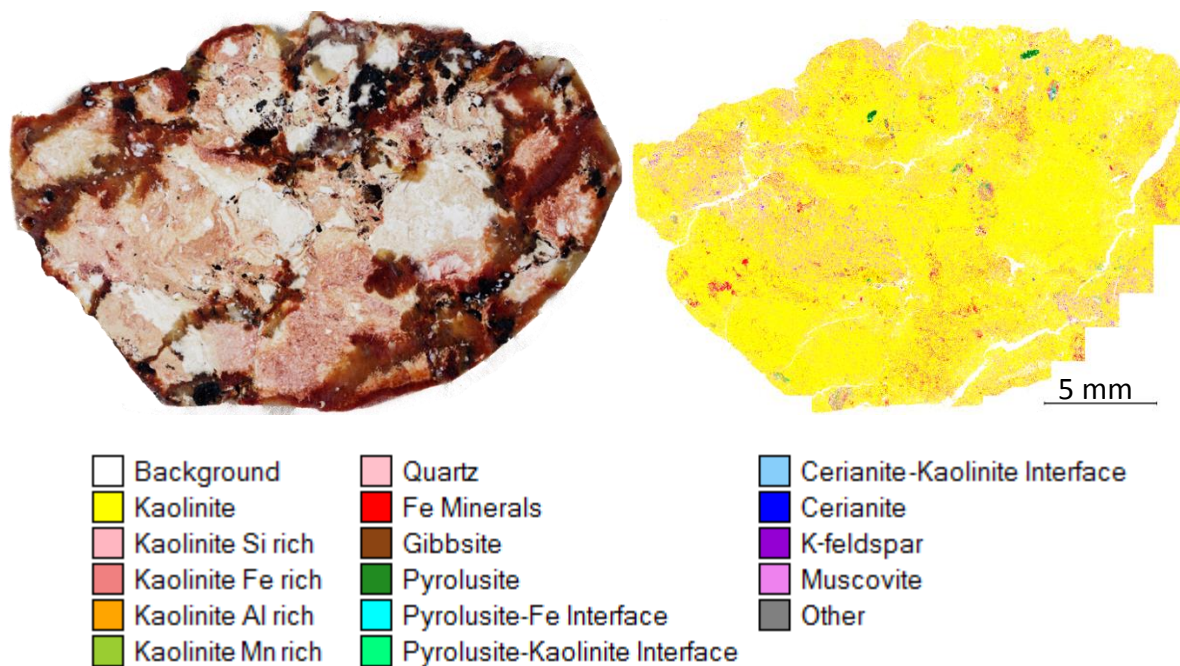


Figure 6.11 Sample B block mount (left) (block 7) and false colour field scan image (right)

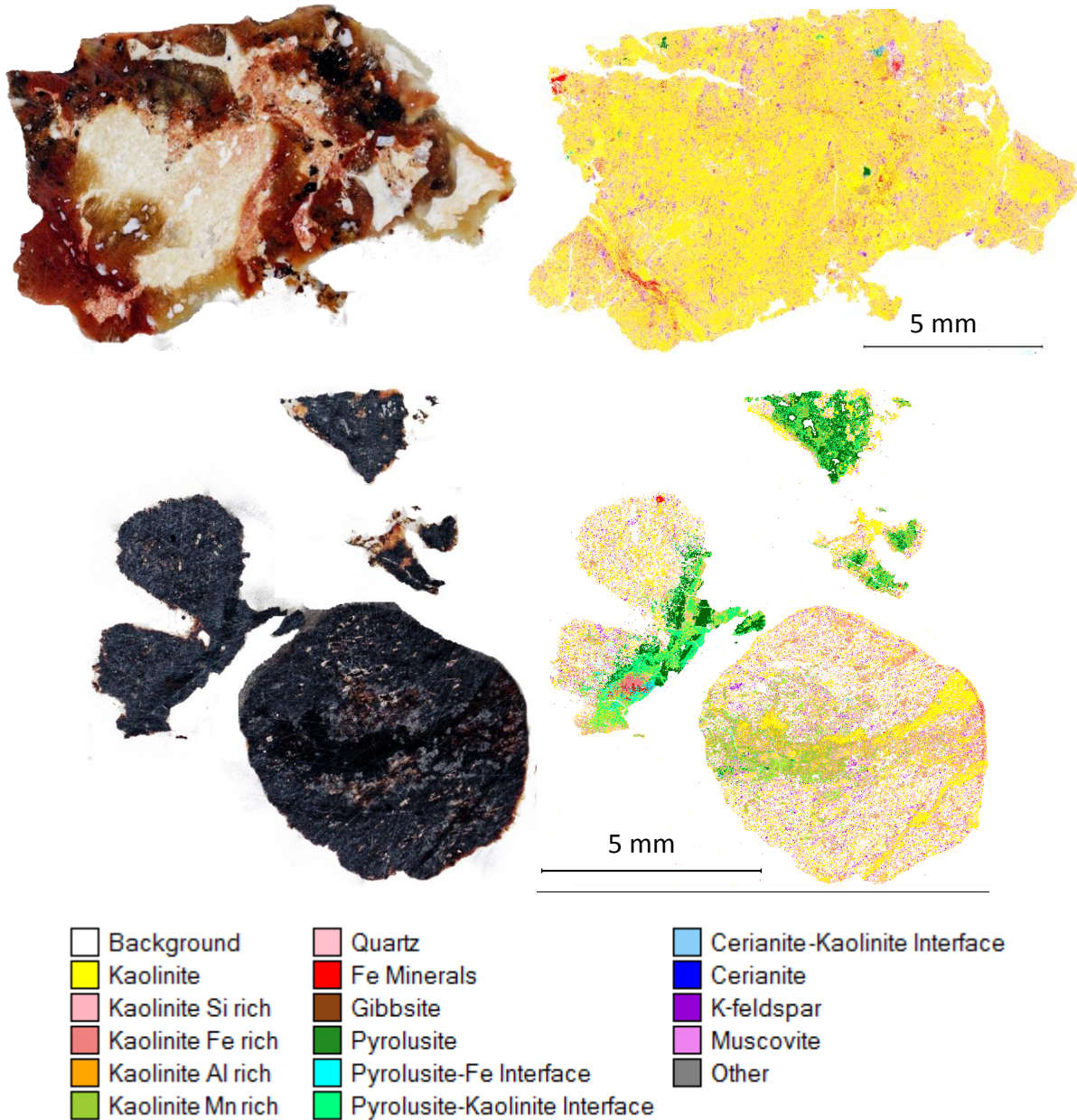


Figure 6.12 Sample F block mounts (left) (block 8 and 10) and false colour field scan images (right)

**Table 6.7 QEMSCAN Blocks 1 to 5 quantitative mineral content**

<b>Mineral Mass (%)</b>	Block 1 A1	Block 2 A1	Block 3 A1	Block 4 A2	Block 5 A2
Kaolinite	86.1	80.7	56.9	35.2	56.4
Kaolinite Fe rich	4.5	4.8	3.8	2.8	5.9
Kaolinite Si rich	5.1	8.6	6.8	10.3	17.5
Kaolinite Al rich	1.4	1.2	2.3	22.2	0.6
Kaolinite Mn Rich	0	0	7.9	1.7	0.1
Total Kaolinite	97.1	95.3	78.1	72.1	80.6
Quartz	0.3	3.3	0.9	6.2	7.3
Fe minerals	2.4	1.4	2.2	0.8	1.9
Gibbsite	0	0	0	2.5	0
K-Feldspar	0	0	0.1	1.6	2.7
Muscovite	0	0	0	4.6	7.4
Carbonates	0	0	1.1	0.5	0
Cerianite	0	0	0.6	0	0
Pyrolusite	0.2	0	11.5	7.5	0.2
Pyrolusite-Kaolinite Interface	0	0	4.8	3.2	0.1
Pyrolusite-Fe Interface	0	0	0.7	0.9	0
Total Mn Minerals	0.1	0	17.0	11.6	0.2
Other	0	0	0.3	0.1	0

Note: zero indicates not detected

**Table 6.8 QEMSCAN Blocks 6 to 10 quantitative mineral content**

<b>Mineral Mass(%)</b>	Block 6 A2	Block 7 B	Block 8 F	Block 9 F	Block 10 F
Kaolinite	56.8	76.4	58.6	63.2	22.0
Kaolinite Fe rich	5.4	4.4	3.1	2.7	6.5
Kaolinite Si rich	18.4	12.5	23.2	19.4	11.1
Kaolinite Al rich	1.8	1.5	0.5	0.7	2.1
Kaolinite Mn Rich	0.1	0.3	0.1	0.2	10.6
Total Kaolinite	82.6	95.2	85.5	86.2	52.4
Quartz	7.3	2.3	7.6	7.0	11.0
Fe minerals	1.6	0.9	1.0	0.8	1.1
Gibbsite	0	0	0	0	0
K-Feldspar	1.9	0.2	1.7	1.5	2.2
Muscovite	5.9	0.9	3.5	3.9	5.4
Carbonates	0	0	0.3	0	0.1
Cerianite	0	0.1	0.1	0	0.1
Pyrolusite	0.5	0.3	0.2	0.4	18.4
Pyrolusite-Kaolinite Interface	0.2	0.1	0.1	0.1	8.0
Pyrolusite-Fe Interface	0	0.1	0	0.1	1.3
Total Mn Minerals	0.7	0.4	0.3	0.6	27.7
Other	0	0	0	0	0.1

Note: zero indicates not detected



6.3.4. Fe QEMSCAN images

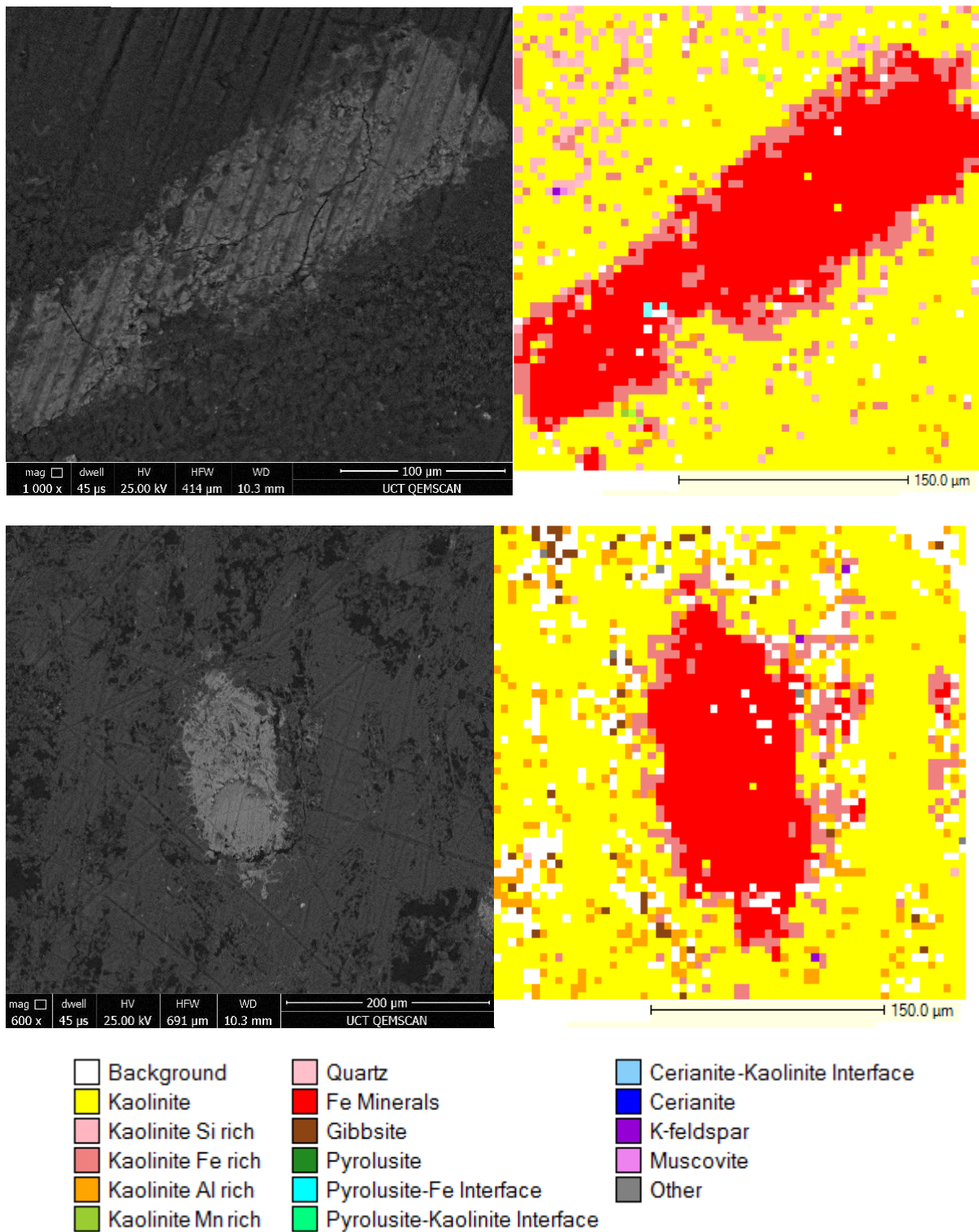


Figure 6.13 BSE QEMSCAN image (left) showing Fe minerals and false colour field scan images (right)

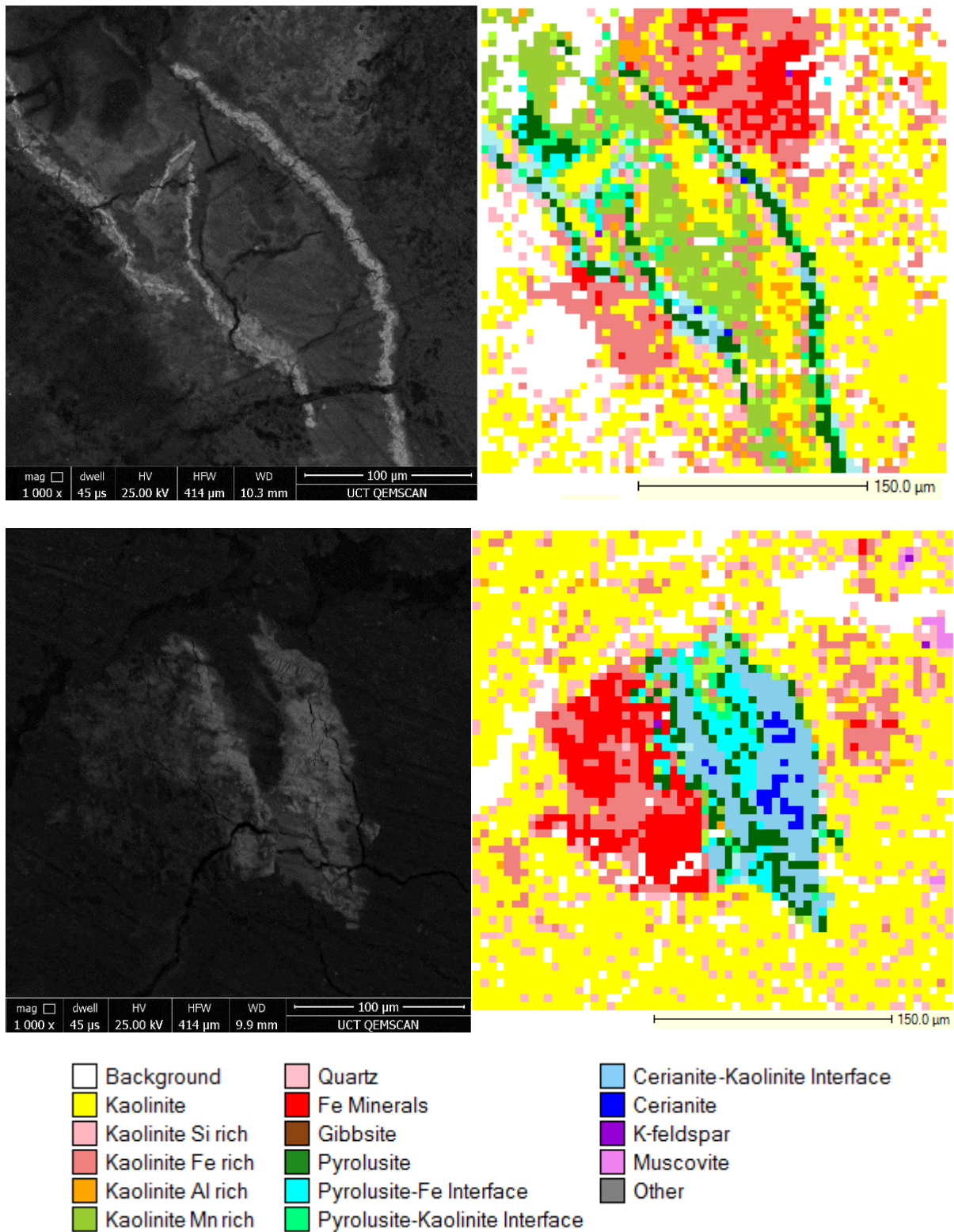


Figure 6.14 BSE QEMSCAN image (left) showing Fe minerals with Mn and Ce minerals and false colour field scan images (right)

6.3.5. Mn QEMSCAN images

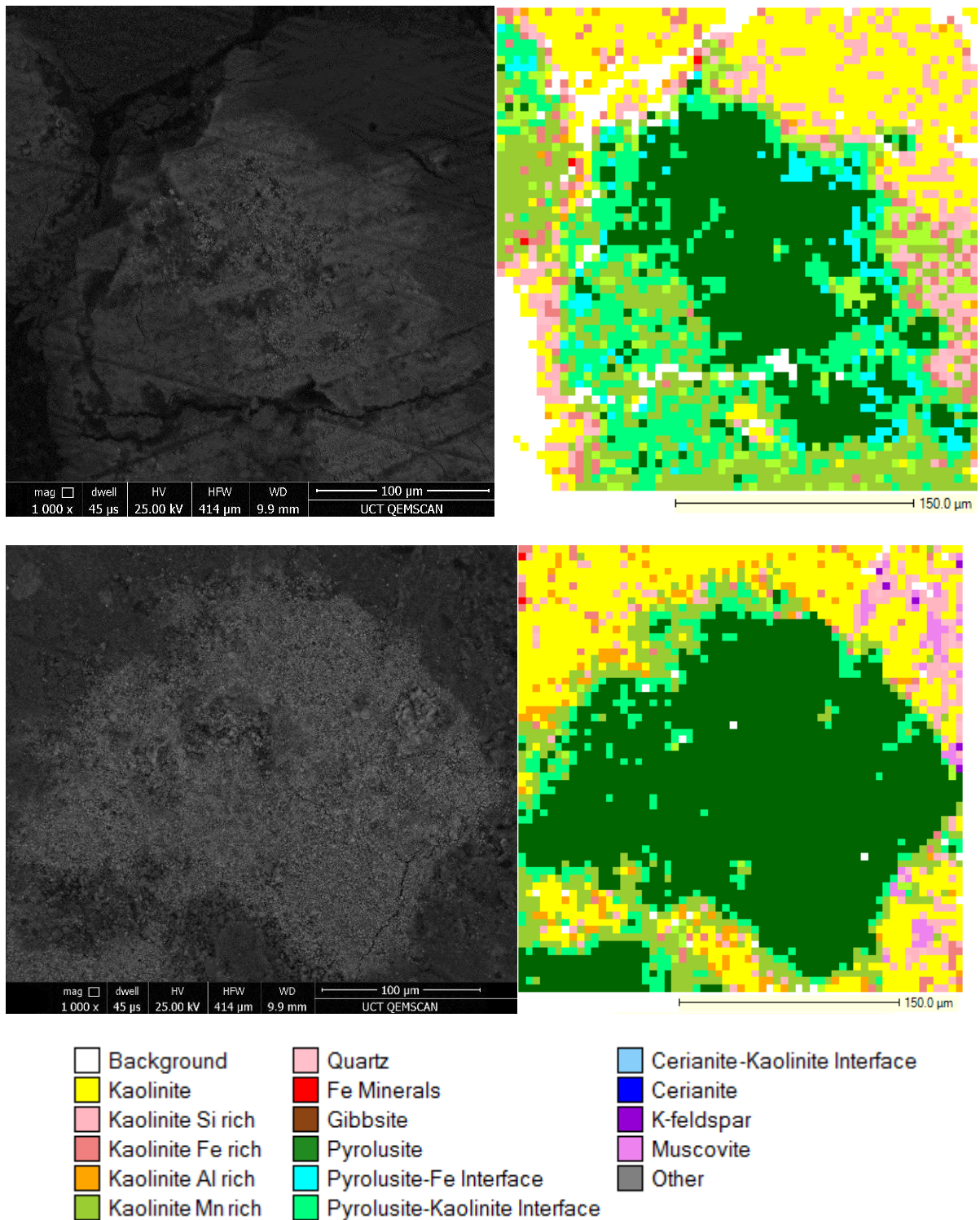
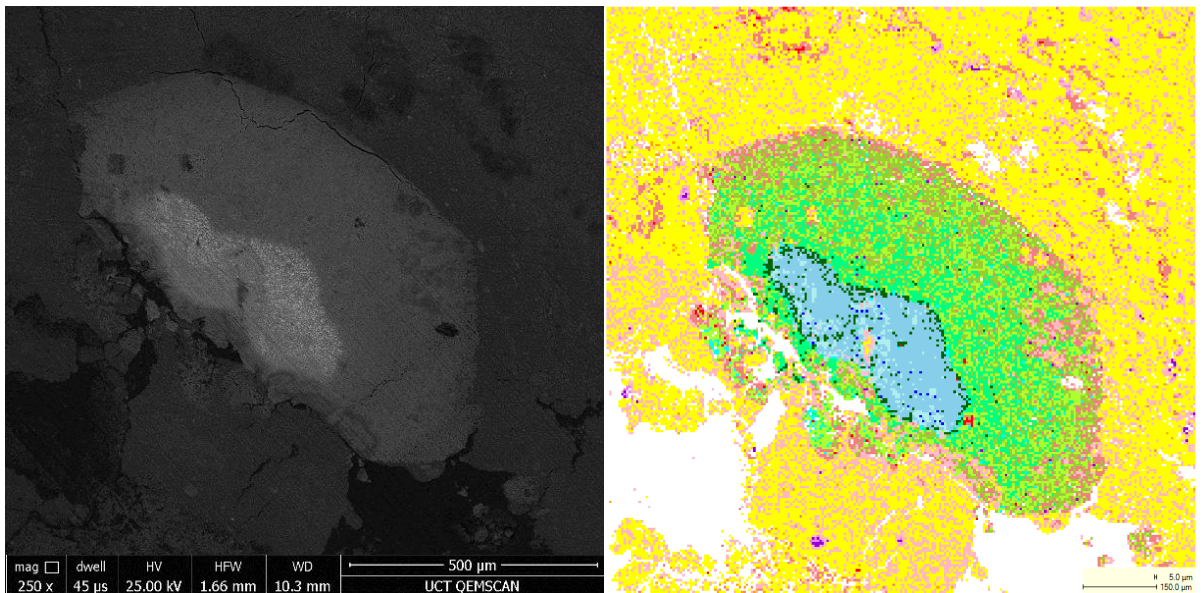
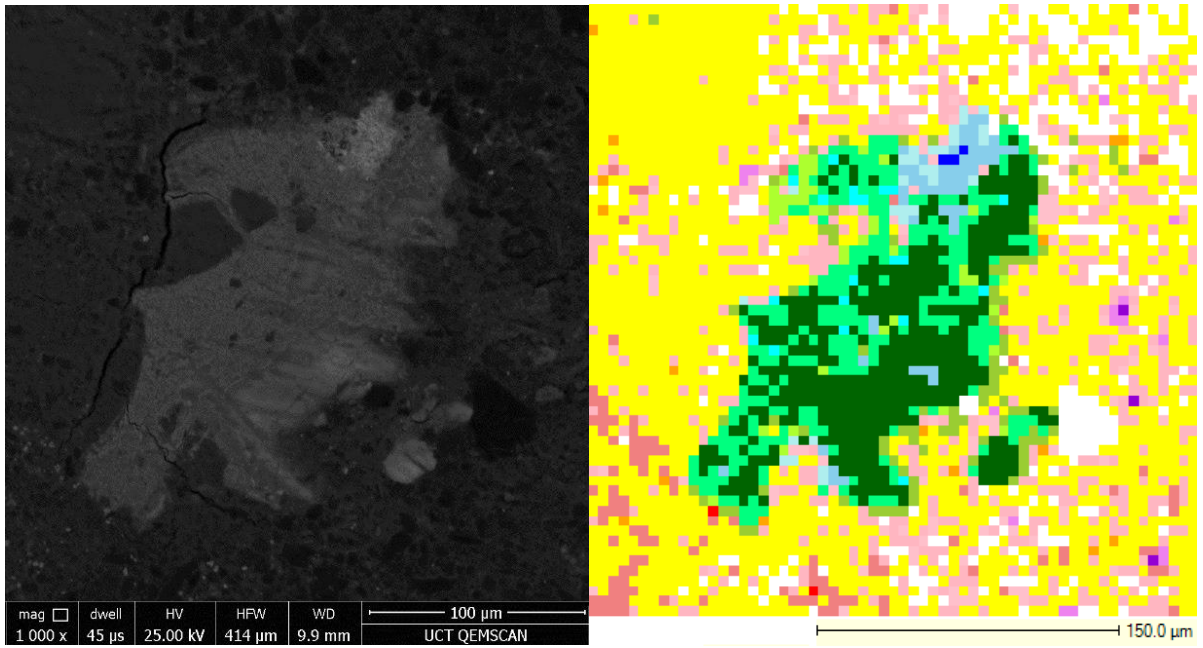


Figure 6.15 BSE QEMSCAN image (left) showing Mn minerals and false colour field scan images (right)



- |                   |                                |                               |
|-------------------|--------------------------------|-------------------------------|
| Background        | Quartz                         | Cerianite-Kaolinite Interface |
| Kaolinite         | Fe Minerals                    | Cerianite                     |
| Kaolinite Si rich | Gibbsite                       | K-feldspar                    |
| Kaolinite Fe rich | Pyrolusite                     | Muscovite                     |
| Kaolinite Al rich | Pyrolusite-Fe Interface        | Other                         |
| Kaolinite Mn rich | Pyrolusite-Kaolinite Interface |                               |

Figure 6.16 BSE QEMSCAN image (left) showing Mn minerals with Ce minerals and false colour field scan images (right)

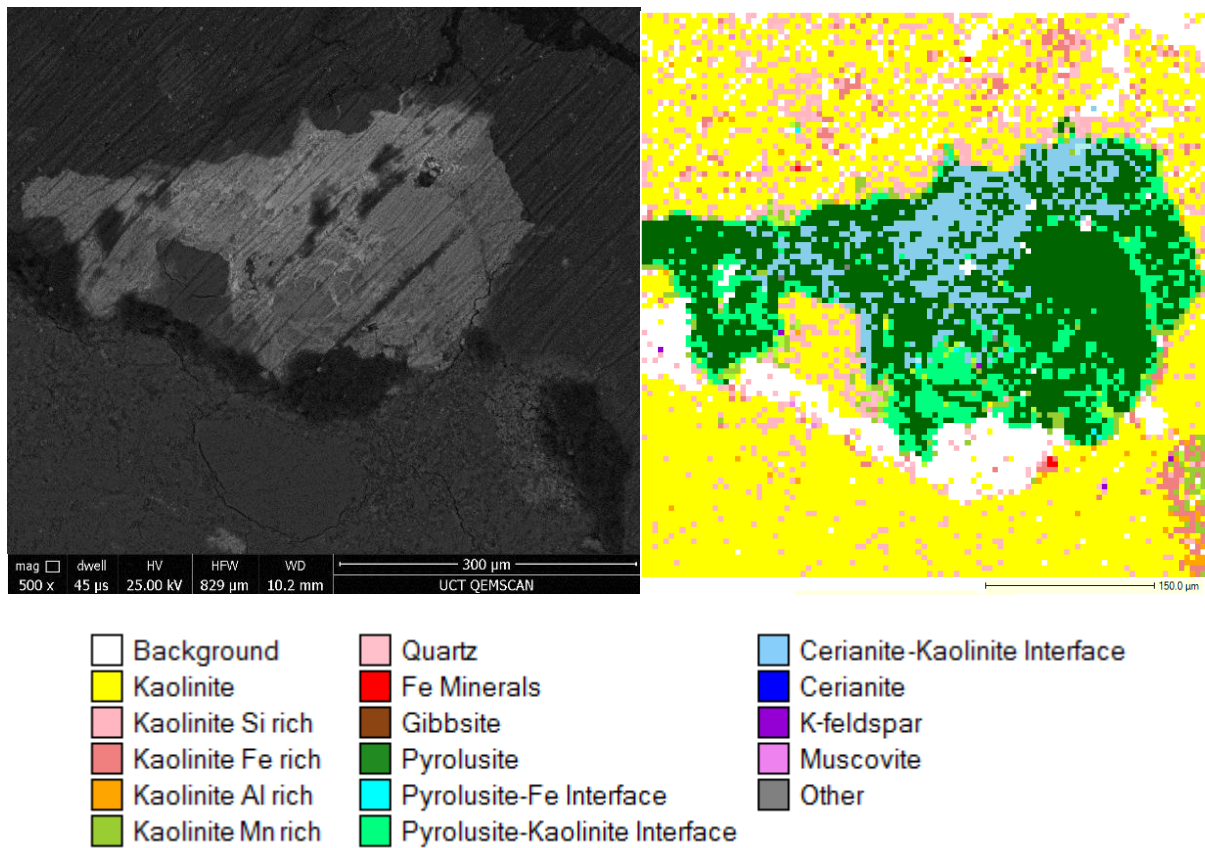


Figure 6.17 BSE QEMSCAN image (left) showing Mn minerals with Ce minerals and false colour field scan images (right)

6.3.6. Ce QEMSCAN images

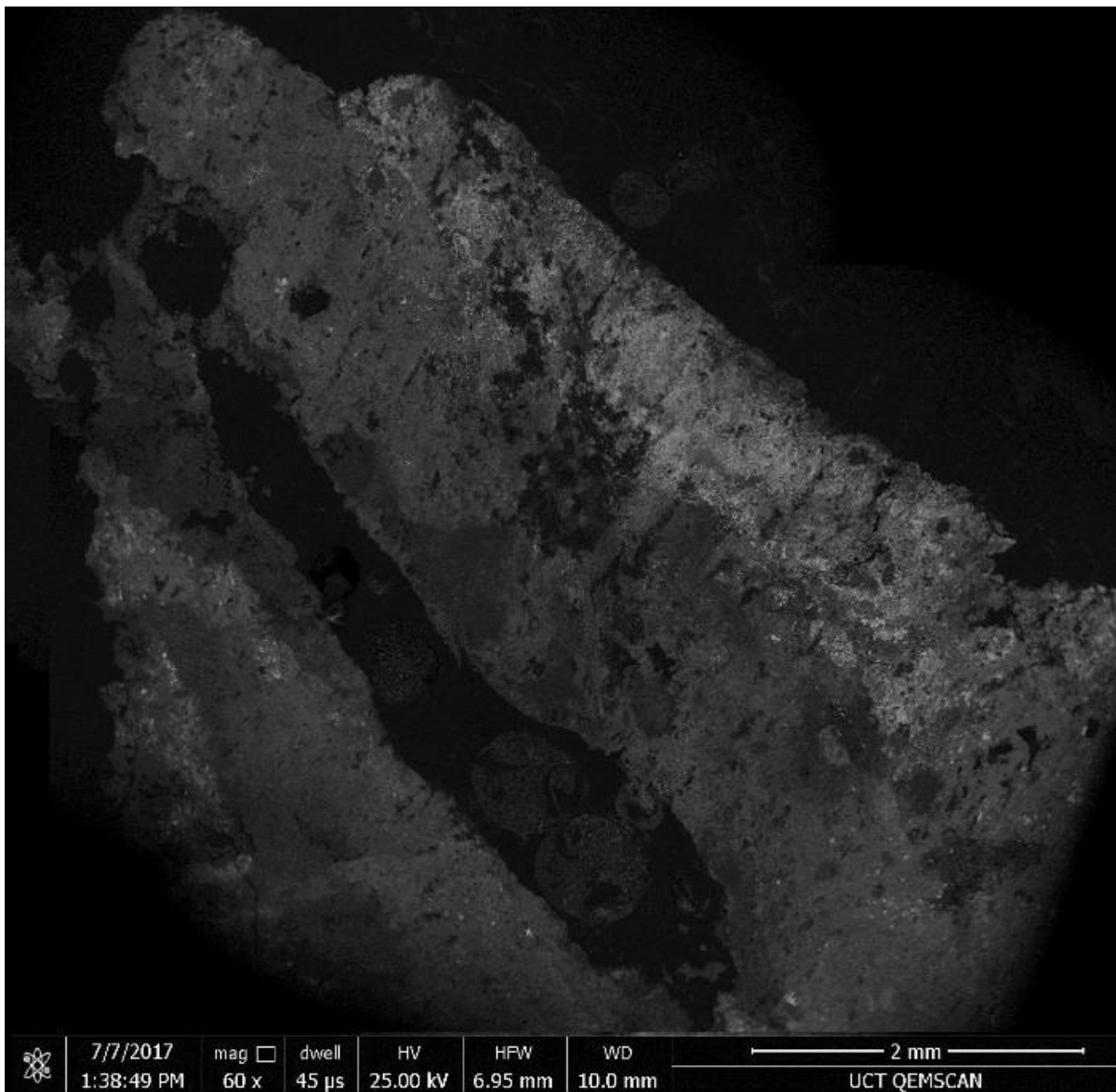
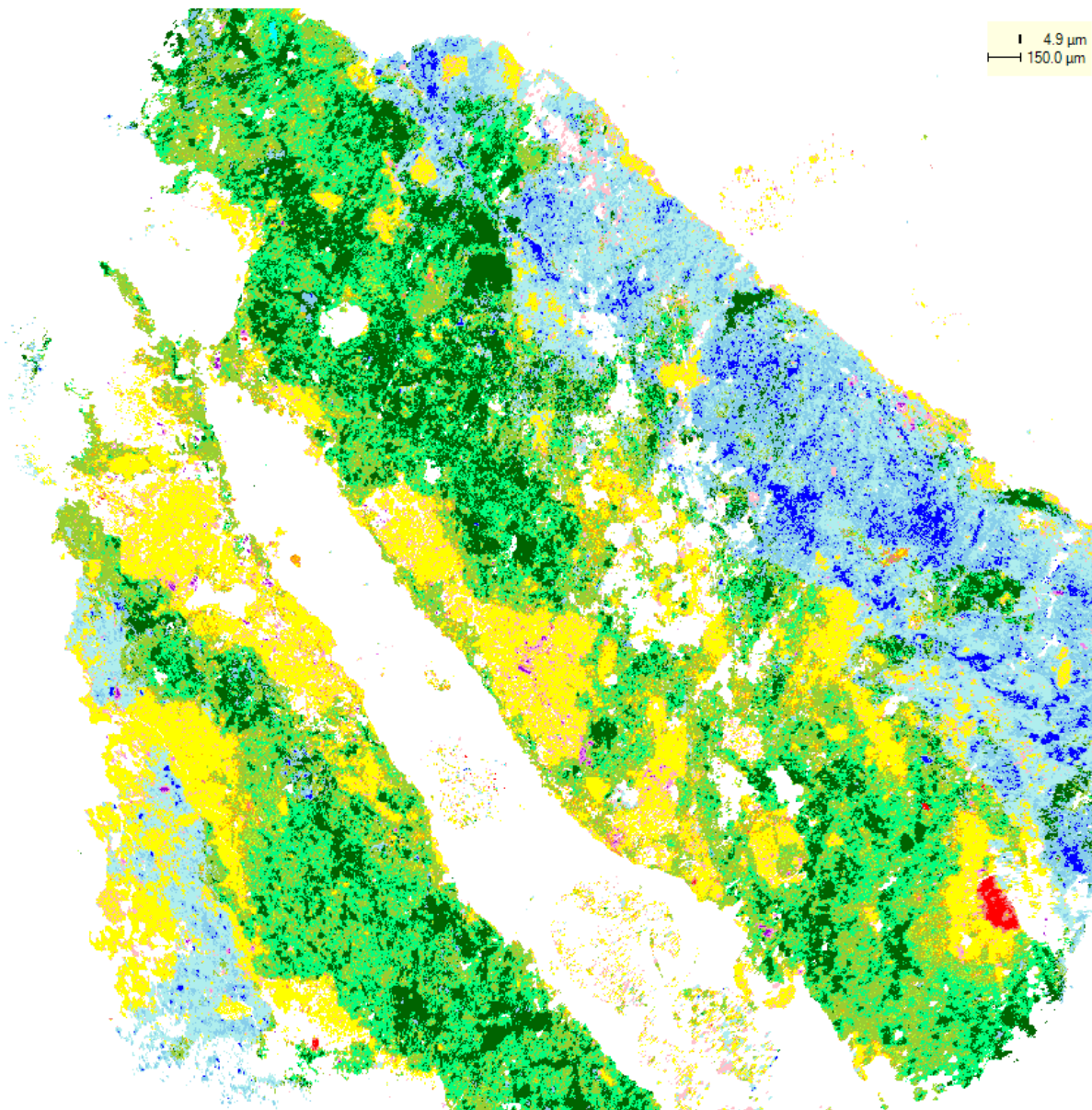


Figure 6.18 BSE image showing Mn and Ce minerals



Background	Quartz	Cerianite-Kaolinite Interface
Kaolinite	Fe Minerals	Cerianite
Kaolinite Si rich	Gibbsite	K-feldspar
Kaolinite Fe rich	Pyrolusite	Muscovite
Kaolinite Al rich	Pyrolusite-Fe Interface	Other
Kaolinite Mn rich	Pyrolusite-Kaolinite Interface	

Figure 6.19 False colour field scan image

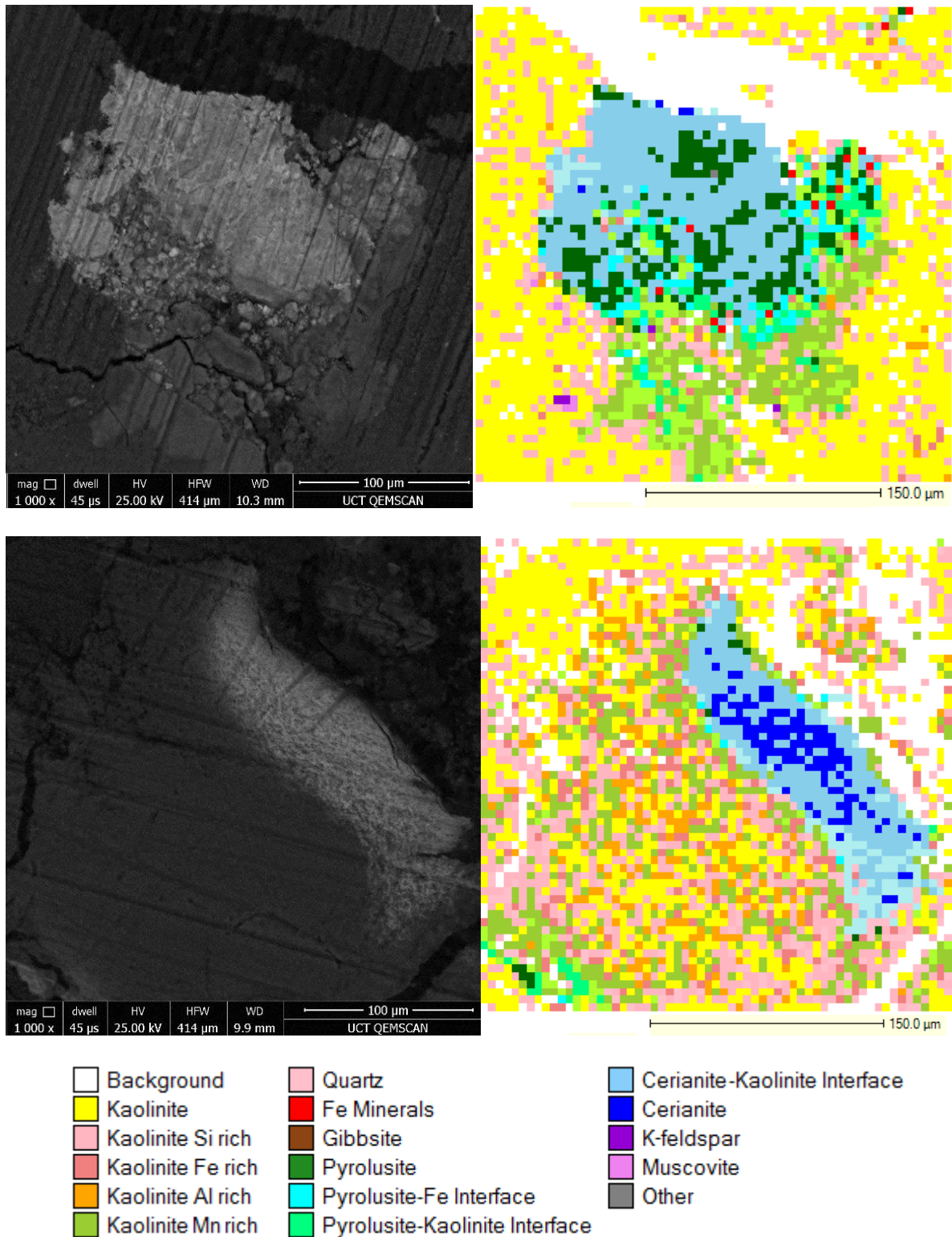
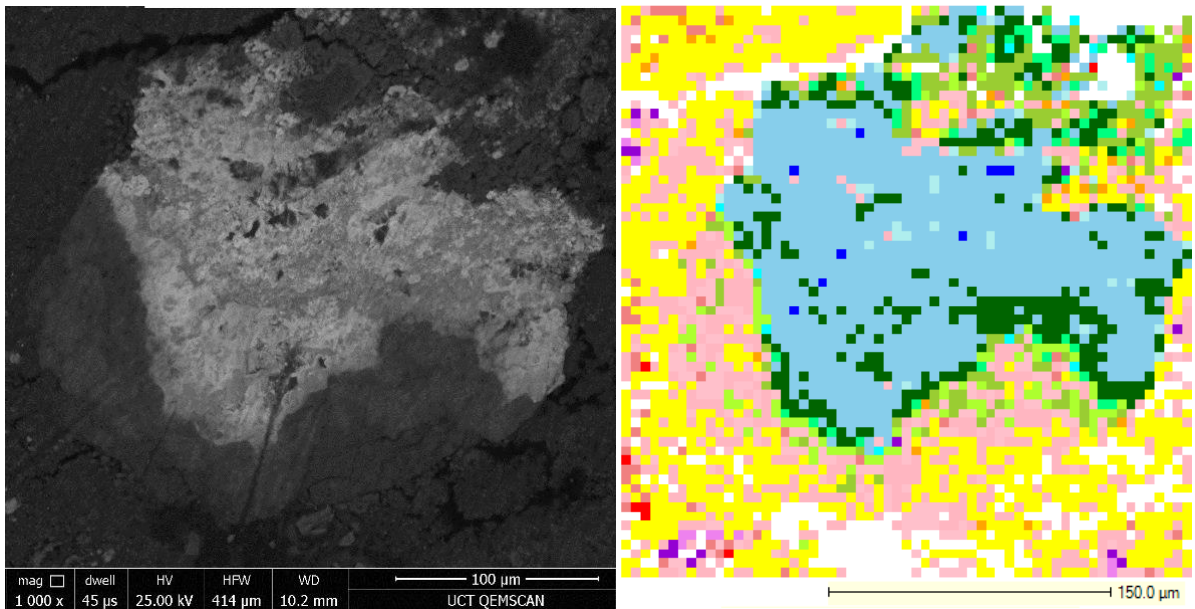
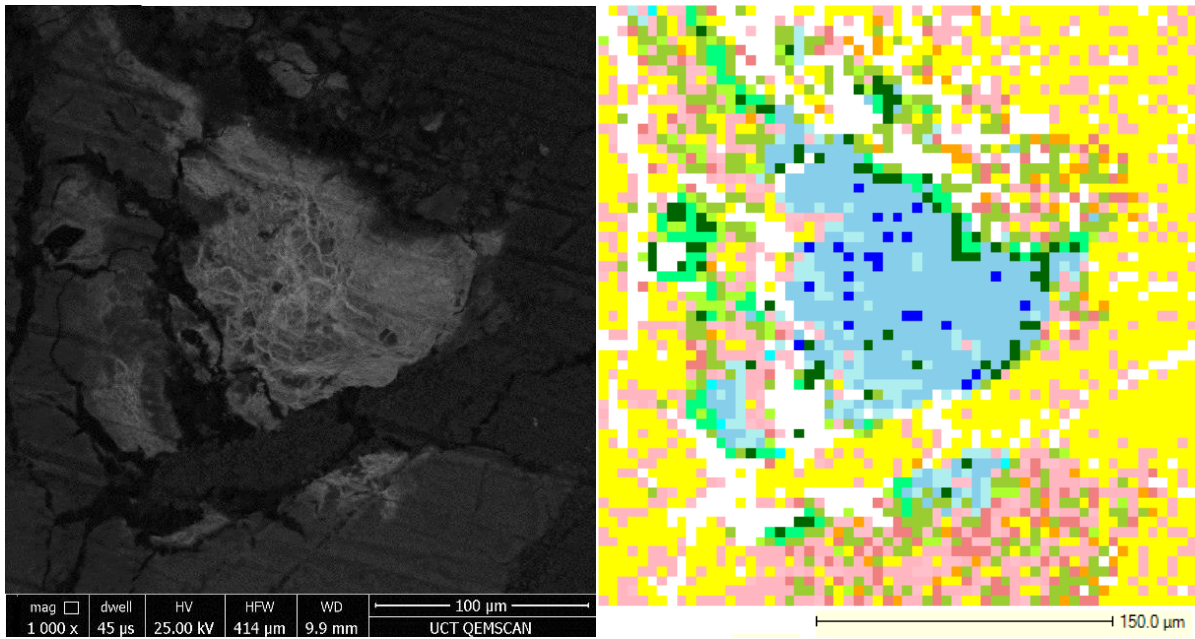


Figure 6.20 BSE QEMSCAN image (left) showing Ce minerals and false colour field scan images (right)





- |                   |                                |                               |
|-------------------|--------------------------------|-------------------------------|
| Background        | Quartz                         | Cerianite-Kaolinite Interface |
| Kaolinite         | Fe Minerals                    | Cerianite                     |
| Kaolinite Si rich | Gibbsite                       | K-feldspar                    |
| Kaolinite Fe rich | Pyrolusite                     | Muscovite                     |
| Kaolinite Al rich | Pyrolusite-Fe Interface        | Other                         |
| Kaolinite Mn rich | Pyrolusite-Kaolinite Interface |                               |

Figure 6.21 BSE QEMSCAN image (left) showing Ce minerals and false colour field scan images (right)

6.3.7. Zircon QEMSCAN images

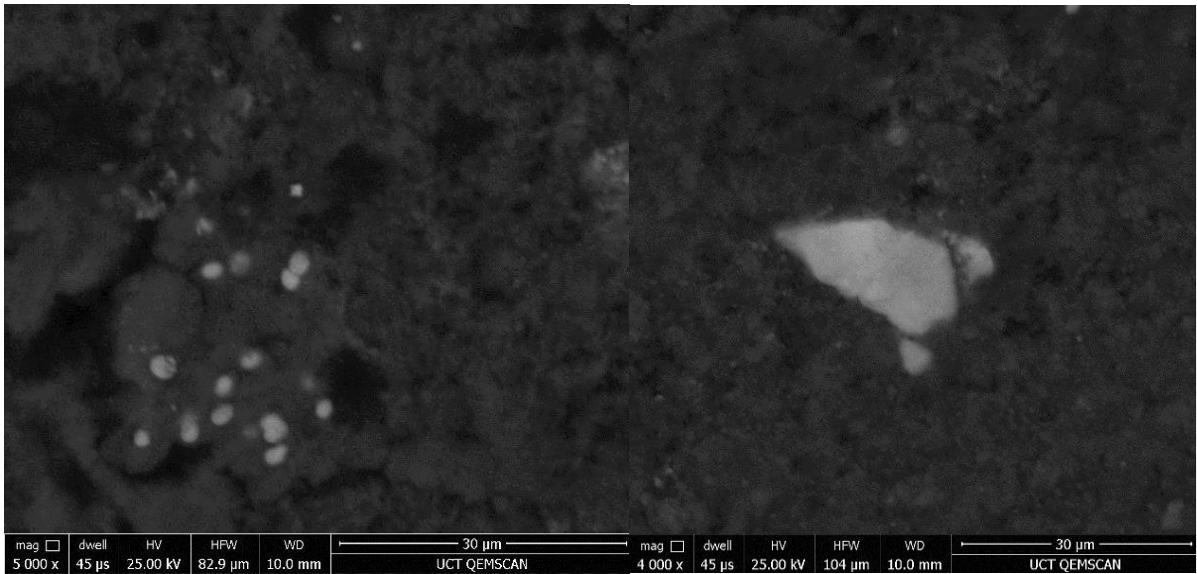


Figure 6.22 Sample A1 (left) and sample B (right) zircon (bright BSE) mineral images

6.3.8. SEM secondary electron images

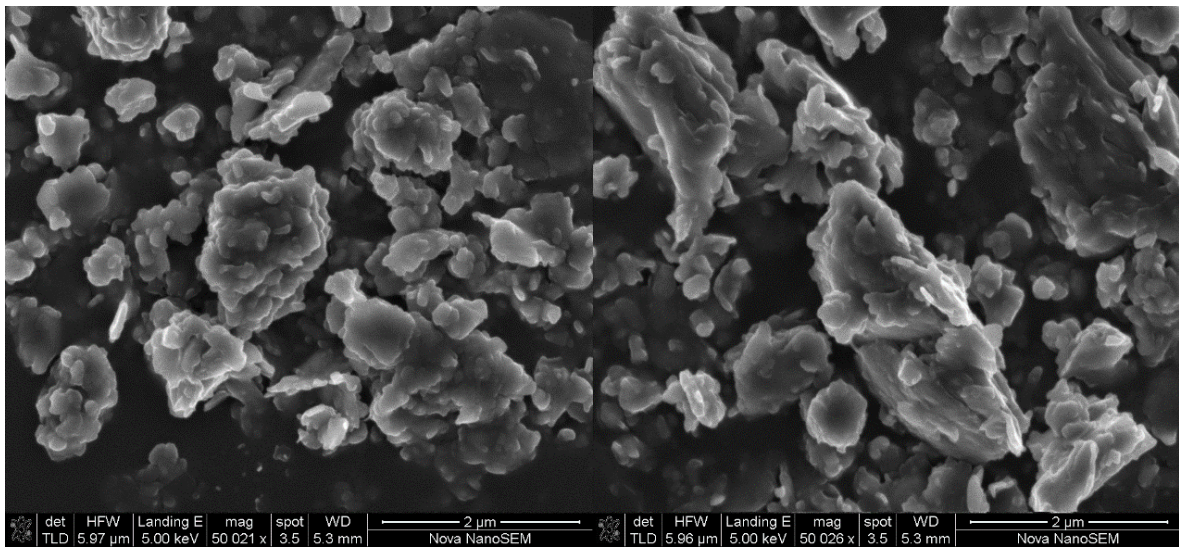


Figure 6.23 Kaolinite (red phase) SEM secondary electron images

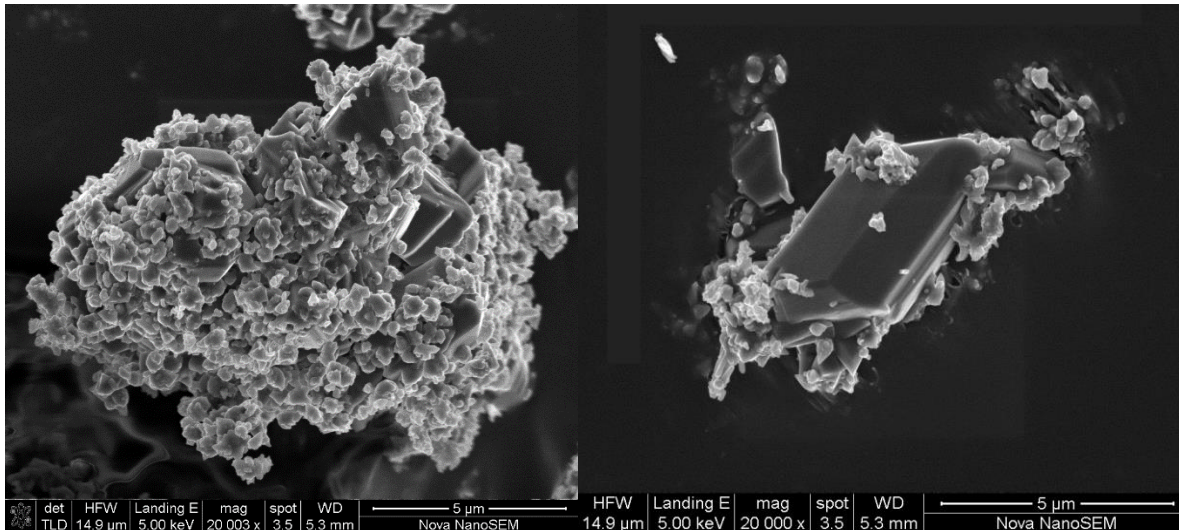


Figure 6.24 Kaolinite (tawny phase - left) and gibbsite (right) SEM secondary electron images

6.3.9. ICP-MS

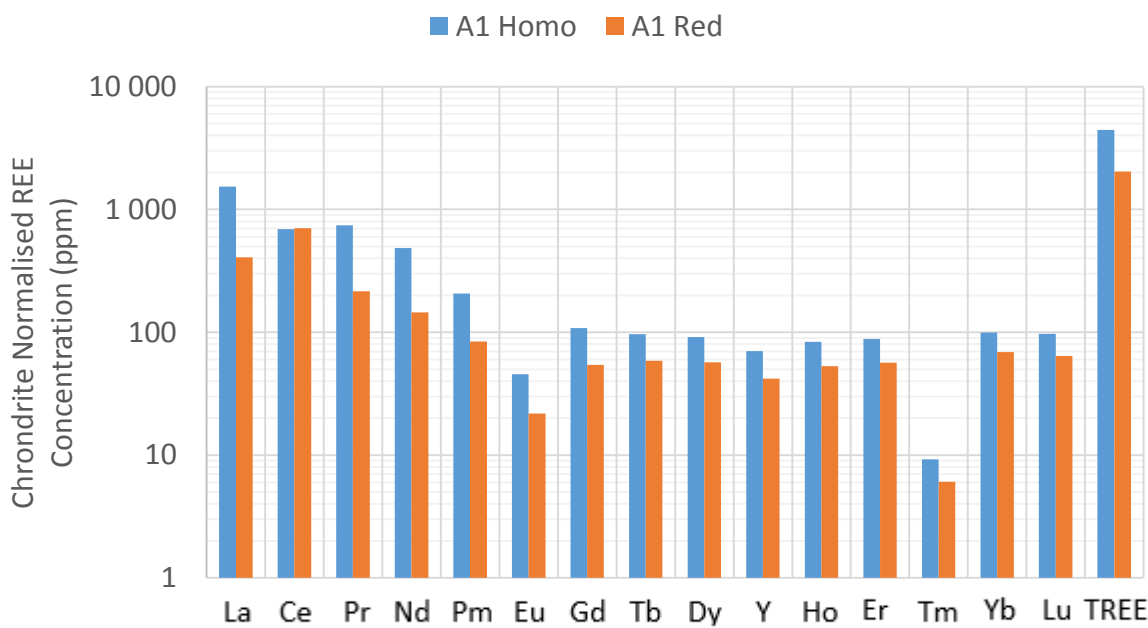
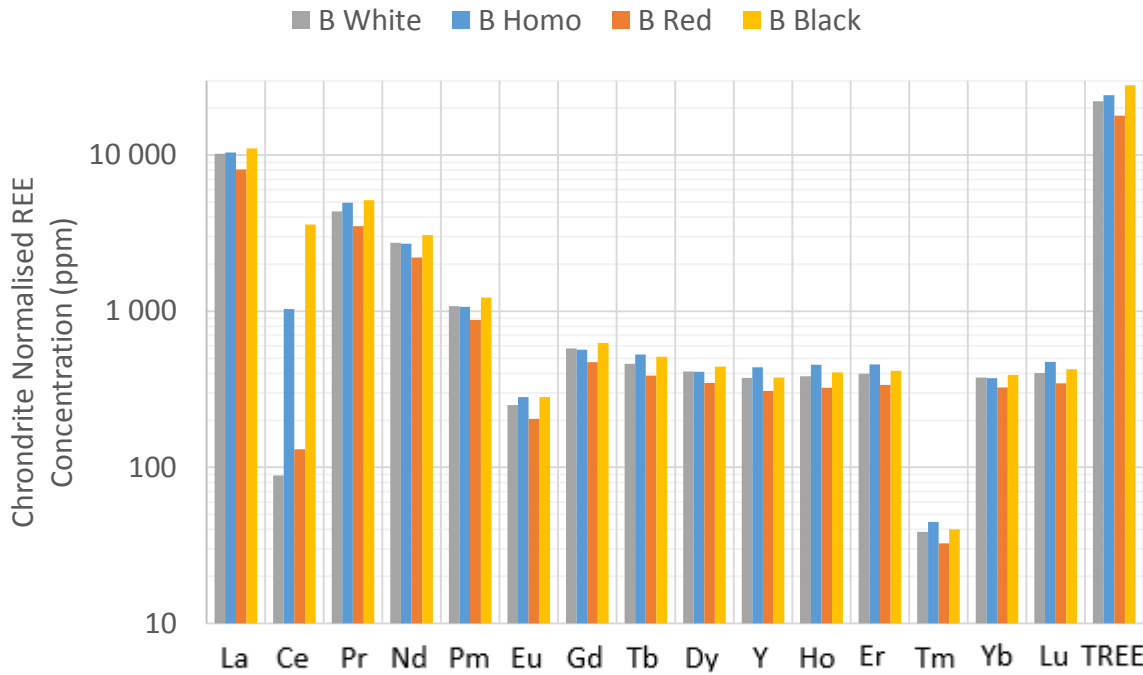
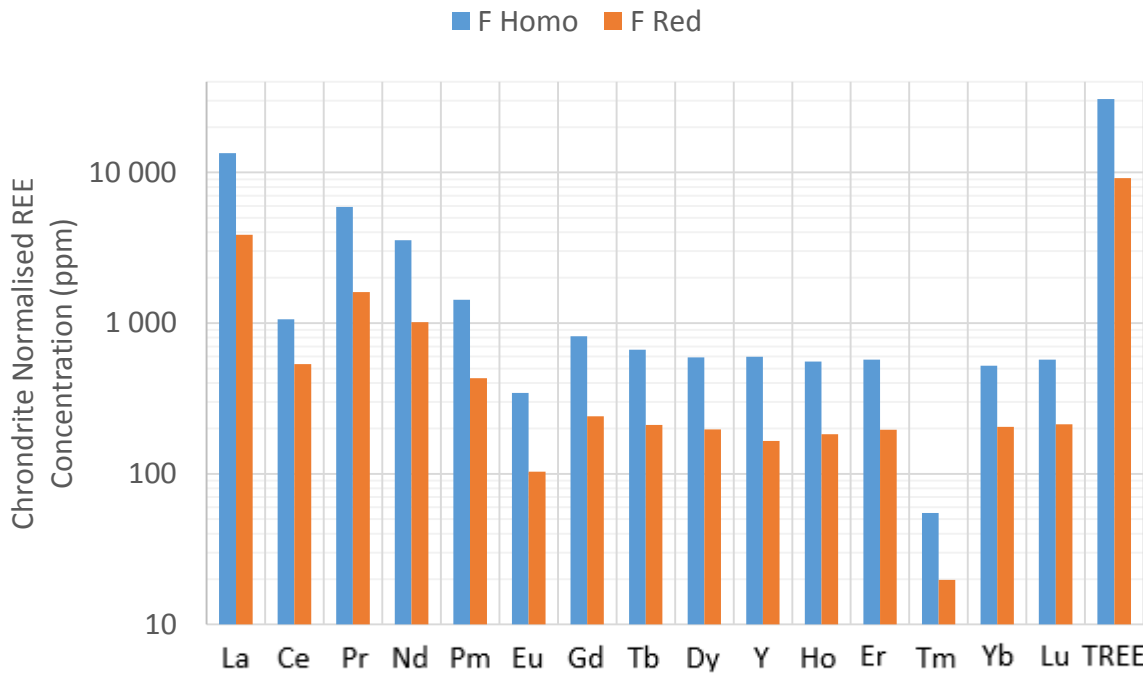


Figure 6.25 Sample A1 red phase REE concentration compared to homogenised concentration



**Figure 6.26 Sample B REE concentration distribution among the white, red and black phase compared to homogenised concentration**



**Figure 6.27 Sample F red phase REE concentration compared to homogenised concentration**

## 6.4.Ethics Clearance

### EBE Faculty: Assessment of Ethics in Research Projects

Any person planning to undertake research in the Faculty of Engineering and the Built Environment at the University of Cape Town is required to complete this form before collecting or analysing data. When completed it should be submitted to the supervisor (where applicable) and from there to the Head of Department. If any of the questions below have been answered YES, and the applicant is NOT a fourth year student, the Head should forward this form for approval by the Faculty EIR committee: submit to Ms Zulpha Geyer ([Zulpha.Geyer@uct.ac.za](mailto:Zulpha.Geyer@uct.ac.za); Chem Eng Building, Ph 021 650 4791). **NB: A copy of this signed form must be included with the thesis/dissertation/report when it is submitted for examination**

*This form must only be completed once the most recent revision EBE EIR Handbook has been read.*

Name of Principal Researcher/Student: Cody Burcher-Jones      Department: Chemical Engineering

Preferred email address of the applicant: BRCCOD001@myuct.ac.za

If a Student:                      Degree: MSc in Chem Eng                      Supervisor: Jochen Petersen

If a Research Contract indicate source of funding/sponsorship: NRF

Research Project Title: Mineralogical and ion-exchange leaching study of a Rare Earth Element (REE) bearing ion-adsorption clay deposit

#### Overview of ethics issues in your research project:


<b>Question 1: Is there a possibility that your research could cause harm to a third party (i.e. a person not involved in your project)?</b>	YES	NO ✓
<b>Question 2: Is your research making use of human subjects as sources of data?</b> If your answer is YES, please complete Addendum 2.	YES	NO ✓
<b>Question 3: Does your research involve the participation of or provision of services to communities?</b> If your answer is YES, please complete Addendum 3.	YES	NO ✓
<b>Question 4: If your research is sponsored, is there any potential for conflicts of interest?</b> If your answer is YES, please complete Addendum 4.	YES	NO ✓

If you have answered YES to any of the above questions, please append a copy of your research proposal, as well as any interview schedules or questionnaires (Addendum 1) and please complete further addenda as appropriate. Ensure that you refer to the EIR Handbook to assist you in completing the documentation requirements for this form.

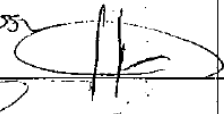

#### I hereby undertake to carry out my research in such a way that

- there is no apparent legal objection to the nature or the method of research; and
- the research will not compromise staff or students or the other responsibilities of the University;
- the stated objective will be achieved, and the findings will have a high degree of validity;
- limitations and alternative interpretations will be considered;
- the findings could be subject to peer review and publicly available; and
- I will comply with the conventions of copyright and avoid any practice that would constitute plagiarism.

Signed by:

	Full name and signature	Date
Principal Researcher/Student:	CODY BURCHER-JONES 	12/02/2016

This application is approved by:

Supervisor (if applicable):	J. Petersen 	12/02/2016
HOD (or delegated nominee): Final authority for all assessments with NO to all questions and for all undergraduate research.		12/02/2016
Chair : Faculty EIR Committee For applicants other than undergraduate students who have answered YES to any of the above questions.		